ABSTRACT

Title of Document: DEVELOPMENT AND VALIDATION OF A
                                BIDIRECTIONALLY COUPLED
                                MAGNETOELASTIC FEM MODEL FOR
                                CURRENT DRIVEN MAGNETOSTRICTIVE
                                DEVICES

                                Frank Graham, M.S., 2009

Directed By: Professor, Alison Flatau, Aerospace Engineering

A bidirectionally coupled magnetoelastic model (BCMEM) has been extended to include electric currents in its magnetic finite element formulation. This enables the model to capture the magnetoelastic behavior of magnetostrictive materials subjected to elastic stresses and magnetic fields applied not only by permanent magnets but also by current carrying coils used often in transducer applications. This model was implemented by combining finite element solutions of mechanical and magnetic boundary value problems using COMSOL Multiphysics 3.4 (Finite Element Modeling software) with an energy-based non-linear magnetomechanical constitutive model. The BCMEM was used to simulate actuator load lines and four point bending results for Galfenol, which were then compared to experimental data. The model also captured the ΔE effect in Galfenol. The BCMEM can be used to study and optimize the design of future current driven magnetostrictive devices.

DEVELOPMENT AND VALIDATION OF A BIDIRECTIONALLY COUPLED
MAGNETOELASTIC FEM MODEL FOR CURRENT DRIVEN
MAGNETOSTRICTIVE DEVICES

By

Frank Graham

Thesis submitted to the Faculty of the Graduate School of the
University of Maryland, College Park, in partial fulfillment
of the requirements for the degree of
Master of Science,
Aerospace Engineering
2009

Advisory Committee:
Professor Alison Flatau, Chair
Professor Norman Wereley
Professor Sung Lee

Acknowledgements

Table of Contents

List of Tables

List of Figures

Chapter 1: Introduction

Iron-Gallium alloys (Fe$_{1-x}$Ga$_x$ with $0.13 \leq x \leq 0.35$), more formally known as Galfenol, are a member of the magnetostrictive class of smart materials. These materials have an inherent coupling between their mechanical and magnetic properties. Application of magnetic field causes magnetostrictive materials to change in length, and stresses cause a change in the material magnetic induction. This unique transduction capability has led Galfenol to be an emerging choice for the potential use in many applications such as SONAR, tunable resonators, vibration suppressors, and acoustic wave propagation control. For a more general overview of magnetostrictive applications see Calkins et al. [1].

1.1 - Motivation for more accurate transducer modeling techniques

This thesis describes the development and validation of a Bidirectionally Coupled Magneto-Elastic Model (BCMEM). The model is created to model the behavior of transducers where the magnetic field is applied via a current carrying conductor. Previous work has been conducted to model the bidirectional behavior for permanent magnet cases and will be discussed later [2].

The ability to accurately depict the key characteristics of Galfenol transducers using a modeling technique will assist the design of magnetostrictive transducers. The key characteristics investigated in this research include the ability to analyze the behavior of different geometric transducer setups, and to model the nonlinear material behavior and magnetoelastic coupling present in Galfenol.

A model, which utilizes the finite element method, allows for the analysis of any type of transducer design. The ability to easily analyze complex geometries will prove to be an advantage for the BCMEM over previous models, which assume constant field and stress conditions. Stress and field distributions will allow one to more thoroughly understand the performance characteristics of every aspect of a particular design. This will aid in the design of magnetostrictive applications.

Galfenol exhibits nonlinear material characteristics which will be discussed in more detail in Section 1.4. These nonlinear material characteristics can be accurately depicted using energy-based models and incorporated into the mechanical and magnetic finite element models (FEM) that are used in the BCMEM via interpolation files. This will allow for the model to accurately predict the magnetostriction and magnetic field as a function of both the stress and magnetic induction.

The use of a command-based language in conjunction with a finite element model will allow for the ability to couple the mechanical and magnetic models. COMSOL Script allows for the user to import, alter, and analyze different models developed in the COMSOL Multiphysics graphical user interface. Solutions to the mechanical and magnetic models are imported to COMSOL Script and coupled together to accurately predict magnetostriction and magnetic field based off the solutions to the mechanical model (σ) and the magnetic model (B) (i.e., $\lambda(\sigma,B)$ and $H(\sigma,B)$).

The following sections serve as a background on magnetostrictive material characteristics, origin, behavior, and modeling techniques.

1.2 - Smart materials background

Smart materials are a unique class of materials that have the ability to transduce between different forms of energy. This ability has led to the use of smart materials in sensing and actuating applications. These materials are classified according to their energy transduction mode, with the most common class of materials being piezo-electrics, shape memory alloys, and magnetostrictives.

Piezo-electric materials exhibit a change in the electric state of the material when subject to a stress and are useful in low stroke high bandwidth applications [3], leading them to being used as acoustic drivers, vibration suppressors, and force/acceleration sensors.

Shape memory alloys have the ability to transduce thermal energy to mechanical energy and are useful in high stroke, low bandwidth applications, and thus justifies their use for tracking helicopter blades [3], and seismic vibration isolation systems [4].

Magnetostrictives transduce between magnetic and mechanical energy. The motivation for the development of transducer materials heightened in the World War II era, where SONAR applications became important. As previously discussed, several other applications include tunable resonators, vibration suppressors, and acoustic wave propagation control. Magnetostrictive materials will be discussed in more detail in the following section.

1.2.1 – Magnetostrictive materials

Magnetic materials exhibit dimensional change (magnetostriction, λ) and magnetization (M) change when subjected to applied magnetic fields and/or elastic stresses. The phenomenon of dimensional change due to applied magnetic field is known as the Joule effect [5], and magnetization change due to the applied stress is known as the Villari effect [6]. The Joule and Villari effects are caused by re-orientation of magnetic moments in the material and are relevant in actuating and sensing applications, respectively.

Magnetostriction is quantified as a strain with non-dimensional units of parts-per-million (ppm), which defines the change in length of the material with respect to its original length upon application of a magnetic field. This phenomenon was first discovered by Joule in ~1860 when it was found that Iron (Fe) changes dimension when its magnetization was changed [7].

Recognition of Nickel (Ni) and Cobalt (Co) as materials possessing low magnetostriction followed with maximum or saturation magnetostriction values of ~40 and 60 ppm observed respectively [8].

It was later found in the 1960's that rare earth metals such as Dysprosium (Dy) and Terbium (Tb) can yield magnetostrictions of greater than 1500 ppm. Proper alloying of Dy and Tb with Fe led to the discovery of a material known as Terfenol-D ($Tb_xDy_{1-x}Fe_y$), with x~0.3 and y~2, which yielded magnetostrictions of greater than 2000 ppm [9]. Although this material has high magnetostrictive capabilities, it is brittle with a tensile strength of 28 MPa, and is therefore limited to cases involving uniaxial compressive loading [10].

More recently, Iron-Gallium alloys ($Fe_{100-x}Ga_x$ with ~$13 \leq x \leq 32$), known as Galfenol, have been shown to be capable of handling a wider array of applications, with a tensile strength of ~515 MPa [11], making it useful for applications involving bending [12] and torsion [13]. The high tensile strength of Galfenol motivates its use in underwater environments involving underwater shocks and blasts. The magnetostriction in Galfenol (~350 ppm) is only moderate as compared to Terfenol-D (~1600 ppm), but its ability to handle applications involving bending and torsion motivate further research of Galfenol. Some additional advantages of Galfenol include its ability to achieve saturation magnetostriction at a much lower applied magnetic field (~100 Oe) than that required by Terfenol-D (~1000 Oe), as well the fact that Galfenol exhibits less hysteresis and is also more easily machined than Terfenol-D and other smart materials [14]. Galfenol is also very easy to weld to existing structures making it an easy component to incorporate into a system. Further, Galfenol has a high Curie temperature of 675 °C (compared to ~350 °C in Terfenol-D), allowing it to be used over a wider range of temperatures [15]. All of the previous information provided is relevant for single crystal Galfenol behavior. Polycrystals exhibit saturation magnetostriction of ~200 ppm, but may vary significantly with sample due to large differences in texture [14]. However, polycrystal Galfenol can be produced at 350 mm/hr as opposed to 2-4 mm/hr for single crystal Galfenol [16]. This will allow polycrystal Galfenol to be more easily made commercially available than single crystal Galfenol. Table 1.1 outlines performance characteristics of the previously described smart materials. It is evident that Galfenol's free strain capabilities are not as large as piezoelectrics, SMAs, or the

magnetostrictive material, Terfenol-D. However, as discussed, the key advantages of

Galfenol (both single and polycrystal) are that it is ductile, has a high tensile strength,

and possesses lower hysteresis SMAs and Terfenol-D.

Table 1.1 – Properties of several smart materials [3, 14, 16]

Material Type	Free Strain (ppm)	Modulus (GPa)	Tensile Strength (MPa)	Actuation requirement	Bandwidth	Linearity
Piezoelectric - PZT-5H	1000	~68	27.6 (Brittle)	5 kV/cm (Electric Field)	0.1 Hz – ~1 MHz	First-order linear (small hysteresis)
SMA - Nitinol	60,000	~20 (martinsite) ~50 (austenite)	High (Ductile)	Heating through ~60° C	0-1 Hz	Highly non-linear (large hysteresis)
Magnetostrictive - Terfenol-D	1600-2400	25-35	28 (Brittle)	~1000 Oe (Magnetic Field)	0 Hz – ~1 MHz	Non-linear (moderate hysteresis)
Magnetostrictive - Single Crystal Galfenol	300-400	~60	500 (Ductile)	~100 Oe (Magnetic Field)	0 Hz – ~1 MHz	Non-linear (low hysteresis)
Magnetostrictive - Polycrystal Galfenol	170-220	~72-86	~440 (Ductile)	~200 Oe (Magnetic Field)	0 Hz – ~1 MHz	Non-linear (low hysteresis)

1.3 – Origin of Magnetostriction

Magnetic materials possess a strong coupling between their electron spin and

the crystal lattice spacing of the material. Thus, the lattice spacing of rare earth

metals is strongly influenced by a magnetization change [17].

This research will study the behavior of magnetostrictives below their Curie

temperature so that the material is in a ferromagnetic state. In this state, the exchange

energy causes the magnetic moments of the material to form randomly oriented

magnetic domains. A magnetic domain is a region of magnetic moments with the

same magnetization. The rotation of the magnetic domains is strongly coupled to the

material lattice spacing, and leads to a dimensional change in length. Alignment of

all of the magnetic moments in one direction will cause the formation of a single

domain. At this point, there is no further strain obtainable from the material since all

of the magnetic moments are aligned in the direction of applied field, and thus the

material is said to be in the saturated state. The strain corresponding to this condition

is known as the saturation magnetostriction.

When operating above the Curie temperature, the thermal energy substantially

outweighs the exchange energy of the material and this prevents the magnetic

moments of the material from forming magnetic domains. The material is said to be

in paramagnetic state. When a magnetic material is cooled through the Curie

temperature from a paramagnetic state into a ferromagnetic state, a spontaneous

magnetostriction occurs due to magnetic domain formation. Spontaneous

magnetostriction is approximately half of the saturation magnetostriction of the

material [15].

1.4 – Actuating and Sensing of Magnetostrictives

Magnetic materials exhibit dimensional change (magnetostriction, λ) and

magnetization (M) change when subjected to applied magnetic fields and/or elastic

stresses. Figure 1.1 shows an example of how a magnetostrictive material can be

used as an actuator. Initially, the magnetic moments of the material are aligned in

random nature. However, when the material is subject to a magnetic field (H), these

moments begin to orient themselves in the direction of the applied field. Once a high

enough field is applied, all of the moments will be aligned parallel to the applied

field. The elongation of the sample is quantified with a variable known as

magnetostriction (λ), and is the change in length of the material divided by its original

length ($\Delta l/l$). It is clear that once all domains are aligned along the length of the rod,

the maximum value of magnetostriction that is possible will be achieved, thus leading

to a nonlinear relationship between λ and H.
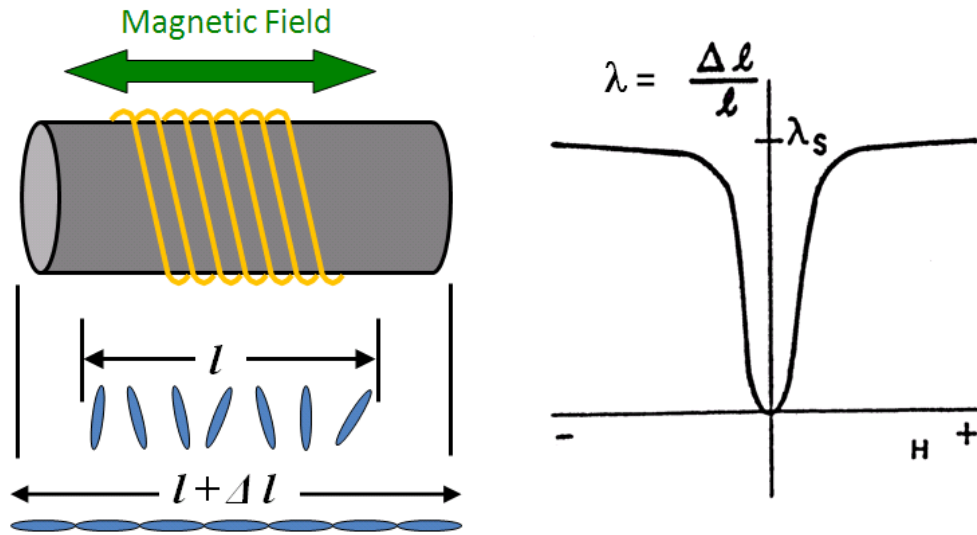
Figure 1.1. Schematic of actuation of magnetostrictive rod and corresponding λ-H behavior.

The Villari Effect also occurs in magnetostrictives and can be used to describe

the sensing behavior of such materials. Consider the case where the saturation

magnetic field is applied to the sample. If one begins to apply compressive stresses to

a magnetostrictive, one will see a drop in the magnetic induction. This change in

magnetic induction due to applied stress warrants its use in sensor applications.
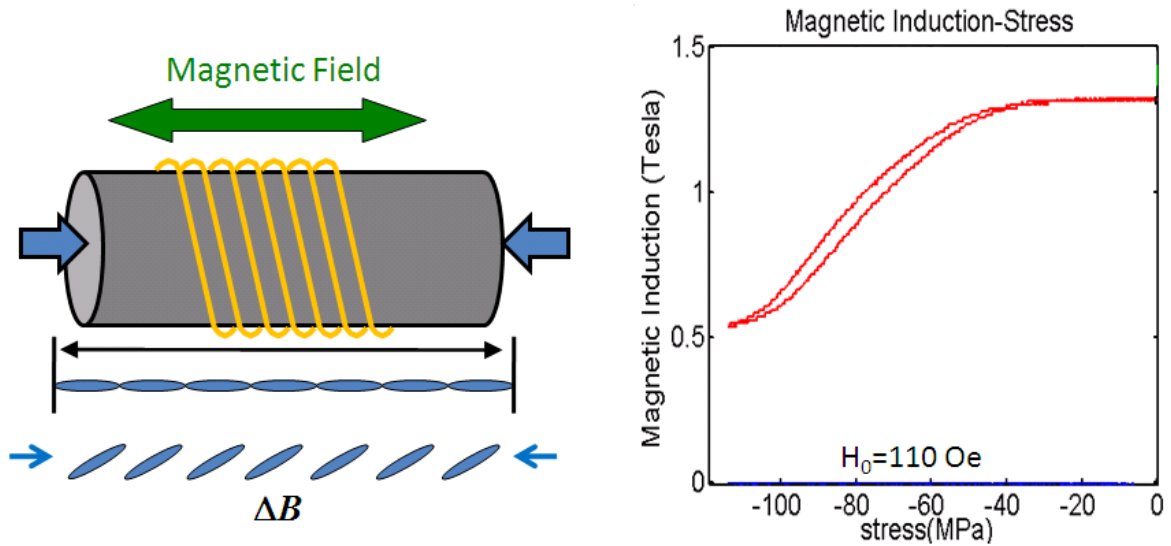
Figure 1.2. Schematic of sensing of magnetostrictive rod and corresponding B-H behavior.

As shown previously, there are two commonly used plots that describe the performance of magnetostrictive materials. One plot describes the relationship between magnetostriction and applied magnetic field (λ-H), and the other plot shows the relationship between magnetic induction and magnetic field (B-H). Figures 1.3 and 1.4 show typical λ-H and B-H plots, respectively, for an 18.4% polycrystalline Galfenol sample. The experimental characterization is discussed in detail in Appendix A. Both figures exhibit low hysteresis which is characteristic in Galfenol. One additional characteristic to note is that both of these characteristic material plots show a stress dependency. In particular, compressive stress increases the saturation magnetostriction. However, there is an optimal compressive stress that should be used for maximizing magnetostriction. This stress causes the magnetic moments to be completely aligned perpendicular to the applied stress. In this case, the maximum magnetostriction can be achieved upon application of field. The application of

further compressive stress beyond the optimal value will not cause any further increase in the magnetostriction. Instead, this higher compressive stresses will require the need for more magnetic field to create the same magnetostriction (i.e., saturation magnetostriction will occur at a higher field). The B-H plot (Figure 1.4) also shows a stress dependency as a drop in relative permeability (dB/dH) is observed upon application of a compressive stress. It will be important to have the ability to capture this stress dependency when developing a model for transducer design work.
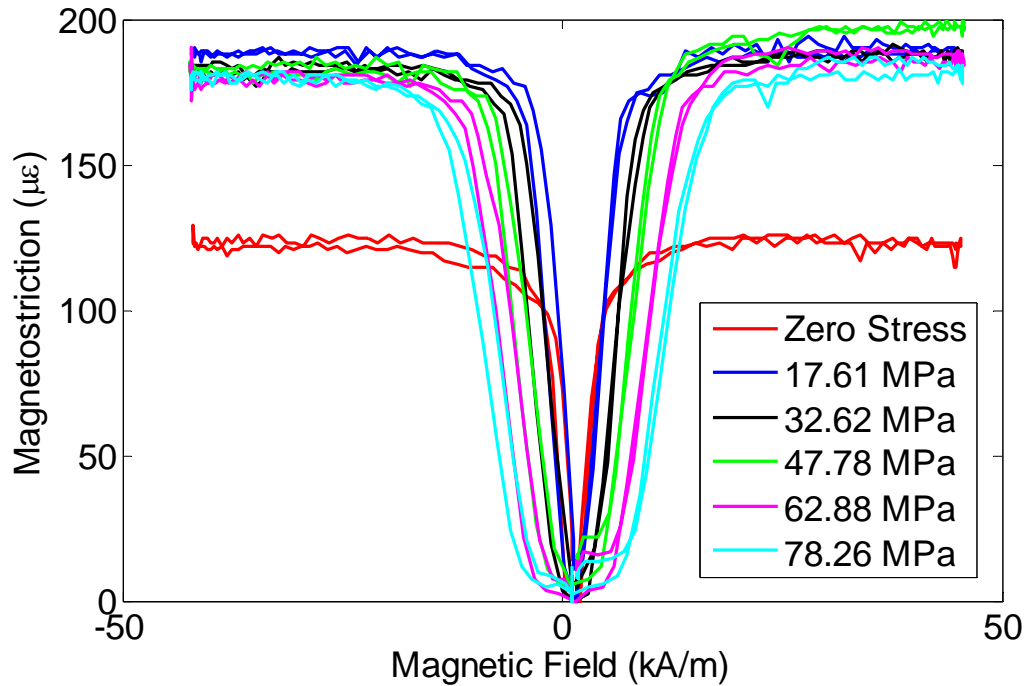
Figure 1.3. λ-H plot for 18.4% at. Ga, polycrystal, production grade (Etrema Products, Inc.)
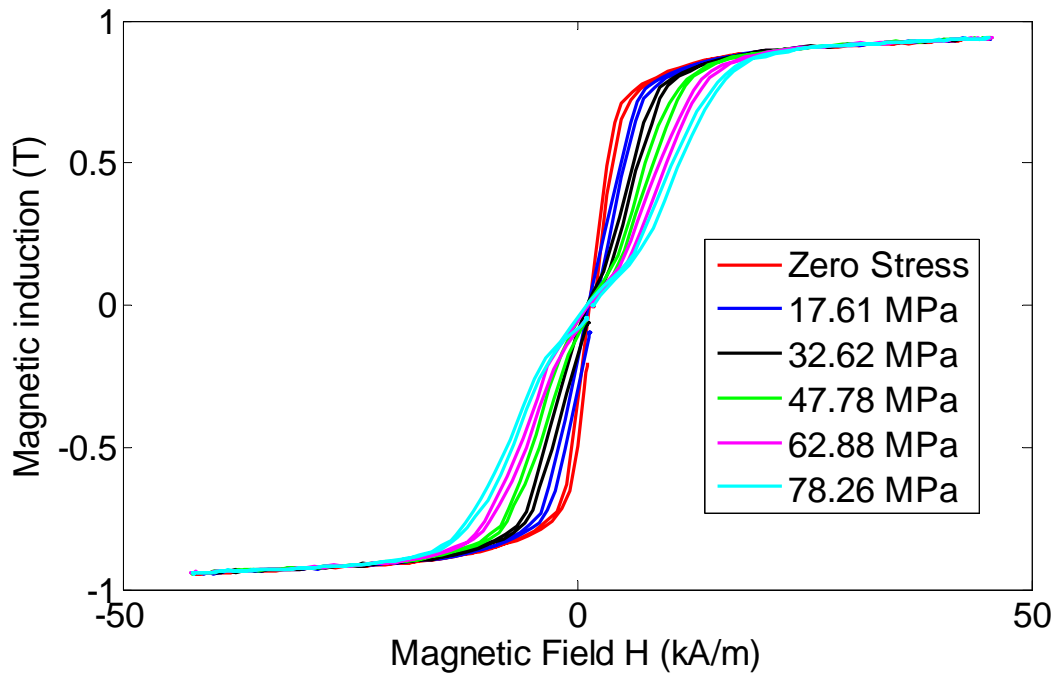
Figure 1.4. B-H plot for 18.4% at. Ga polycrystal, production grade (Etrema Products Inc.)

Another key characteristic of Galfenol behavior is its dependency on Gallium concentration. Figure 1.5 shows the relationship between magnetostriction and percentage Gallium. The relationship is highly nonlinear with a double-peaked characteristic. The figure also shows a dependency on whether the particular sample was quenched or furnace cooled, especially for Gallium contents surrounding the first peak (i.e., ~400 ppm at 19% Ga for quenched and ~320 ppm at 17% Ga for furnace cooled samples). It has been claimed that the short range ordering of Ga atoms in the A2 phase of Fe lead to an increase in magnetostriction up to ~17% (furnace cooled) and ~19% (quenched) at. Ga [18]. It has been claimed that the formation of $D0_3$ leads to the decrease in magnetostriction after the first peak (~17% and ~19% at. Ga for furnace cooled and quenched samples respectively). Further, it has been claimed that

the magnetostriction begins to rise again at ~24% at. Ga due to a drop in the elastic

shear modulus [14]. The maximum magnetostriction at ~27% at. Ga has been

claimed to occur as a result of lattice softening [19].
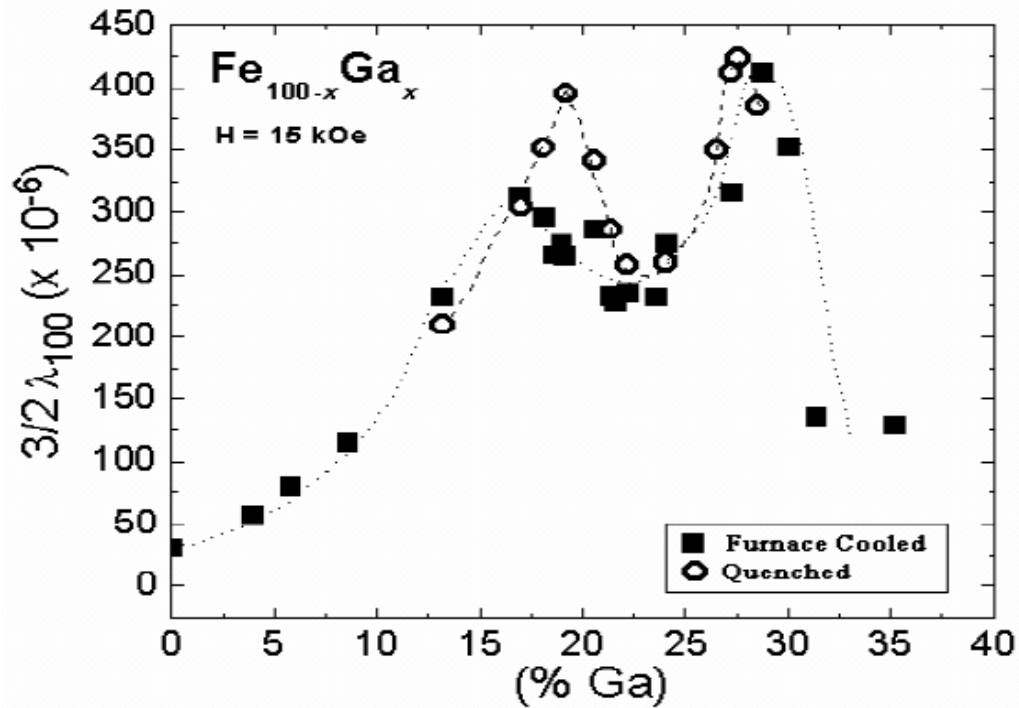
Figure 1.5. Magnetostriction ($3/2\lambda_{100}$) of single crystal FeGa vs. Ga content [20, 21]

1.5 – Modeling magnetostriction

An understanding of the mechanical and magnetic characteristics of

magnetostrictive materials is necessary to fully understand their capabilities in

transducers. Several models will be discussed in this chapter ranging from basic

models such as the linear constitutive equations to a more complicated finite element

method approach which couples an energy-based model to FEM solutions of the

mechanical and magnetic BVPs (BCMEM).

1.5.1 – Linear constitutive equations

The coupled 1-D linear constitutive relations based model [22], [23] is one of the most widely used methods to predict magnetostrictive behavior (Equations 1.1 and 1.2). These equations relate changes in stress and magnetic field to changes in strain and magnetic induction. This is done through coupling coefficients, d_{33} and $d_{33}*$. The coefficient d_{33} represents the change in strain due to a change in magnetic field and the coefficient d_{33}^* represents the change in magnetic induction due to a change in stress. The compliance, S^H, defines the stiffness of the material at a constant magnetic field, and the permeability, μ^σ, defines the magnetic properties of the system describing the B-H relations at constant stress. However, these equations are valid only for small perturbations of applied field and stress about an operating point within the linear region of magnetostrictive response, and they fail to properly predict the nonlinear magnetoelastic behavior over the entire operating range [2], or to address hysteretic behavior.

$$\varepsilon = S^H \sigma + d_{33} H \qquad (1.1)$$

$$B = d_{33}^* \sigma + \mu^\sigma H \qquad (1.2)$$

A common method of determining the transduction capability of magnetostriction materials is to use the magnetomechanical coupling factor. The magnetomechanical coupling factor is a way to quantify the efficiency of transduction between magnetic and mechanical energy. It can determined with a knowledge of the

piezo-magnetic coefficients d_{33} and d_{33}*, as well as the Young's Modulus at a

constant field condition and relative permeability at a constant stress condition

(Equation 1.3) [24].

$$k = \sqrt{\frac{d_{33}d_{33}^{*}E^{H}}{\mu^{\sigma}}} \qquad (1.3)$$

1.5.2 – Preisach model

The Preisach model was developed to predict hysteresis in ferromagnetic

materials. It employs an on-off operator which is dependent on the current and

previous states of the material. Suzuki and Matsumoto [25] has extended this model

to account for stress effects on the hysteretic loop. Due to the negligible hysteretic

effects on Galfenol, this research will not explore the effect of accounting for the

effects of hysteresis.

1.5.3 - Non-linear energy-based models

Several magnetomechanical energy-based models have been created in an

attempt to capture the non-linear behavior present in Galfenol.

Modeling techniques by Dapino et al. [26], include a thermodynamic

approach for estimating magnetostriction and magnetization to stress, field, and stress

annealing.

Additional modeling techniques have been reported by Sablik and Jiles [27],

where internal energy minimization is used to ensure mechanical equilibrium. This

model is capable of capturing the hysteretic effect, although for Galfenol, this effect is rather small as compared to other magnetostrictives.

Yet another energy based model has been reported by Armstrong [28]. It determines the total energy as the sum of the Zeeman, stress-induced anisotropy, and magnetocrystalline anisotropy energies along different orientations of magnetization given an applied stress and magnetic field. This is a probabilistic model where magnetic domains are most likely to orient along directions that correspond to energy minima. The net magnetization and magnetostriction of the sample along a particular direction are calculated as an ensemble average of the magnetization or magnetostriction along the different orientations. The Armstrong model [28] will be the model used in this research, and will be discussed in more detail later.

1.5.4 – Analytical magnetoelastic coupled modeling

Analytical methods have also been developed for predicting magnetostrictive performance. Datta et al. [29] developed magnetoelastic coupled models suitable for actuator and sensor analysis. This was done by coupling Classical Laminated Plate Theory (CLPT) to the nonlinear energy based Armstrong model described in Section 1.5.3. Datta et al. [29] uses CLPT to solve for the stress state of the material. The Galfenol samples studied are assumed to have a uniform magnetic field. The nonlinear energy based model is used to calculate $\lambda(H,\sigma)$. The resulting magnetostriction is reinserted into CLPT to solve for a new stress condition. This process is repeated until a convergence on the stress state is reached.

This modeling approach is suitable for geometries that satisfy the thin plate assumptions of CLPT. When analyzing complex geometries, the finite element

method will generally give a more accurate result. However, the approach taken by Datta et al. [29] will provide a faster solution than by using the finite element approach.

1.5.5 – Unidirectional modeling

A unidirectional sensor model that includes effects of stress on magnetic induction has been implemented [14]. Magnetomechanical coupling was employed by coupling solutions to the Armstrong model and a lumped parameter magnetic model. Since the modeling is unidirectional in nature, only the effect of stress on magnetic field is considered, and the reciprocal (effect of magnetic field on stress) is not considered. For the application boundary conditions considered in the research conducted by [14], unidirectional modeling gives the exact solution to the problem. Scenarios when unidirectional modeling is a valid modeling technique will be discussed in more detail later.

Atulasimha [14] also used his unidirectional modeling techniques to show the optimal placement of a Hall sensor and sensing coil for determining magnetic field and induction respectively. Radial and longitudinal variations of magnetic field were plotted to determine the optimal locations of these measuring devices. Several improvements to a transducer design [30] were proposed based off of the model predictions.

1.5.6 – Bidirectional modeling for permanent magnet cases

Bidirectional modeling that couples the magnetic and elastic BVPs using an energy based magnetomechanical model has been research by Mudivarthi et al. [2].

The Armstrong Model was used to create λ-H and B-H material data for the model. Bidirectional modeling captures both the effect of the stress on magnetic field, as well as the effect of magnetic field on stress.

However this work only considers permanent magnet cases, and is not applicable to current carrying applications, and thus the set of Maxwell Equations reduce to equations 1.4-1.6 below. An iterative approach was used to solve the mechanical and magnetic BVPs. A 0.2% difference between stress and field between iterations was used as the convergence criteria. A Galfenol unimorph structure was modeled using this bidirectional model. Model results for ε_z and B_z versus bending moment showed good correlation with experimental results, with the model only requiring about 5 iterations.

$$\nabla \cdot B = 0 \qquad (1.4)$$
$$\nabla \times H = 0 \qquad (1.5)$$
$$H = -\nabla V_m \qquad (1.6)$$

1.5.7 – Bidirectional modeling for current carrying cases

Most actuators develop a magnetic field using a current-carrying coil. The ability to model such applications using the techniques described in Mudivathi et al. [2] has not been implemented. Therefore, this research investigates the extension of the model described in section 1.5.6 to current-carrying applications. Development and implementation of a current-carrying BCMEM will be discussed in the next chapters.

Chapter 2: Modeling Magnetostriction

This chapter more thoroughly analyzes the key characteristics that should be incorporated into a magnetostriction model. First, the probabilistic energy-based model used to simulate experimental data is explained. Energy model simulations of nonlinear λ-H and B-H data are shown and the role of this model in the BCMEM is discussed. The advantages of using the finite element method are outlined, and several transducer setups are investigated to examine the differences in their magnetostatic performance. Next, a magnetic circuit analysis is conducted to further emphasize the need for a coupling mechanism in the model. Also, experimental H-σ results are presented to show a coupling between the mechanical and magnetic properties of Galfenol. The ability to couple the mechanical and magnetic FEM using a script-based language is also introduced. This chapter sets the stage for the BCMEM development which is discussed in Chapter 3.

2.1 – The Armstrong Model

The development of a model for predicting the performance of magnetostrictive materials should include the capability to predict the nonlinear λ-H and B-H characteristics of the material. The Armstrong model is one form of the energy based magnetomechanical models (briefly discussed in section 1.5.3) [28], which has been shown to give accurate predictions of magnetostrictive nonlinear material behavior [31].

This model determines the total energy as the sum of the magnetic, stress-induced, and magnetocrystalline anisotropy energies along different orientations of magnetization given an applied stress and magnetic field. This is a probabilistic

model where magnetic domains are most likely to orient along directions that correspond to energy minima according to a Boltzman distribution. The net magnetization of the sample along a particular direction is calculated as an ensemble average of the magnetization or magnetostriction along the different orientations. This model requires the input of five material constants: cubic crystalline anisotropy constants K_1 and K_2, magnetostrictive constants λ_{100} and λ_{111}, and the saturation magnetization M_s, along with an empirical Armstrong smoothing factor Ω. The constants M_s, λ_{100} and λ_{111}, K_1, and K_2 are determined experimentally, and Ω optimized such that the data simulated by the model closely matches that gathered experimentally. It is important to note that Ω was not optimized as a function of stress in this research.

Figures 2.1 and 2.2 show the effects of stress and magnetic field, on magnetostriction and magnetic flux density respectively. These figures were developed experimentally using a water cooled transducer for gathering data at a constant temperature of $21 \pm 1°$ C [30]. During the tests, λ-H and B-H data were gathered with the sample subject to several compressive loads ranging between 0 and 66 MPa. A constant magnetic field was applied to the sample with use of a feedback controller. The experimental setup and testing procedure is discussed in greater detail in Appendix A. For an even more detailed description of the water cooled transducer refer to [30].

It can be seen from Figure 2.1 that the application of compressive stress enhances the material's saturation magnetostriction. However, it also shows that the required magnetic field to saturate the material increases as the applied compressive

stress increases. Similarly, from Figure 2.2 it can be seen that the application of

compressive stress reduces the permeability of the sample. This behavior is well

captured by the Armstrong model.
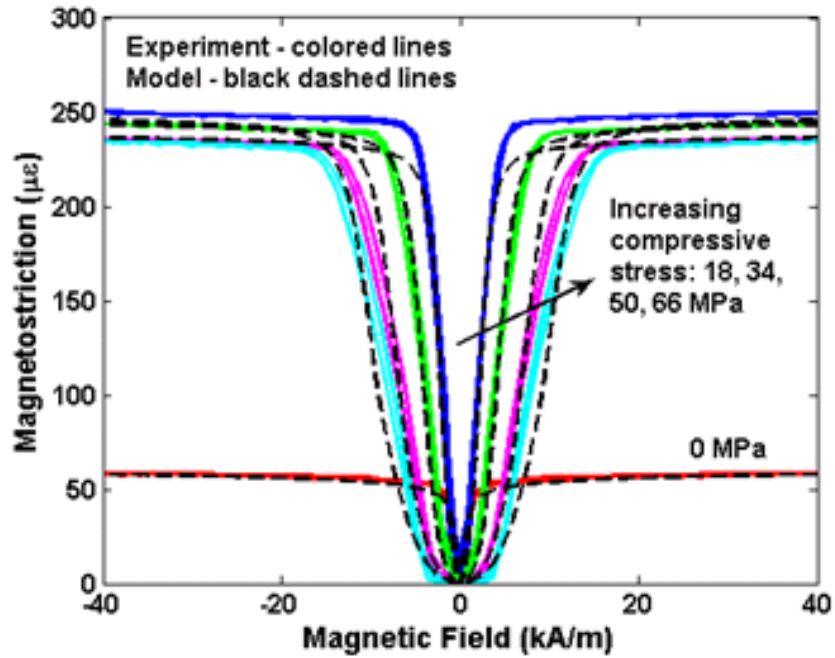
Figure 2.1. λ-H curve for 16% Ga. Sample, 100 oriented single crystal subjected to compressive loads of 0-66 MPa [32]. The Armstrong model parameters: M_S = 1456 kA/m, λ_{100}=165 ppm, λ_{111} = (2/3)*20 ppm, K_1 = 13 kJ/m^3, K_2 = -90 kJ/m^3, Ω = 600.

Figure 2.2. B-H curve for 16% Ga. Sample, 100 oriented single crystal subjected to compressive loads of 0-66 MPa [32]. The Armstrong model parameters: $M_S = 1456$ kA/m, $\lambda_{100} = 165$ ppm, $\lambda_{111} = (2/3)*20$ ppm, $K_1 = 13$ kJ/m^3, $K_2 = -90$ kJ/m^3, $\Omega = 600$.

Knowing that the Armstrong model agrees with the experimental data, linear interpolation and extrapolation using the model could be done to simulate behavior under other stress and field conditions. Although the experimental data shown in Figures 2.1 and 2.2 is only data for compressive prestresses, Atulasimha [14], has shown the use of the Armstrong model for extrapolation to the tensile condition. The ability to use the Armstrong model to determine λ-H and B-H data for many stress conditions will enhance the accuracy of the BCMEM.

The remainder of this section discusses the analytical formulation behind the Armstrong model.

Expressions for the different energy terms are shown below: magnetic (Equation 2.1), stress-induced (Equation 2.2), and magnetocrystalline (Equation 2.3)

energies along different orientations of magnetization given an applied stress and magnetic field [33]. In Equations 2.1-2.3 below, α_1, α_2, α_3 represent directional cosines of the magnetic moment, β_{1F}, β_{2F}, and β_{3F} correspond to directional cosines of the applied field, and β_{1s}, β_{2s}, and β_{3s} represent directional cosines of the applied stress.

The magnetic energy is the free energy of unit volume due to the applied magnetic field.

$$E_{magnetic} = -\mu_0 M_s H \left(\alpha_1 \beta_{1F} + \alpha_2 \beta_{2F} + \alpha_3 \beta_{3F} \right) \qquad (2.1)$$

The stress-induced energy is due to the energy extracted as the magnetic domains rotate upon application of stress.

$$\begin{aligned} E_{stress\_induced} = &-\frac{3}{2} \lambda_{100} \sigma \left(\alpha_1^2 \beta_{1s}^2 + \alpha_2^2 \beta_{2s}^2 + \alpha_3^2 \beta_{3s}^2 \right) \\ &- 3\lambda_{111} \sigma \left(\alpha_1 \alpha_2 \beta_{1s} \beta_{2s} + \alpha_2 \alpha_3 \beta_{2s} \beta_{3s} + \alpha_3 \alpha_1 \beta_{3s} \beta_{1s} \right) \qquad (2.2) \end{aligned}$$

The magetocrystalline energy is energy related to the difficulty of domain rotation.

$$E_{magnetocrystalline} = K_1 \left(\alpha_1^2 \alpha_2^2 + \alpha_1^2 \alpha_2^2 + \alpha_1^2 \alpha_2^2 \right) + K_2 \alpha_1^2 \alpha_2^2 \alpha_3^2 \qquad (2.3)$$

The total energy is found by summing together contributions due to magnetic, stress-induced, and magnetocrystalline energies (Equation 2.4).

$$
\begin{aligned}
E(\sigma,H) &= E_{magnetocrystalline} + \gamma_\sigma E_{magnetoelastic} + E_{magnetic} \\
&= K_1\left(\alpha_1^2\alpha_2^2 + \alpha_1^2\alpha_2^2 + \alpha_1^2\alpha_2^2\right) + K_2\alpha_1^2\alpha_2^2\alpha_3^2 + \\
&\quad \gamma_\sigma\left(\begin{array}{l} -\dfrac{3}{2}\lambda_{100}\sigma\left(\alpha_1^2\beta_{1s}^2 + \alpha_2^2\beta_{2s}^2 + \alpha_3^2\beta_{3s}^2\right) \\[2mm] -3\lambda_{111}\sigma\left(\alpha_1\alpha_2\beta_{1s}\beta_{2s} + \alpha_2\alpha_3\beta_{2s}\beta_{3s} + \alpha_3\alpha_1\beta_{3s}\beta_{1s}\right) \end{array}\right) \\
&\quad - \mu_0 M_s H\left(\alpha_1\beta_{1F} + \alpha_2\beta_{2F} + \alpha_3\beta_{3F}\right)
\end{aligned}
\tag{2.4}
$$

An energy weighted average is used calculate the magnetization in each direction, with orientation of magnetic domains in certain directions having higher probabilities than others (Equation 2.5). This is a probabilistic approach where magnetic domains are most likely to orient along directions that correspond to energy minima according to a Boltzmann's distribution. This concept is based on the fact that there are 6 energy minima (energy wells) present, and magnetic moments are more likely to orient themselves in these directions. Figure 2.3 shows the energy plotted for a zero stress condition and a compressive stress condition [14].

$$
M_x = \frac{\sum_{\sigma,\phi}\left(M_s\sin\theta\cos\phi\right)\left(d\theta d\phi\left|\sin\theta\right|\right)e^{\frac{-E(\theta,\phi)}{\Omega}}}{\sum_{\theta,\phi}\left(d\theta d\phi\left|\sin\theta\right|\right)e^{\frac{-E(\theta,\phi)}{\Omega}}}
\tag{2.5}
$$

The magnetization contributions corresponding to their respective orientations are then summed to obtain a total magnetization (Equation 2.6). This value of magnetization is used to determine the magnetic induction for a particular stress and field (Equation 2.7).

$$M(\sigma,H) = M_1\beta_i + M_2\beta_j + M_3\beta_k \qquad (2.6)$$

$$B(\sigma,H) = \mu_0\left(M(\sigma,H) + H\right) \qquad (2.7)$$
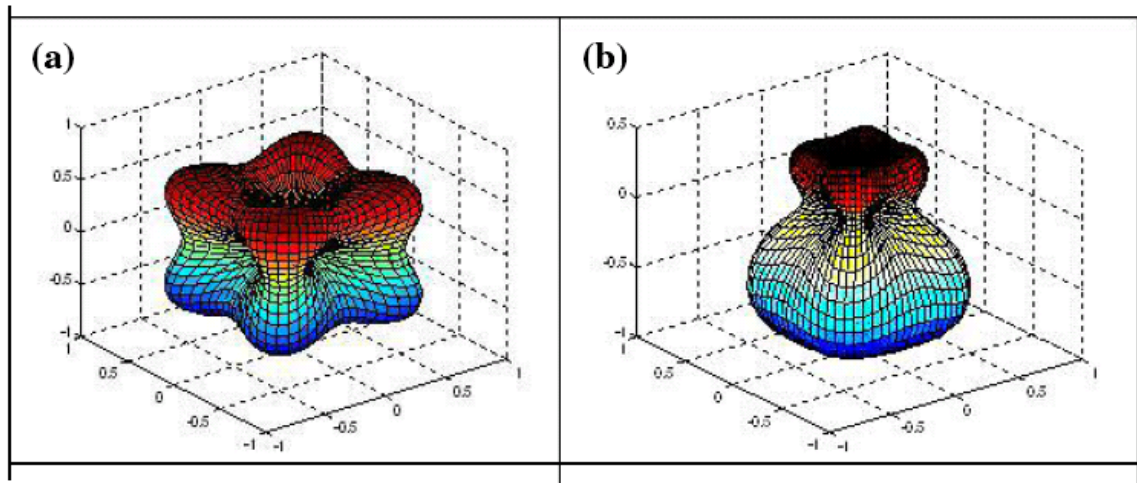
Figure 2.3. Energy plot for (a) zero stress, (b) compressive pre-stress [14]

2.2 - Demagnetization

When a magnetic field is applied to a magnetic material, the free magnetic poles towards the ends of the material will cause a demagnetization field in the direction opposite to the applied field. This demagnetization field depends on the geometry of the magnetostrictive material [33]. Figure 2.4 shows how demagnetization affects the effective magnetic field within an ellipsoid.
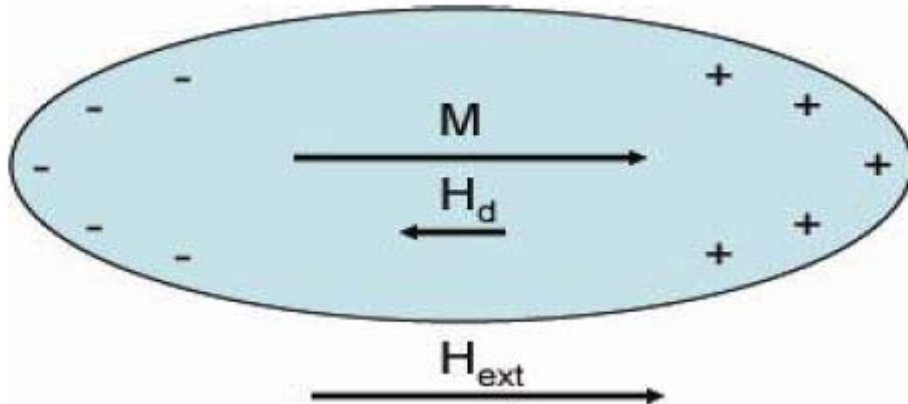
Figure 2.4. Demagnetization of an ellipsoid [14]

Analytical methods have been developed for determining the amount of
demagnetization field present in materials with simple geometric shapes. Equation
2.8 gives a general expression for determining the effective magnetic field within a
sample, with a known value of N_d (demagnetization factor) [14]. Since calculation of
the effective magnetic field (H_{eff}) requires a knowledge of N_d (geometry dependent),
the magnetic field within the sample is normally difficult to calculate (especially for
complicated geometries).

$$H_{eff} = H_{ext} - H_d = H_{ext} - N_d M \qquad (2.8)$$

Ellipsoidal geometries have been shown to have a relatively constant magnetic
field distribution, leading to one value of demagnetization factor for the entire
geometry. An analytical expression for calculating the demagnetization factor as a
function of a dimensional ratio (k) was developed by [33] (Equation 2.9). The

dimensional ratio, k, is determined by dividing the length of the semimajor axis by the semiminor axis.

$$N_d = \frac{1}{k^2-1}\left[\frac{k}{\sqrt{k^2-1}}\log_e\left(k+\sqrt{k^2-1}-1\right)\right] \qquad (2.9)$$

Other analytical methods have been developed by [34], where methods are given to calculate the demagnetization factor of rectangular prisms and cylinders. However, since the field varies greatly within these shapes, the demagnetization factor is solved for as a function of position. Calculating the demagnetization factor using a volumetric average approach is also investigated [34]. This approach gives one value of demagnetization factor for the shape.

The demagnetization factor has also been determined experimentally for simple geometries [33, 35]. However, these demagnetization factors are defined for positions relevant to the outer surface of the material. Again, the demagnetization factor is defined as a geometric property, as experimental demagnetization factors are listed as functions of dimension.

Many magnetostrictive applications will not consist of only a sample and a coil. Instead, there may be a surrounding transducer setup that was designed to increase the magnetic field within the sample. It is clear that a key disadvantage to using the available analytical approaches to determine the demagnetization factor is that they only consider cases of a sample in air that is surrounded only by a coil. Seeing this, it is not an accurate means of predicting the effective magnetic field

within a sample if immersed in a surrounding magnetic circuit. The following section

discusses how the finite element method is a more flexible approach than an

analytical approach.

2.2.1 – Analytical versus FEM demagnetization factor of a rectangular prism

As a basis for comparison, the analytical method for calculating the

demagnetization factor of a rectangular prism [34] is compared to FEM predictions,

where the effect of aspect ratio on demagnetization is investigated. A COMSOL

Multiphysics 3.4 magnetostatic (with currents) finite element model was created with

a geometry consisting of a rectangular prism immersed in a coil, surrounded by an air

domain with dimensions of three times the largest dimension of the rod and coil

(Figure 2.5). COMSOL Multiphysics 3.4 is the finite element software used

throughout this research. The logistics of the model creation will be discussed more

rigorously in Chapter 3.
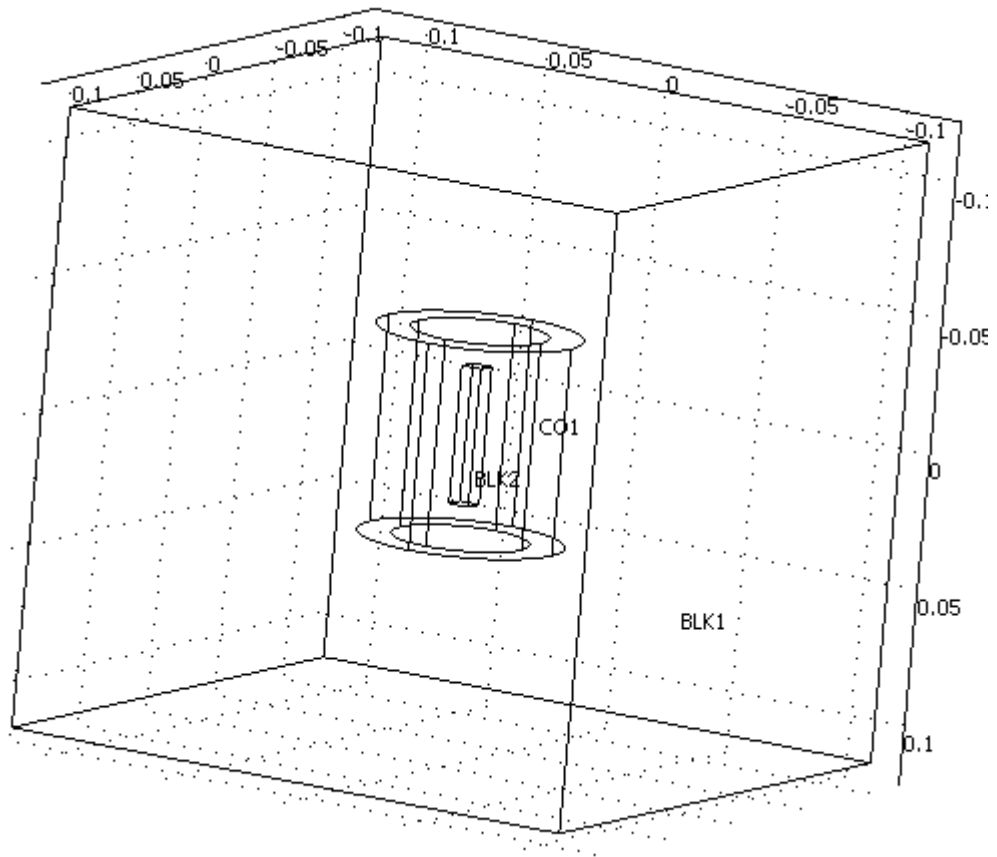
Figure 2.5. – COMSOL magnetostatics (with currents) geometric rod-coil setup.

To determine the demagnetization factor via a FEM approach, Equation 2.8 is rearranged and solved for the demagnetization factor (Equation 2.10). The external field is calculated by determining the magnetic field at a point of interest in space within the coil in the absence of the sample. The effective magnetic field and magnetization are determined at the same point, but with the sample in the model. The demagnetization factor was calculated for several aspect ratios, where the length of the sample always remained 2-inches. The square cross-section was varied to change the aspect ratio. It is clear that the FEM and analytical results show very good correlation over a large range of aspect ratios (Figure 2.6).

28

$$N_d = \frac{H_{ext} - H_{eff}}{M} \qquad (2.10)$$
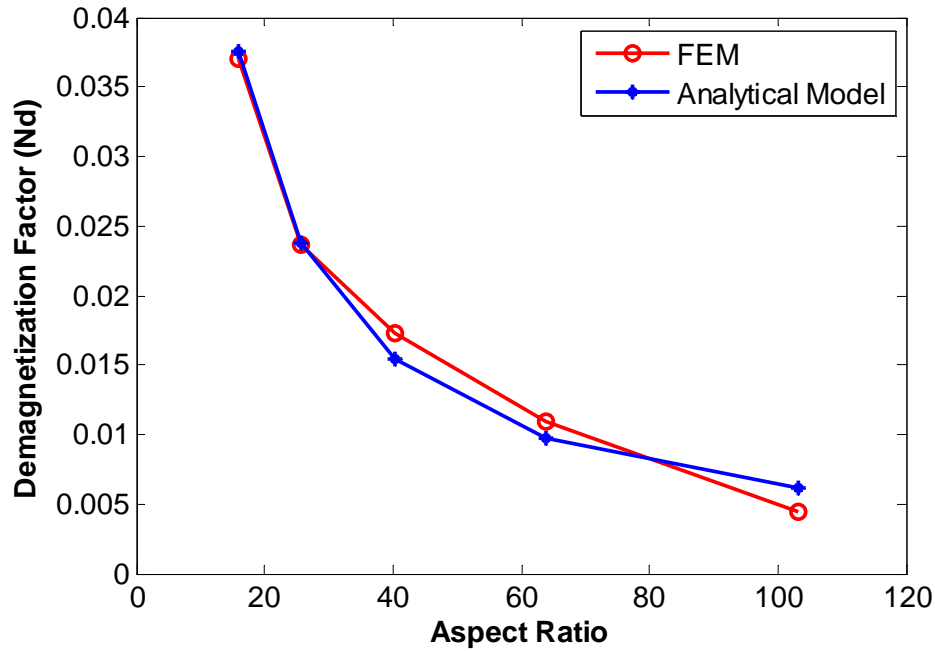
Figure 2.6. Demagnetization factor versus aspect ratio of a rectangular rod from FEM and an analytical approach [34].

In terms of modeling magnetic material performance, the finite element method allows one to quickly calculate the spatial variation of demagnetization. It also allows for the use of different geometric setups, which as will be discussed later, also plays a role on the magnetic field experienced within the sample. The following introduces how the finite element method provides valuable insight to magnetic field distribution behavior.

2.3 - Magnetic field distributions

This section concentrates on the finite element analysis of different basic transducer setups and their effects on the magnetic properties of a system. Magnetic field distributions will be used for each setup to emphasize key differences between different designs.

Consider the scenario of a cylindrical rod, made of a magnetic material such as Iron, surrounded by a coil. It was desired to simulate the magnetic field behavior along the radius and length of the rod. A 2D axisymmetric, magnetostatics (with currents) model was utilized. The rod was placed at the $r = 0$ location and was surrounded by a coil. The rod and coil setup is surrounded by an air domain ($\mu_R = 1$) with dimensions that are three times the length of the coil, which is the largest component of the circuit. A current density of 3e6 A/m^2 was assigned to the geometry corresponding to the coil. A relative permeability of 50 was assigned to the rod for this study.

Figure 2.7 shows a 2D axisymmetric streamline of the magnetic field when the magnetic sample ($\mu_R = 50$) is placed inside the coil. It is evident that due to the demagnetization effect, the magnetic field leaks throughout the length of the rod (i.e., some streamlines fail to travel the full distance of the sample). However, if a magnetic circuit is incorporated into the design of the transducer, then the flux leakage can be drastically reduced. In Figure 2.8, a steel flux return path is added to the same setup as in Figure 2.7, with $\mu_R = 2000$ for the steel. The use of a well-defined magnetic circuit will allow for the full use of the material capabilities, as there is negligible field lost due to flux leakage.
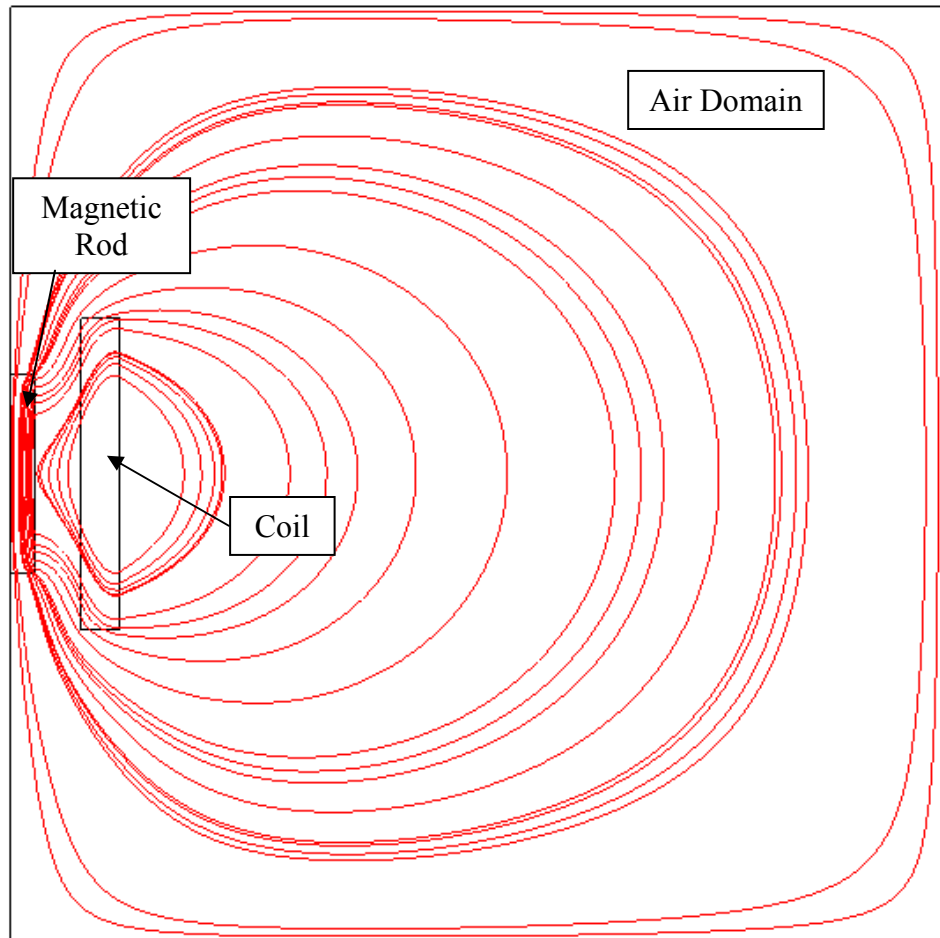
Figure 2.7. 2D axisymmetric view of magnetic field streamlines showing lines of flux leakage resulting from rod and coil setup
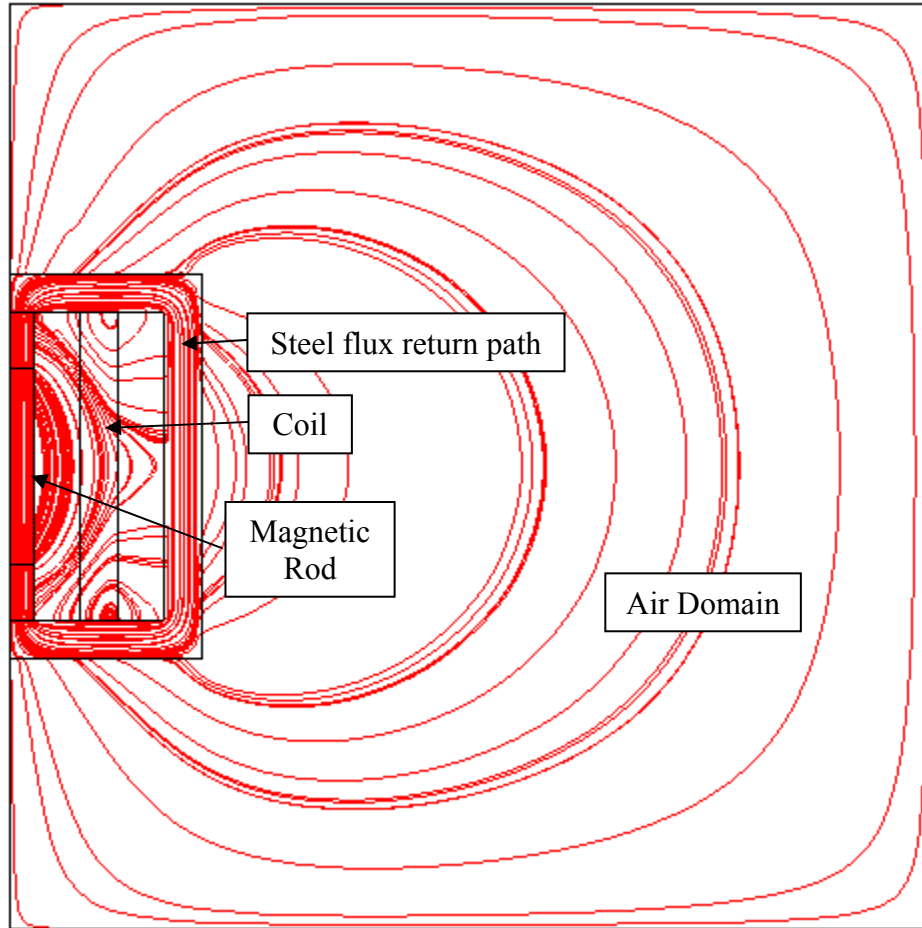
Figure 2.8. 2D axisymmetric view of magnetic field streamlines showing negligible flux leakage for rod and coil with steel flux return path

2.3.1 – Magnetic field studies of cylindrical sample

After analyzing Figures 2.7 and 2.8, it is clear that magnetic field distributions will provide valuable knowledge for optimization of transducer performance. Variation in the field along the length and radius of a cylindrical rod shaped sample will be studied in this section. Rods having a radius of 0.25-inches will be analyzed for aspect ratios of 1, 2, and 4 (0.5, 1, and 2-inch long rods respectively).

Consider the same two setups presented in Section 2.3, where different magnetic circuits were analyzed. As stated in the previous section, the magnetic rod

is assumed to have a constant permeability of 50. The steel flux return path discussed in the second case has a permeability of 2000. The current density used here is 3e6 A/m^2 for all cases.

First, the magnetic field distribution was studied for the no steel flux return case. Figure 2.9 shows a typical 2D axisymmetric contour plot of magnetic field in a rod (left) and the lines of constant field in a rod (right). The dashed lines in Figure 2.9 (left) show where the radial and lengthwise magnetic field distribution studies will be conducted for the remainder of this section.

Surface: Magnetic field, norm [A/m] Max: 3962.692

Radial distribution (r = 0 to outer radius, h = mid-height)

Length distribution (r = 0, h = 0 to length of rod)

Min: 879.656

Figure 2.9.   A 2D slice of a cylindrical sample from the centerline to the outer radius showing magnetic field contour (left) and streamlines (right) of the 0.5-inch long sample with no flux return path

The radial magnetic field distribution (at the mid-height of the rod) was studied for the no steel flux return case, for cylindrical rods with aspect ratios of 1, 2, and 4, and all with radii of 0.25-inches. The magnetic field data for each aspect ratio

33

was non-dimensionalized according to its maximum magnetic field value. The radial position was also non-dimensionalized (i.e., max field is one, and outer radius position is one). Figure 2.10 shows the non-dimensional results for the three different aspect ratios. It is important to note that because the magnetic fields are non-dimensional, the maximum magnetic field values for each aspect ratio are different. There are two sets of data shown for each aspect ratio. The dashed lines correspond to rods with length and width of half the sample shown by the red lines. Using these dimensions gives the same aspect ratio. It is evident that the non-dimensional magnetic field distribution does not vary for rods of the same aspect ratio. It is important to note that this is only true when comparing magnetic field distributions of the same shape. As determined in Section 2.2, the demagnetization effects vary between sample shapes. Also, these distributions are unique to the specific coil design and applied current density. Further, Figure 2.10 shows that lower aspect ratio samples experience a larger amount of non-dimensional magnetic field leakage from their centerline to the outer radius. Additionally, it is evident that the magnetic field increases from the center of the rod and reaches a maximum at the end of the rod for all aspect ratio cases. It should also be noted that the relationships shown in Figure 2.10 are parabolic. This parabolic magnetic field behavior plays a key role in the element type that is chosen for the mesh in the BCMEM. This will be discussed in more detail in Chapter 3.

Figure 2.10. Nondimensional radial magnetic field verses non-dimensional position for a rod and coil setup with varying aspect ratios. The dashed lines show rods with different dimensions that yield the same dimensions as the rods shown in the solid lines. All data is normalized to its respective maximum magnetic field

Next, the magnetic field distribution along the length of the rod was studied

for the no steel flux return case, for cylindrical rods with aspect ratios of 1, 2, and 4,

and all with radii of 0.25-inches. Again, the magnetic field data for each aspect ratio

was non-dimensionalized according to its maximum value. The position along the

length was also non-dimensionalized (i.e., maximum field is one, and top of rod

position is one). Figure 2.11 shows the non-dimensional results for the three different

aspect ratios. It is clear that higher aspect ratio samples experience a larger amount of

non-dimensional magnetic field leakage along the rods length. It is clear that the

maximum magnetic field can be expected to be seen in the mid height of the rod.

Also, the behavior of the top and bottom halves of the rods, act symmetrically.

Figure 2.11. Nondimensional longitudinal magnetic field verses non-dimensional position for a rod and coil setup with varying aspect ratios. All data is normalized to its respective maximum magnetic field (i.e., maximum magnetic fields for each sample length are: 7.16 kA/m (2-inch), 3.72 kA/m (1-inch), and 1.91 kA/m (0.5-inch)

Table 2.1 summarizes the magnetic field behavior shown in Figures 2.10 and

2.11. As the aspect ratio is increased, the percentage difference between the

maximum and minimum magnetic field through different locations along the radial

span decreases. On the contrary, the percentage difference between maximum and

minimum magnetic field along the length increases for samples with higher aspect

ratio ratios. Differences in magnetic field of 80.9% were seen along the length of a 2-

inch, 0.25-inch diameter sample. Appendix A will discuss the experimental

characterization of a Galfenol polycrystal with these same dimensions. This provides

valuable insight to experimental design, as it is not safe to assume a constant

magnetic field throughout the sample, especially along its length when using a

traditional rod and coil setup.

Table 2.1 – Percentage difference of magnetic field along radius and length of
cylindrical samples with radii of 0.25-inches and lengths of 0.5, 1, and 2-inches
(aspect ratio ratios of 1, 2, and 4) for rod and coil setup.

Aspect ratio aspect ratio	% difference in magnetic field along radius	% difference in magnetic field along length
1	17.4	54
2	5.2	70
4	1.6	80.9

The next set of model runs were implemented with a steel flux return path of

the same dimension as described in Section 2.2.1. Figure 2.12 shows a typical 2D

axisymmetric view of the magnetic field contour plot (left) and magnetic field

streamlines (right). It is clear that the presence of the steel flux return path increases

the magnetic field within the sample, as well as creates a more uniform distribution of
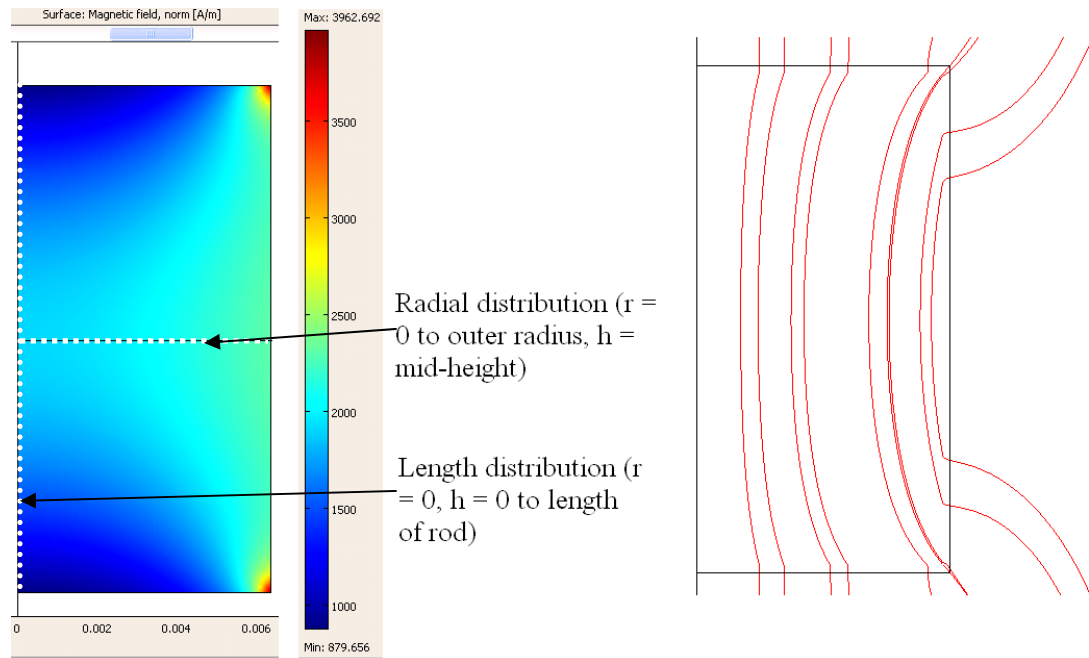
magnetic field.
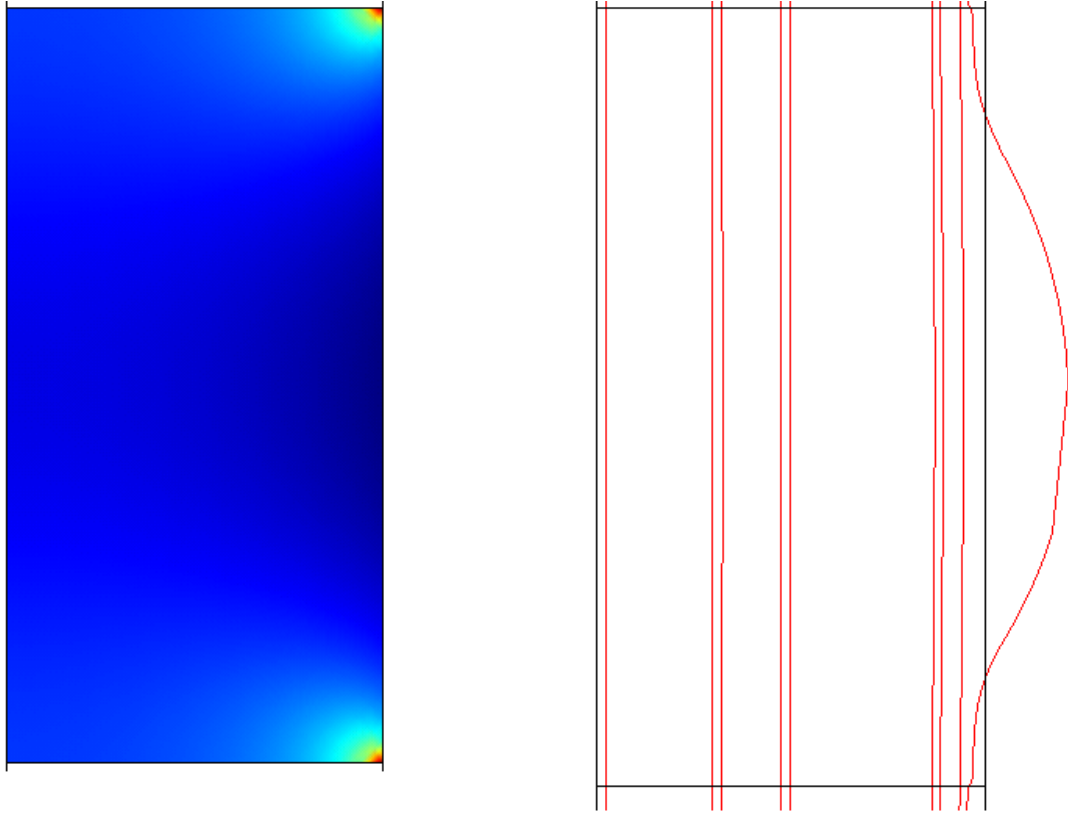
Figure 2.12. A 2D slice of a cylindrical sample from the centerline to the outer radius showing magnetic field contour (left) and streamlines (right) of the 0.5-inch long sample with no flux return path

The radial magnetic field distribution (at the mid-height of the rod) was studied for the steel flux return case, for the same cases as done for the no steel flux return path studies. The magnetic field distributions along the radius will again be shown in a non-dimensionalized form. Figure 2.13 shows the non-dimensional results for the three different aspect ratios. It is clear that lower aspect ratio samples experience a larger amount of non-dimensional magnetic field leakage from their centerline to outer radius. Additionally, it is evident that the magnetic field decreases from the center of the rod and reaches a minimum at the end of the rod for all aspect ratio cases. This is due to the fact that the outer radius of the rod is in contact with

air. The magnetic field will follow the steel flux return path due to its high permeability, and be most heavily concentrated in the center of the rod. However, note that the differences between the center and outer radius are much smaller when using a steel flux return path (Figure 2.13) than without using a steel flux return path (Figure 2.10).
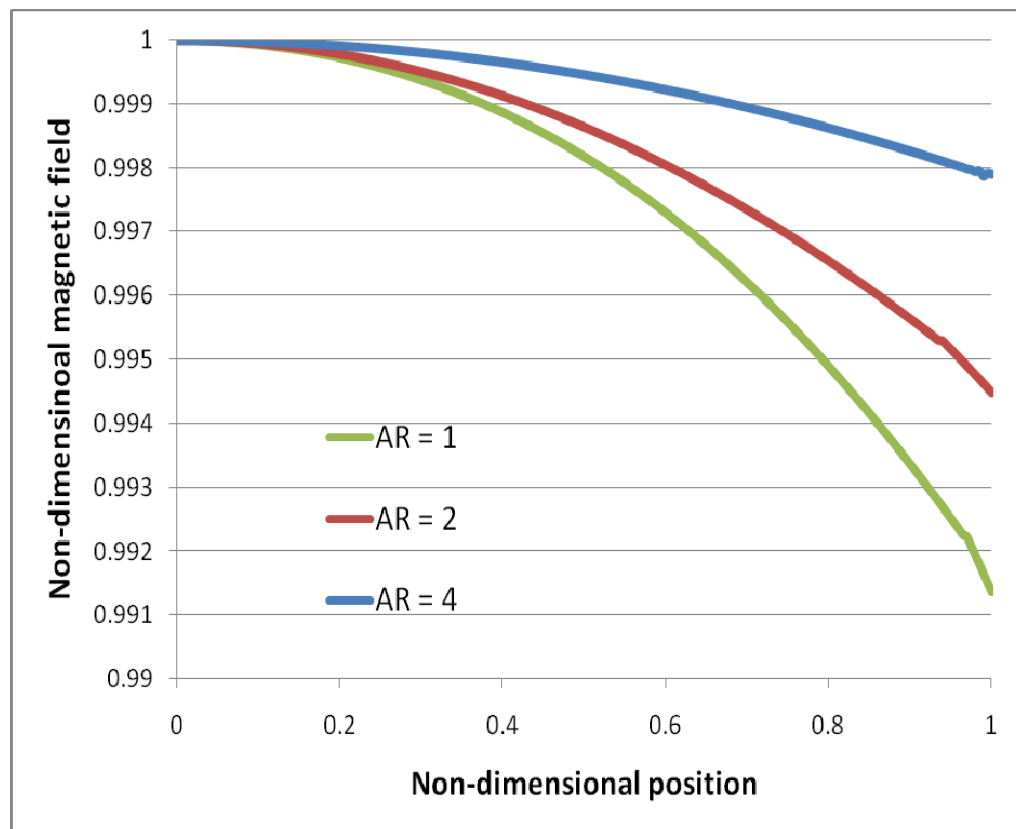
Figure 2.13. Nondimensional radial magnetic field verses non-dimensional position for a rod and coil setup with a flux return path, with varying aspect ratios. All data is normalized to its respective maximum magnetic field.

Next, the magnetic field distribution along the length of the rod was studied for the no steel flux return case, for cylindrical rods with aspect ratios of 1, 2, and 4. Again, the magnetic field data for each aspect ratio was non-dimensionalized according to its maximum value. The position along the length was also non-dimensionalized (i.e., maximum field is one, and top of rod position is one). Figure 2.14 shows the non-dimensional results for the three different aspect ratios. It is clear that higher aspect ratio samples experience a larger amount of non-dimensional magnetic field leakage along the rod length. However, in comparison to the no steel flux return case, the amount of magnetic field leakage along the length is reduced. It is clear that the minimum magnetic field can be expected to be seen in the middle height of the rod. Also, the behavior of the top and bottom halves of the rods, act symmetrically.
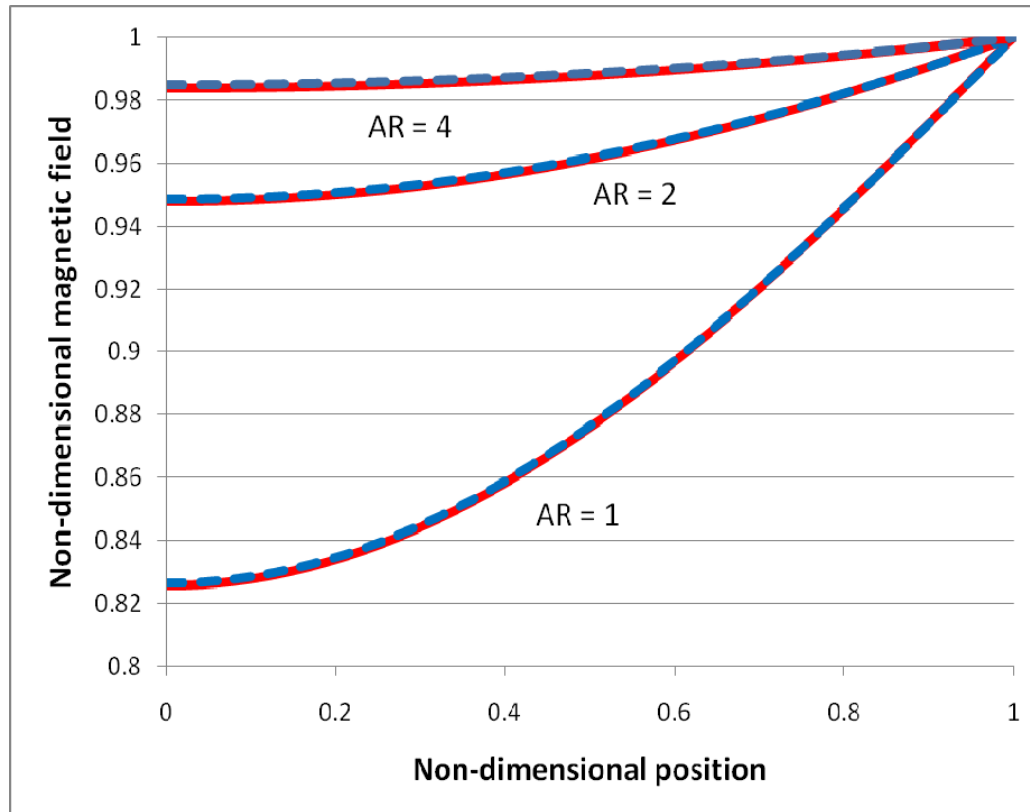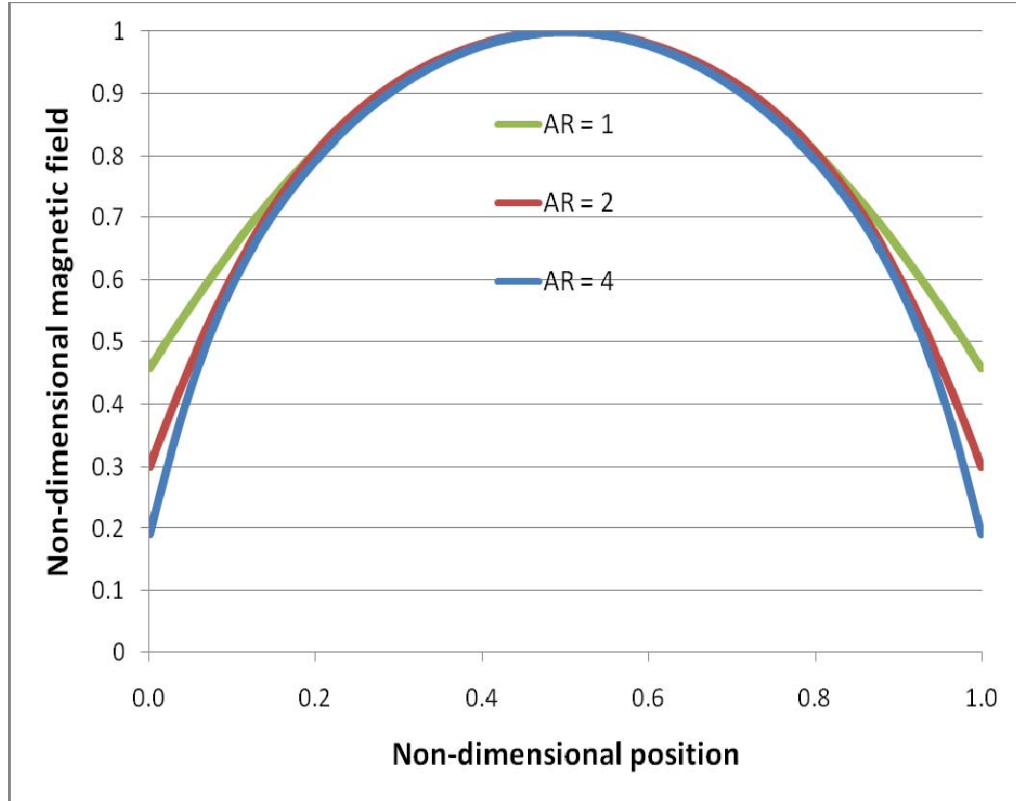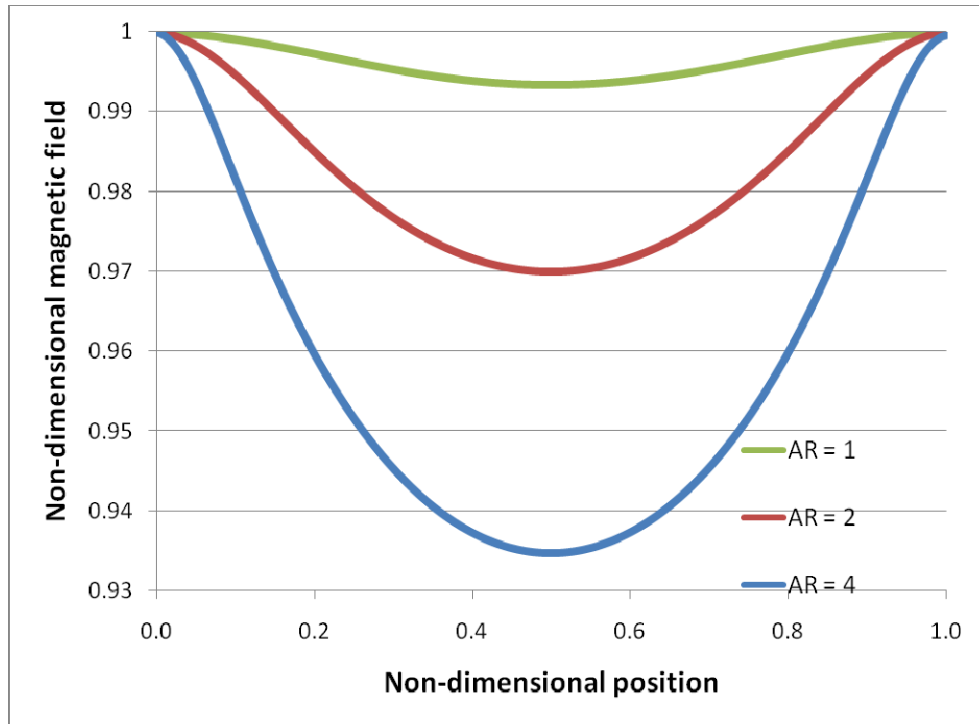
Figure 2.14. Nondimensional longitudinal magnetic field verses non-dimensional position for a rod and coil setup with varying aspect ratios. All data is normalized to its respective maximum magnetic field.

Table 2.2 summarizes the magnetic field behavior shown in Figures 2.13 and 2.14. As the aspect ratio increases, the percentage difference between the maximum and minimum magnetic field through the radial span decreases. In contrast, the percentage difference between maximum and minimum magnetic field along the length increases for samples with higher aspect ratios. Differences in magnetic field of 6.5% were seen along the length of a 2-inch, 0.25-inch diameter sample. However, in comparison to Table 2.1, the steel flux return path eliminates a large amount of the flux leakage leading to small percentage differences in magnetic field along the radius and length of the sample.

Table 2.2 – Percentage difference of magnetic field along radius and length of cylindrical samples with radii of 0.25-inches and lengths of 0.5, 1, and 2-inches (aspect ratios of 1, 2, and 4) for rod, coil, and steel flux return path.

aspect ratio	% difference in magnetic field along radius	% difference in magnetic field along length
1	0.9	0.7
2	0.6	3
4	0.2	6.5

It is clear that the spatial variation of magnetic field varies greatly with transducer setup. To obtain a more uniform field, this parametric study suggests it is important to include a flux return path. It was also found that it is desirable to use samples of lower aspect ratio, as the percentage change in magnetic field is much smaller for lower aspect ratio samples. Seeing this, the magnetic circuit should be modeled before experimentation. This will help with the decision of where to place the strain gage, Hall sensor, and pickup coil, as well as give one a first look at how the transducer will perform. It was shown that a steel flux return path greatly reduces the radial and longitudinal variations of field.

As a side note, it is important to realize that most Galfenol applications will involve Galfenol samples with changing permeability. This can greatly affect the magnetic circuit as will be discussed in Section 2.6. However, the use of FEM as shown in this section can provide valuable information on the performance of any type of geometry setup and magnetic circuitry.

2.4 – Stress Distributions

As discussed previously, the magnetostriction and magnetic field of a magnetostrictive material are strongly influenced by the stress state of the material. The linear constitutive equations and energy based models assume constant uniform stress conditions. For Galfenol, however, many practical applications will involve bending and/or torsion in the material.

Consider the case of a unimorph structure, where a magnetostrictive patch is mounted on a beam. When the magnetostrictive patch is actuated, the beam will bend, and thus cause non-uniform stresses through the thickness of the magnetostrictive material. Consider the case of nanowires used for acoustic sensing. The nanowires will vibrate when subject to acoustic waves, and thus bending stresses, with tension and compression on opposite sides of the neutral axis, will be induced in wires. Finally, consider the development of Galfenol as a torque sensor. The idea here is to conformally mount magnetostrictive patches around a curved portion of a shaft and to use the patches to sense the torsional loads applied to the shaft.

The stress distributions arising from these applications will be non-uniform. To account for this spatial stress variation, a mechanical finite element model of Galfenol under different mechanical loading conditions was implemented.

2.5 – Magnetoelastic coupling

As has been previously discussed, there is a strong coupling between the mechanical and magnetic properties of magnetostrictive materials. This is evident upon investigating the dependency of magnetostriction and magnetic induction on

stress and field when using either the linear constitutive equations or the Armstrong model. Section 1.5.5 discusses how such coupling can be achieved for unidirectional cases. However, magnetostrictives rarely behave in a unidirectional manner, but instead they behave bidirectionally.

To understand bidirectional behavior, consider a fixed-fixed rod subjected to a magnetic field. Mechanical constraints prevent magnetostriction from occurring, and as a result, the applied field induces a compressive stress in the material.

Consider the balance of magnetomotive force (MMF) in a magnetic circuit as stress and field vary. From the B-H curve previously presented (Figure 1.4), it is evident that μ_R (slope of the B-H curve) changes when the stress changes. A compressive stress will cause a drop in μ_R and a tensile stress will cause a rise in μ_R.

Consider the effect that a changing μ_R will have on the reluctance of a magnetostrictive material in a magnetic circuit. It is known that μ_R is related to the reluctance from Equation 2.11. An investigation of Equation 2.11 will show that a stress change (which changes μ_R) will lead to a reluctance change. A compressive stress (decrease in μ_R), will cause an increase in reluctance, and a tensile stress (increase in μ_R) will cause a decrease in reluctance.

Further, the reluctance is related to the MMF via Equation 2.12. A compressive stress (increase in reluctance), will cause an increase in MMF, and a tensile stress (decrease in reluctance), will cause a decrease in MMF.

Finally, reluctance can be related to magnetic field by using a combination of Equations 2.13 and 2.14 to for Equation 2.15. A compressive stress (increase in

44

MMF), will lead to an increase in magnetic field, and a tensile stress (decrease in MMF), will lead to a decrease in magnetic field.

This coupling behavior is shown in Figure 2.15. Modeling of this interaction becomes an iterative approach until a convergence criterion for change of stress and field is satisfied. It is clear that this process is not unidirectional in nature since the mechanical problem has an effect on the magnetic problem, and the magnetic problem has an effect on the mechanical problem. This motivates the need for a bidirectionally coupled model which can handle this phenomenon.

$$\Re(\sigma, H) = \frac{L}{\mu_0 \mu_r(\sigma, H) A} \tag{2.11}$$

$$MMF(\sigma, H) = \Re(\sigma, H) \phi(\sigma, H) \tag{2.12}$$

$$MMF(\sigma, H) = NI \tag{2.13}$$

$$H(\sigma, H) = \frac{NI}{L} \tag{2.14}$$

$$H(\sigma, H) = \frac{MMF(\sigma, H)}{L} \tag{2.15}$$

$\Re$ = reluctance

L = length

A = cross-sectional area

MMF = magnetomotive force

ϕ = magnetic flux

N = number of turns
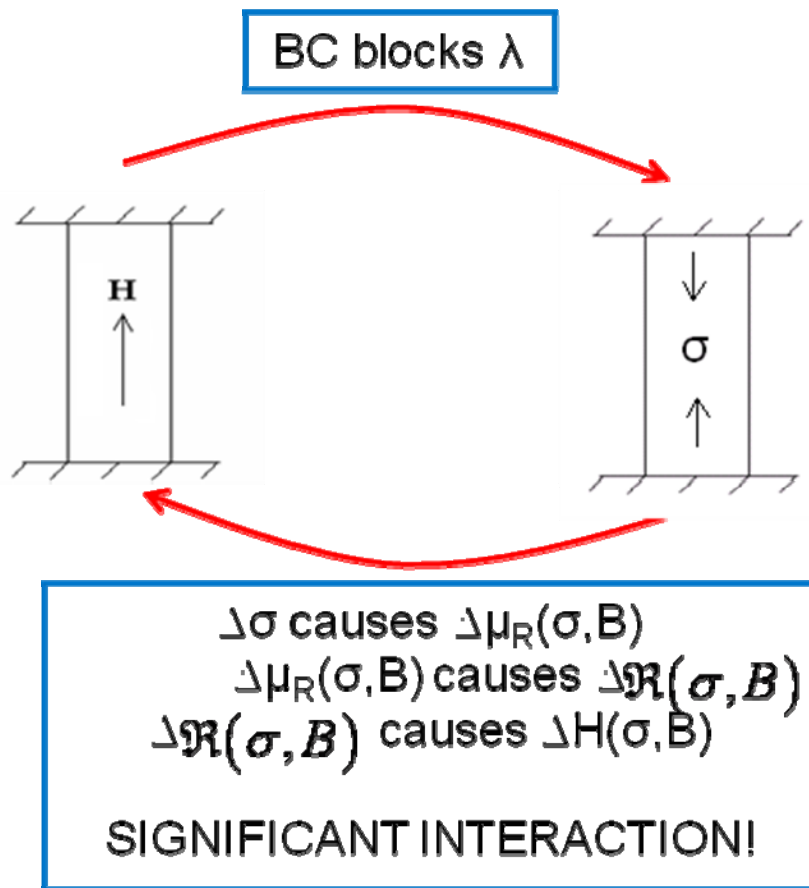
Figure 2.15 - Schematic showing bidirectional magnetoelastic coupling in a fixed-fixed rod.

A magnetic circuit depiction of a magnetostrictive transducer is shown in

Figure 2.16. The variable resistor represents the variable relative permeability and

thus reluctance of Galfenol. The other resistor represents the constant permeability and thus reluctance of the surrounding transducer. When there is a drop in relative permeability, the reluctance increases, causing an increase in MMF, which causes an increase in H.

Magnetoelastic coupling becomes an important modeling parameter for magnetostrictives that exhibit large changes in magnetic field under different stress conditions. This necessitates the need for proper modeling of this coupling phenomenon.
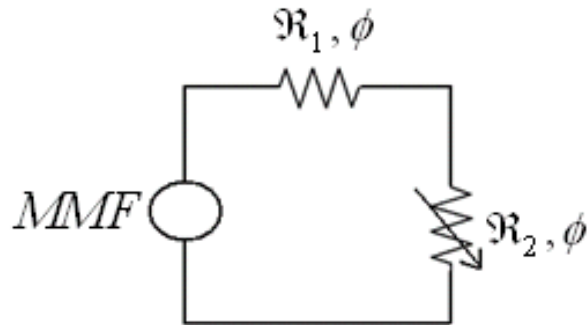
Figure 2.16. Magnetic circuit depiction of a magnetostrictive transducer

This strong coupling behavior has also been captured experimentally. Datta and Flatau [32] found a change in internal magnetic field when different stresses were applied to Galfenol. This experimental procedure will be discussed in more detail in Chapter 4. They observed that a constant current through the solenoid did not produce a constant magnetic field in the sample during the stress cycle as shown in Figure 2.17 [32]. A change in the sample reluctance occurs due to stress-induced

change in the permeability of the sample which in turn changes the internal magnetic field of the sample even for a constant applied field [36]. The proposed BCMEM needs to be able to accurately reproduce this type of experimental behavior.
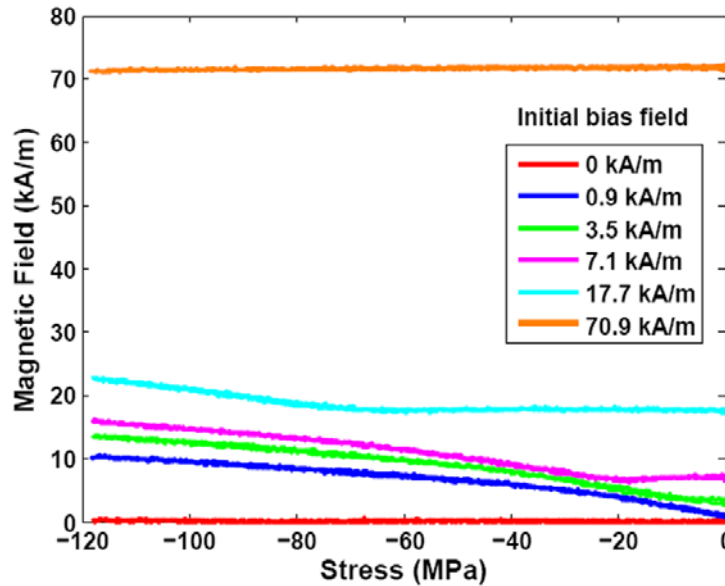
Figure 2.17. Variation in measured magnetic field in Galfenol as a function of compressive stress for different constant current in the transducer drive coil. The initial bias field measured after applying the current but in the absence of a stress are noted in the legend [32].

2.6 – Improved modeling strategies

Sections 2.1-2.5 outline several important and necessary techniques needed to properly model magnetostrictive materials. Galfenol behavior is strongly dependent on the Gallium concentration. Seeing this, experimental characterization is needed to properly understand the effect of varying Gallium content on λ-H and B-H performance. This behavior, as it is nonlinear in nature, needs to be captured accurately for use in a model. The Armstrong model has been shown to accurately depict experimental data. An advantage of the Armstrong model is its capability to

interpolate to generate λ-H and B-H data for many stresses that would not be feasible experimentally. Further, it was shown that there exists a spatial variation of the magnetic field distribution which is strongly dependent on the transducer setup used, as well as the stress state of the material. The capability to accurately model designs of vastly different magnetic circuits is crucial to advancing optimized use of magnetostrictive devices. Another key characteristic that is prevalent in magnetostrictive materials is magnetoelastic coupling. This is coupling between the magnetic and mechanical properties of the device, which led to continuous changes of the stress and relative permeability states of the material. This inherent coupling calls for solutions to both mechanical and magnetic BVPs in the model. Again, it was shown that the transducer used plays a role in the extent of magnetoelastic coupling present. These ideas are summarized in a flow chart below (Figure 2.18). The flow chart shows the use of FEM models with embedded characterized data simulated using the Armstrong model. The FEM allows for the use of force and current as inputs and magnetostriction and magnetic field as outputs. Finally, the magnetoelastic coupling is denoted by the arrows as the two models are coupled using COMSOL Script. The next chapter will discuss the model (BCMEM) in more detail.
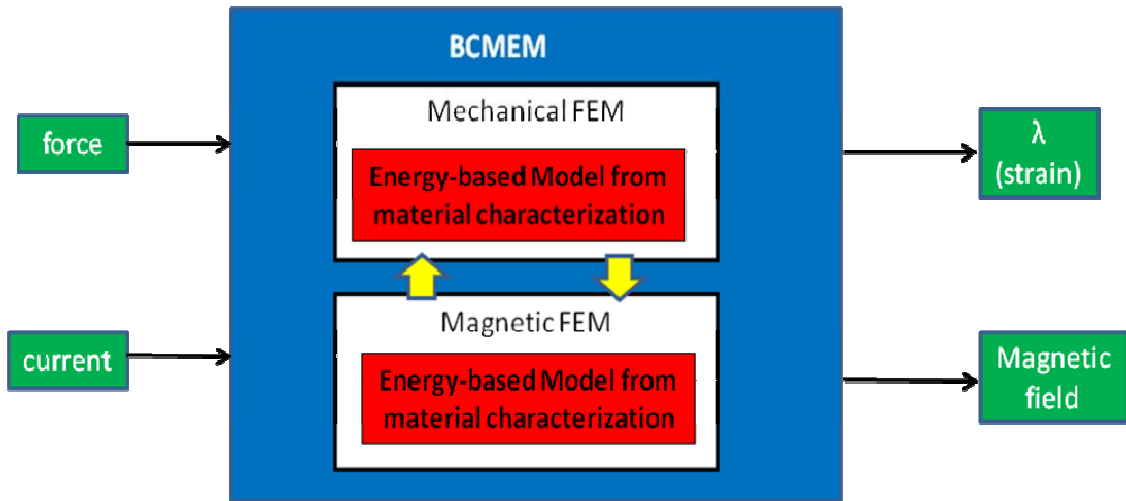
Figure 2.18. Flow chart of BCMEM ideas from Chapter 2

Chapter 3: The BCMEM

     As discussed previously, modeling of magnetostrictive behavior requires the solutions to both magnetic and mechanical BVPs. Both FEM problems are discussed in detail in this chapter. The coupling of the problems is conducted using a script based language (COMSOL Script 1.2). The BCMEM model formulation is discussed as well as the model convergence parameters. This chapter also includes a discussion on the boundary, loading, and current conditions used in the BCMEM.

3.1 – Magnetic and mechanical BVPs

     Most actuators use a current carrying coil to produce a magnetic field in a magnetic material. For a coil of infinite length, the magnetic field in its core is assumed to be H = nI, where n is the number of turns per unit length of the coil, and I is the current passed through the coil. FEM modeling of finite length coils will be implemented with the coil current density J (units of A/m^2) instead of current I, with coil design considerations left for future work. The use of FEM software will allow one to accurately model the differences between coil setups of different dimensions.

     The model discussed in Section 1.5.6 is not capable of handling current carrying cases since the reduced form of Maxwell equations that were used eliminate the current carrying term (J). This research investigates the extension of the model created by Mudivarthi et al. [2] to handle current carrying applications. The original, or full set of Maxwell equations, are listed below. Since the modeling done in this research only investigates quasi-static cases, the time dependent terms can be eliminated. Also, the use of a magnetic potential to describe the magnetic induction

51

as: $B = \nabla \times A$, will be useful here, as well as the constitutive relation $B = \mu_0 \mu_R H$.

The relevant equations are listed under the magnetic BVP equation section below.

$$\nabla \times H = J + \frac{\partial D}{\partial t} \quad \rightarrow \text{ Maxwell-Ampere's Law} \qquad (3.1)$$

$$\nabla \times E = -\frac{\partial B}{\partial t} \quad \rightarrow \text{ Faraday's law} \qquad (3.2)$$

$$\nabla \cdot D = \rho \quad \rightarrow \text{Electric form of Gauss's Law} \qquad (3.3)$$

$$\nabla \cdot B = 0 \quad \rightarrow \text{ Magnetic form of Gauss's Law} \qquad (3.4)$$

<u>Magnetic BVP</u>

$$\nabla \times H = J \qquad (3.5)$$

$$\nabla \cdot B = 0 \qquad (3.6)$$

$$B = \nabla \times A \qquad (3.7)$$

$$B = \mu_0 \mu_R (\sigma, B) H \qquad (3.8)$$

A rearranged form of Equation 3.8 is shown below as Equation 3.9. Inserting Equation 3.7 into Equation 3.9 gives Equation 3.10 below. Finally, substituting Equation 3.10 into Equation 3.5 gives Equation 3.11 below. The current density (J) is an input to the magnetostatics model. COMSOL uses J to solve for the magnetic potential (A) using Equation 3.11. Then, using Equation 3.7, COMSOL solves for the magnetic induction (B). Finally, the magnetic field (H) can be solved for with a knowledge of the stress condition from the mechanical model.

$$H = \frac{B}{\mu_0 \mu_R (\sigma, B)} \qquad (3.9)$$

$$H = \frac{\nabla \times A}{\mu_0 \mu_R (\sigma, B)} \qquad (3.10)$$

$$J = \nabla \times \left(\frac{\nabla \times A}{\mu_0 \mu_R (\sigma, B)} \right) \qquad (3.11)$$

Now the mechanical BVP will be investigated. A static equilibrium force balance will lead to Equation 3.12. Classical strain and displacement relations are used here, with strain equal to the gradient of the displacement (Equation 3.13). However, there is a new contribution to strain due to magnetostriction, which must be incorporated into the mechanical model. When calculating the stress, it is necessary to subtract the contribution of magnetostriction from the corresponding strain in the direction of elongation (Equation 3.14). This is done by altering the equation system for the Galfenol subdomain only in the mechanical FEM.

Mechanical BVP

$$\nabla \cdot \sigma + F_{body} = 0 \qquad (3.12)$$

$$\varepsilon = \nabla u \qquad (3.13)$$

$$\sigma = E \left(\varepsilon - \lambda (\sigma, B) \right) \qquad (3.14)$$

To properly account for magnetoelastic coupling as discussed in Section 2.5, the magnetic and mechanical problems are coupled together by COMSOL Script 1.2.

This is a command based language similar to the MATLAB interface. The finite

element models can be imported to COMSOL Script. With the proper coding, the

magnetic and mechanical models can be coupled until a converged solution is

reached. COMSOL Script will be discussed in more detail in Section 3.7.

3.2 – BCMEM Model flow chart

The bidirectional modeling approach used in the development of the BCMEM

is outlined in Figure 3.1. This type of modeling requires bidirectional coupling

between the previously described mechanical and magnetic BVPs.   The bidirectional

model uses a major loop to couple two minor loops, which represent the mechanical

and magnetic problems. The magnetic and mechanical BVPs as formulated in

Section 3.1 are iteratively solved until a specified convergence criterion is met. In the

case of bidirectional modeling it was determined that convergence of induced stress

and magnetic field would be the most important variables to monitor. A difference of

less than 1% in stress and magnetic field between iterations was used as the

convergence criterion. The values of stress and magnetic field at the center of the

sample were used to determine the percentage difference between iteration. Figure

3.2 illustrates the convergence of stress and field for a typical BCMEM run. Despite

a relatively strict convergence parameter, the model still proved to be computationally

efficient, as only eight iterations were required for convergence.
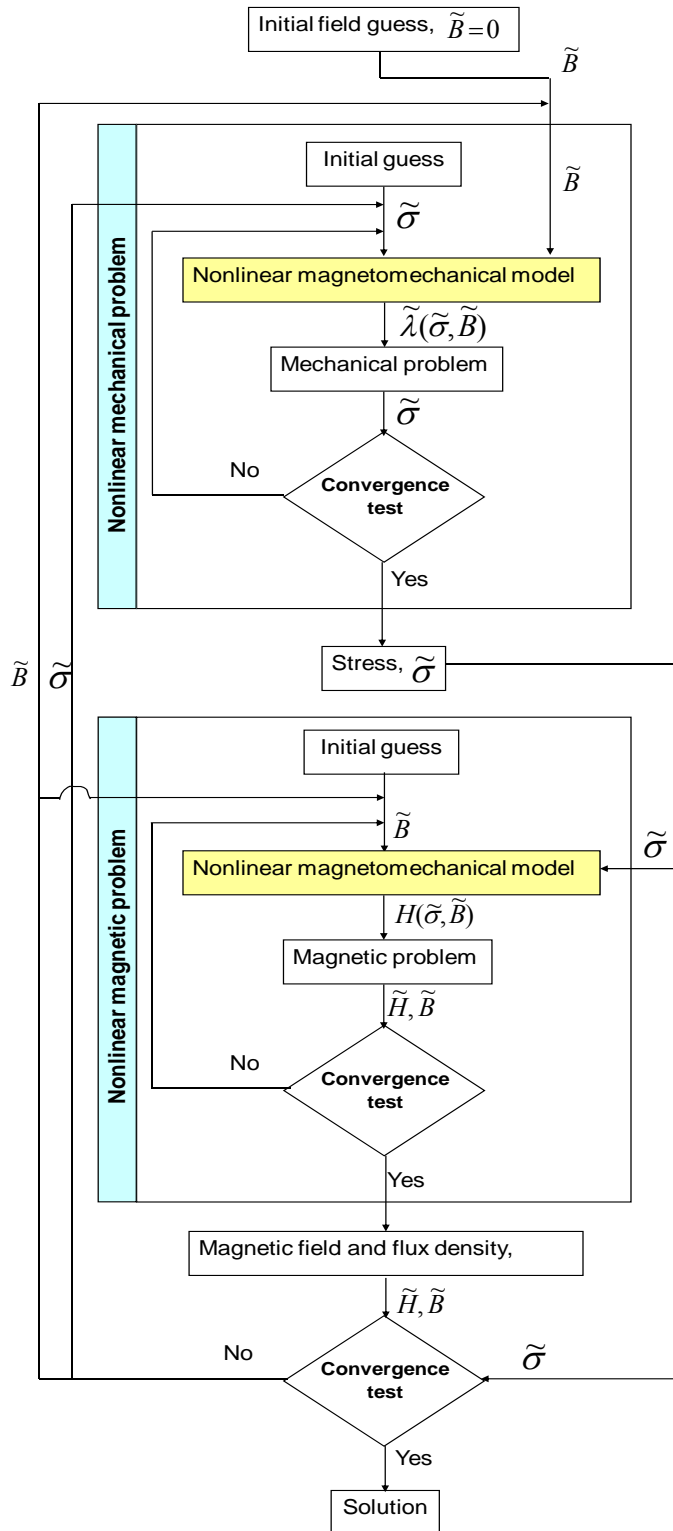
Figure 3.1. Flowchart of BCMEM with two minor iterative loops embedded in a major iterative loop
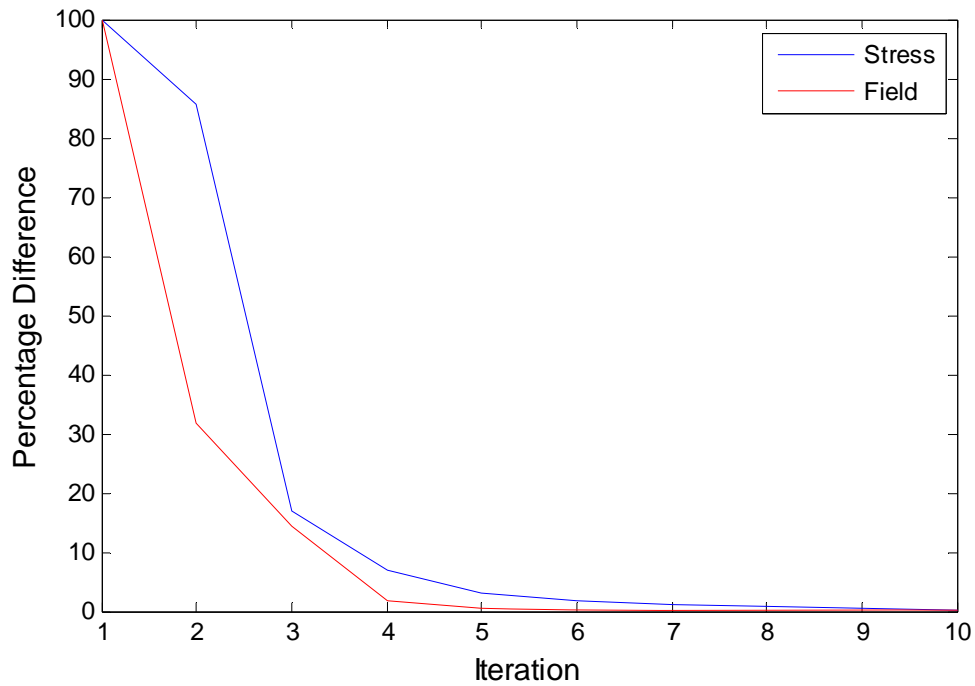
Figure 3.2. Percentage difference between iterations of stress and magnetic field

3.2.1 – Special unidirectional model cases

Although the BCMEM can handle any boundary condition, there are two notable cases which eliminate the need for the major iterative loop in Figure 3.1. These two cases arise when the solution of only one of the BVPs affects the other and thus require only one iteration before a solution is reached. Case 1 applies when the mechanical BVP solution affects the magnetic BVP solution but the resulting magnetic solution has no effect on the mechanical solution. This modeling approach can be used only when the applied magnetic field does not induce any change in stress in the sample, which is possible only when magnetostriction is not impeded. Case 2 applies when the magnetic BVP solution affects the mechanical BVP solution but the resulting mechanical solution has no effect on the magnetic solution. This

modeling approach can be used only when the internal field in the sample is held constant using a feedback controller.

3.3 – BCMEM Boundary Conditions

Boundary conditions can be applied to nodes, edges, boundaries, subdomains, points, or lines. For the purposes of the mechanical model studied in this research, only the fixed edge and simply supported line boundary conditions were used.

The fixed boundary condition was used to model the blocked stress of Galfenol, where a fixed-fixed condition was simulated. Chapter 4 discusses the modeling of the blocked stress as well as other loading schemes that make up the actuator load line. This model was a 2D axisymmetric model and therefore, the fixed-fixed boundary condition was simulated by fixing the top and bottom boundaries of the sample. The fixed boundary condition ensures that the specified locations (i.e., nodes, boundaries, etc.) do not displace or rotate in any direction.

The simply supported boundary condition ensures no vertical displacement, but allows for rotation. This boundary condition was used to model the four-point bending setup which will be discussed in more detail in Chapter 5.

There are several magnetic boundary conditions that need to be implemented in the magnetostatics model. This research involves the use of a 2D axisymmetric model for purposes of simulating actuator load lines (Chapter 4), and a 3D model for purposes of analyzing a four-point bending setup (Chapter 5).

The 2D axisymmetric model boundary conditions are outlined in Figure 3.3 where a simple rod and coil setup is shown. The rod and coil setup is surrounded by

an air domain. The air domain is a region of air ($\mu_R = 1$), where the magnetic flux

lines are not permitted to exit. Since the magnetic field lines are constrained to stay

within the air domain, the outer edges of the air domains enforce a flux line flow

tangency condition where the tangent component of the magnetic potential is zero (n

x A = 0). This is known as magnetic insulation. An investigation of Figure 3.3 will

show that the outer edges of the air domain properly ensure the flux line flow

tangency condition.

Atulasimha [14] has shown appropriate air domain sizing techniques that are

used in this research. The sizing of the air domain was determined to optimize the

computational efficiency by using the smallest air domain that still yields accurate

results. The air domain has dimensions that are three times the largest dimension of

the transducer setup. In this case, a 2-inch long rod was used, which presents the

largest dimension, thus the air domain was chosen to be 6-inches by 6-inches.

However, since this is a 2D axisymmetric model, a rectangle represents a cylinder, so

the air domain is a cylinder with a diameter of six inches and a height of six inches.

When using a 2D axisymmetric model, it is assumed that the magnetic

solution does not vary azimuthally. Because of this symmetric assumption the

modeling considers only a cross section of the magnetostatic problem. Due to the

symmetric assumptions of the magnetostatic solution, an axisymmetric boundary

condition is used. This boundary condition was applied to the r = 0 center line. This

boundary condition is generally set by default.

A continuity boundary condition is used to define the junction between two

subdomains (or separate geometries). This boundary condition enforces continuity of

the tangential component of the magnetic field via: n x (H_2 – H_1) = 0 between two boundaries, where n is the unit normal vector.

The 3D model used in this research uses the same boundary conditions as the 2D axisymmetric model except for requiring axial symmetry at r = 0 since the 3D magnetic solution is assumed to vary azimuthally.
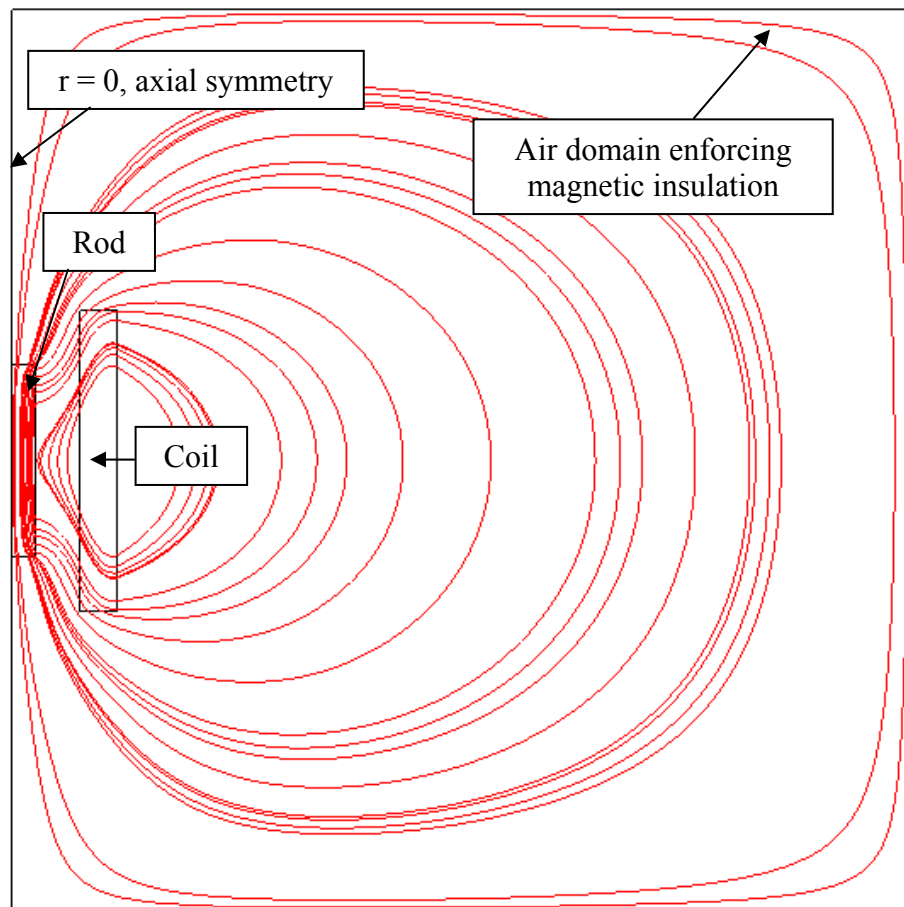
Figure 3.3. Boundary conditions for 2D axisymmetric, magnetostatics (with currents) model.

3.4 – Loading and current density

This section discusses the different inputs to the mechanical and magnetic models. Since the finite element method is being used, force and current density become the inputs to the mechanical and magnetic models respectively. These models solve for the stress and magnetic field distributions respectively. Other variables such as strain and magnetic induction can also be determined.

In a static model there are several ways to apply a load. A load can be applied to a node, edge, boundary, subdomain, point, or line. Note that these are the same locations at which boundary conditions can be applied. The units of the force vary depending what type of load is applied. A node or point load has the units of (N) or (lb), an edge load has the units of (N/m) or (lb/ft), a boundary load has the units of (N/m^2) or (lb/ft^2), and a subdomain load has units of (N/m^3) or (lb/ft^3).

In a magnetostatics model, a current density can be applied to a subdomain in either 2D or 3D. The current density provides the magnetic field to the sample as discussed in Section 3.1. In a 2D axisymmetric model, the current is assigned to the cross-section of the coil with units of A/m^2. In 3D, one must assign the current density on with respect to the x-y-z direction coordinate system J_x, J_y, and J_z based on a magnitude of current density, J (A/m^2). Since the units of current density are A/m^2, the number of turns in the coil is not modeled using FEM. Instead, only the amount of current per unit area is considered. Applying current densities in 2D and 3D will be discussed in more detail in Chapters 4 and 5 respectively.

3.5 – Development of λ-H and B-H interpolation files for BCMEM

A material model is needed to correctly depict the λ-H and B-H behavior of Galfenol for the BCMEM. It was shown in Section 2.1 that the highly nonlinear behavior of Galfenol is modeled well by fitting the Armstrong energy-based model to experimental λ-H and B-H characterization curves.

COMSOL Multiphysics 3.4 allows for the user to input B-H data to describe material magnetic behavior. This was not the case on earlier versions of COMSOL where one had to describe the behavior of a magnetic material in terms of relative permeability. For example, the work done by Mudivarthi et al. [2] used COMSOL Multiphysics 3.3, where the magnetic model required relative permeability (μ_R) as a function of H and σ, whereas now, with version 3.4 of COMSOL Multiphysics available, the model will determine μ_R directly from the B-H plots for each stress. However, to input a B-H plot, it must be in the form of H(B,σ), which requires a conversion of the Armstrong model output of B(H,σ) to H(B,σ). This matrix conversion is a novel task that can be done using MATLAB. A similar matrix conversion was done for the λ(H,σ) matrix to obtain a λ(B,σ) matrix.

There are several ways for COMSOL Multiphysics 3.4 to read the material data. These methods include the use of a table, MATLAB function, or text file. The previous BCMEM created by [2], makes use of MATLAB functions to calculate λ(H,σ) and B(H,σ). In this work, a text file was used for purposes of determining λ(B,σ) and H(B,σ). The basic format of the text file is as follows for an interpolation as a function of two variables (i.e., z = f(x,y), refer to example below). All of the independent variables are listed under the Grid section. Each variable is listed in

61

ascending order in its own row. All of the combinations of dependent solutions of the

independent variables are listed under the Data section. This procedure is repeated

until all of the possible x-y combinations have been accounted for. The size of the

text files can become very large as the number of independent data values becomes

large. However, the text file only needs to be loaded one time, and does not

significantly affect the computional efficiency of the model.

An example interpolation file is shown below. Consider creating an

interpolation file based on $\lambda(\sigma,B)$ data. Stress (σ) and magnetic induction (B) are the

independent variables and thus all possible σ and B values are listed under the Grid

section in ascending order.

Next, the data corresponding to each combination of magnetostriction (λ) due

to σ and B are listed under the Data section. The first row corresponds to the

magnetostriction due to the range of stresses σ_1 to σ_n for the first magnetic induction,

B_1. The stress is cylced through for each magnetic induction until B_n is reached. This

completes the creation of the interpolation file for $\lambda(\sigma,B)$.

% Grid
σ_1 σ_2 ….. σ_n
B_1 B_2 ….. B_n
% Data
$\lambda(\sigma_1, B_1)$ $\lambda(\sigma_2, B_1)$ ….. $\lambda(\sigma_n, B_1)$
$\lambda(\sigma_1, B_2)$ $\lambda(\sigma_2, B_2)$ ….. $\lambda(\sigma_n, B_2)$
……..
……..
……..
$\lambda(\sigma_1, B_n)$ $\lambda(\sigma_2, B_n)$ …… $\lambda(\sigma_n, B_n)$

3.6 – Meshing

A benefit of the finite element method is the ability to discretize the problem into several parts. This allows for a more computationally efficient solution than a uniform distribution of properties. This section analyzes how an understanding of meshing properties is fundamental to obtaining an accurate and computationally efficient solution.

A mesh is a discretization of a geometry into pieces known as elements. Each element contains nodes which help to define the relationships of the key variables of the problem. In a 2D model, the most traditionally used elements are triangular and rectangular. Most triangular elements contain either three, six or seven nodes. Rectangular elements contain generally either four, eight, or nine nodes. A 3D mesh generally contains tetragonal or brick elements.

Consider the case of a 2D axisymmetric magnetostatics model containing triangular elements. The scenario of a magnetic rod surrounded by a coil, as discussed in Section 2.3, will be used here. The rod is assigned a relative permeability of 50 (typical value of relative permeability is saturation of B-H curve for Galfenol single crystals), and the coil is assigned a current density of 3e6 A/m^2. This section analyzes the difference between using thee and six node triangular elements (Figure 3.4).

Figure 3.4. 3-node (left) and 6-node (right) 2D triangular element

There are several options to chose from when creating a mesh. The predefined free mesh parameters vary from extremely fine to extremely coarse. For this study a coarse mesh was implemented. Figures 3.5 – 3.7 below outline the element discretization of different types of predefined element sizes for a 2D axisymmetric rod and coil setup. Clearly, there is a tradeoff between computational efficiency and model accuracy, as a finer mesh normally requires more memory and computational time, but generally gives a more accurate solution.
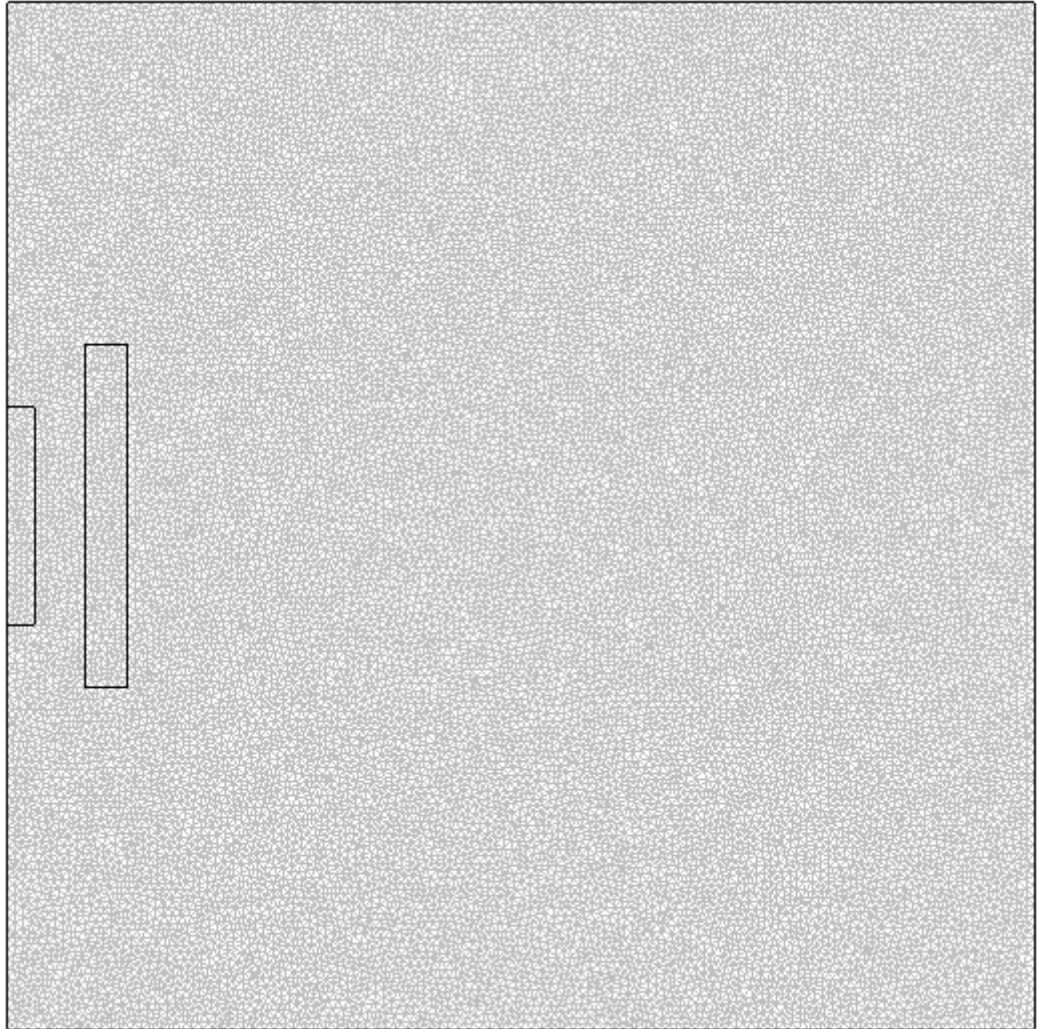
Figure 3.5. Extremely fine mesh
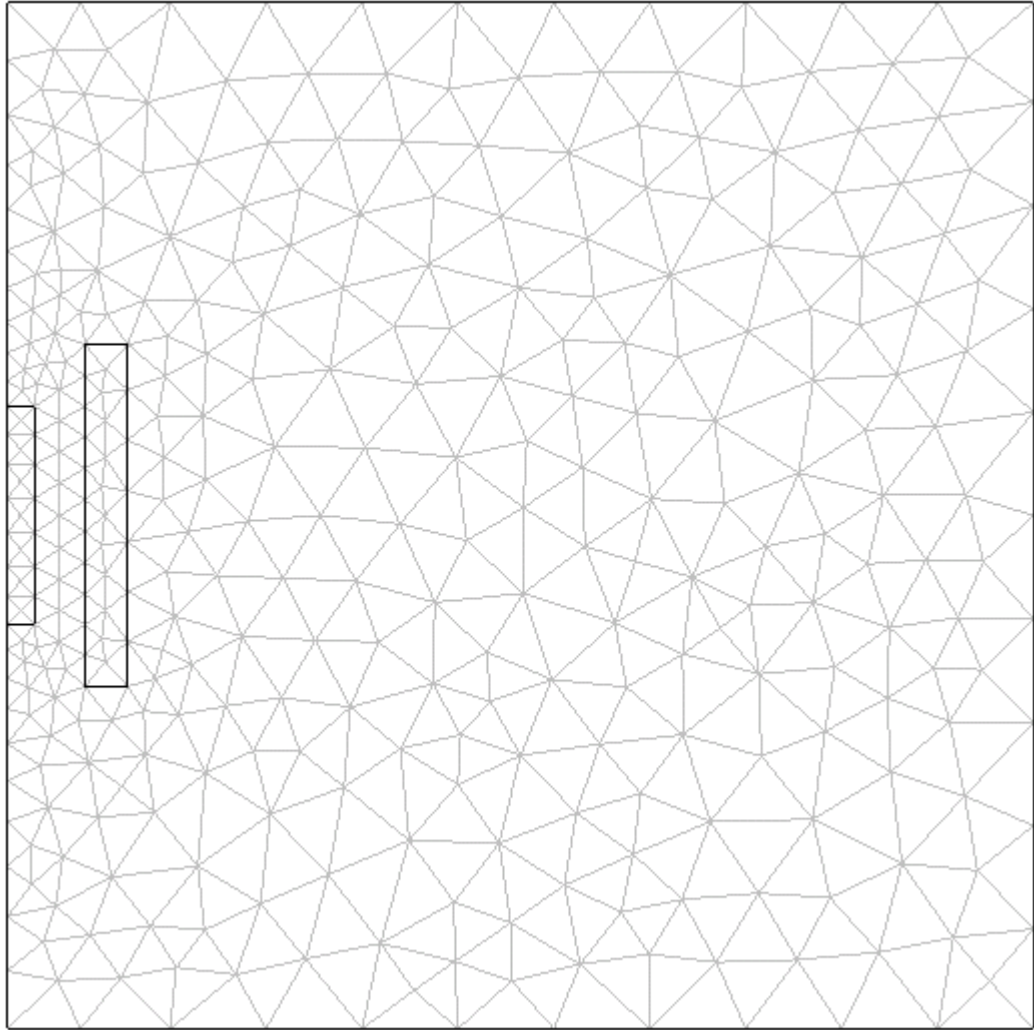
Figure 3.6. Coarse mesh
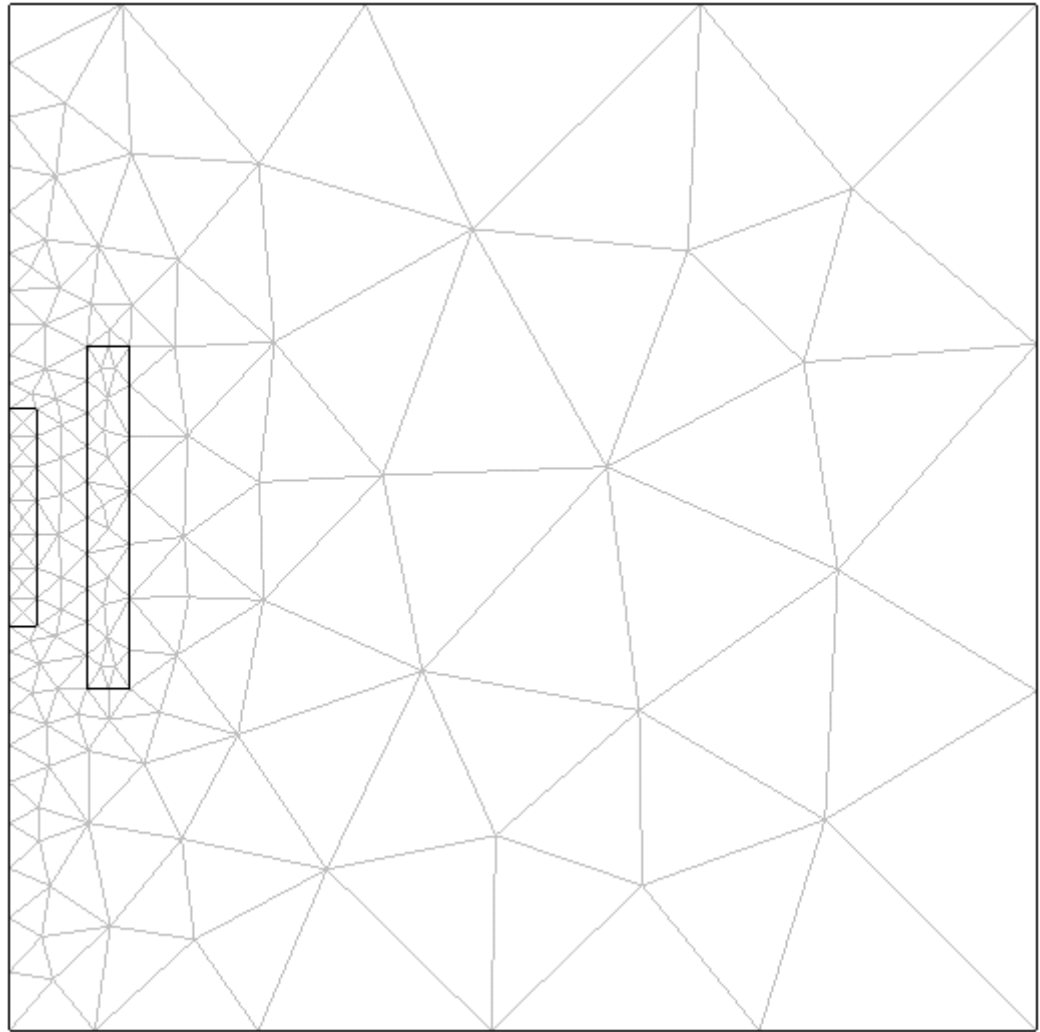
Figure 3.7. Extremely coarse mesh

When assigning a mesh to a geometry, one must also define what is known as

a shape function. A shape function defines the relationship between a particular

variable (stress, strain, magnetic field, magnetic induction, etc). The shape function

can be defined as linear, quadratic, cubic, etc.

First, consider the case of a 3-noded element (Figure 3.4). Pian and Lee [37]

have shown that the conventional elements such as 3-node triangular and 4-node

quadrilateral elements will lead a stiffness matrix with all infinite values. The

inability of these elements to give accurate results when dealing with incompressible problems should be considered when selecting a mesh type. The magnetic problem discussed in this research involves the magnetic form of Gauss's Equation (Equation 3.4), which employs an incompressibilty condition. Seeing this, one should avoid the use of conventional 3-node triangular and 4-node quadrilateral elements when solving magnetostatics problems.

Now consider the use of six-node triangular elements (Figure 3.4). Since there are three nodes defining each edge of the triangle, a parabolic relation can be defined. In Section 2.3, it was found that the magnetic field distribution along the length and radius of a cylindrical magnetic sample is parabolic in nature. Figures 3.8 – 3.10 show the magnetic field distributions along with the corresponding levels of mesh refinement. Finally, Figure 3.11 shows the mesh discretization within the Galfenol sample corresponding to the correct magnetic field distrbituion. The rest magnetic setup was meshed using the coarse baseline mesh. Since a 2D axisymmetric model is being used, the number of elements is greatly reduced (as opposed to using a 3D model), and the use of a 6-node element proved to yield a computationally efficient model.

One may pose the question: why are refinements needed here since a six node element defines a parabolic relation? The answer to this question is that this particlar study did not consider the variation of magnetic field along the height of the sample. Using a coarse mesh does not allow for enough elements along the height of the sample to correctly depict its magnetic behavior. Therefore, in this case, the mesh

refinements are needed to increase the number of elements along the length of the rod
to correctly depict the spatial variation of field.
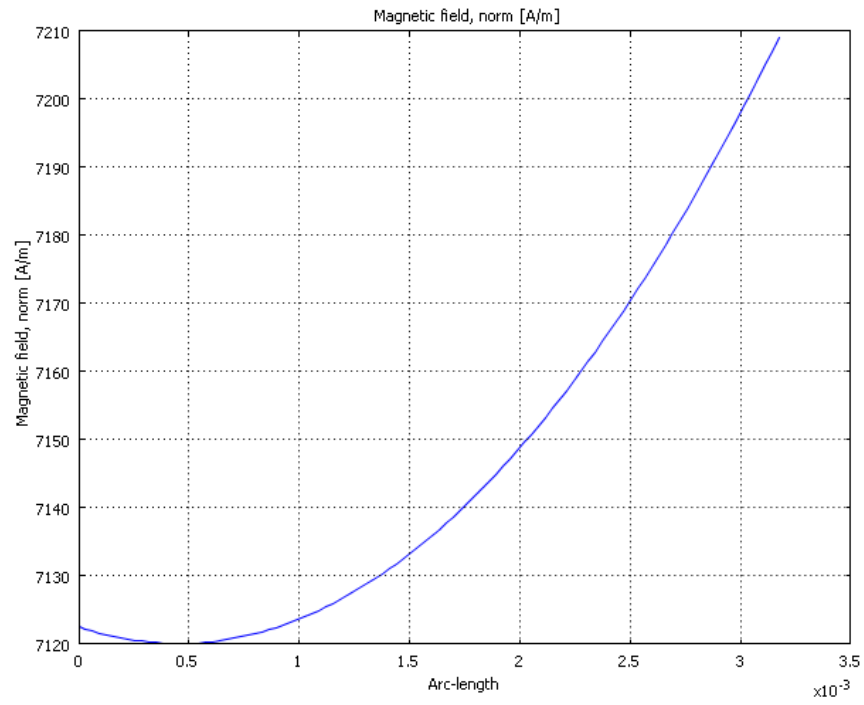
Figure 3.8. Field distribtion along radius with 6-node element, coarse mesh
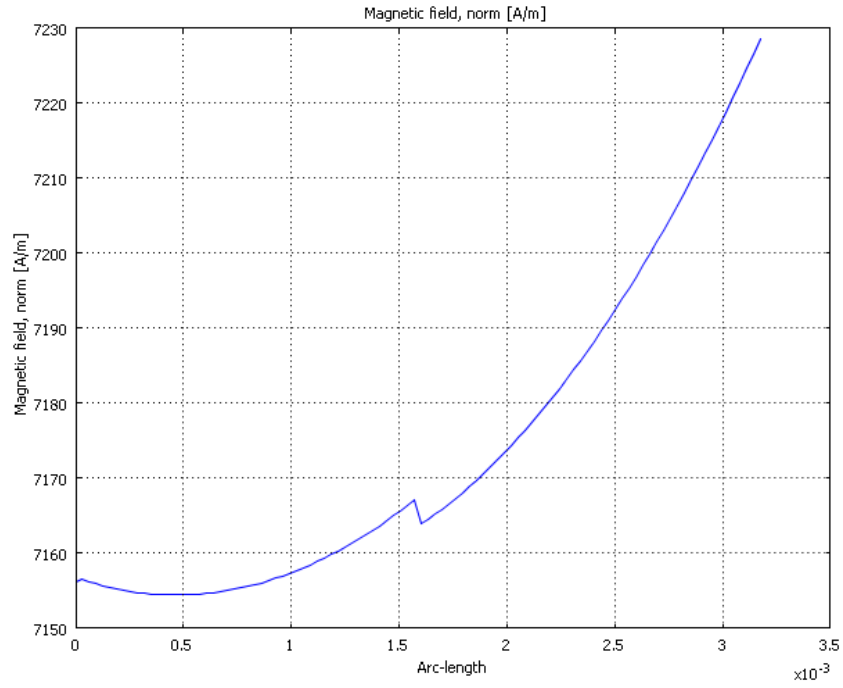
Figure 3.9. Field distribtion along radius with 6-node element, coarse mesh, one refinement
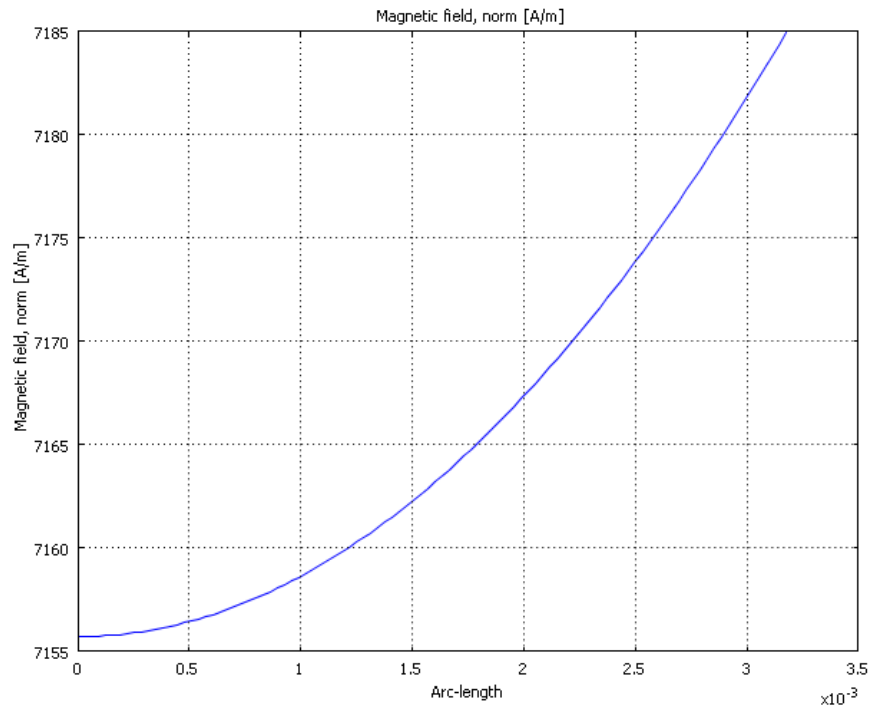
Figure 3.10. Field distribtion along radius with 6-node element, coarse mesh, three refinements

70
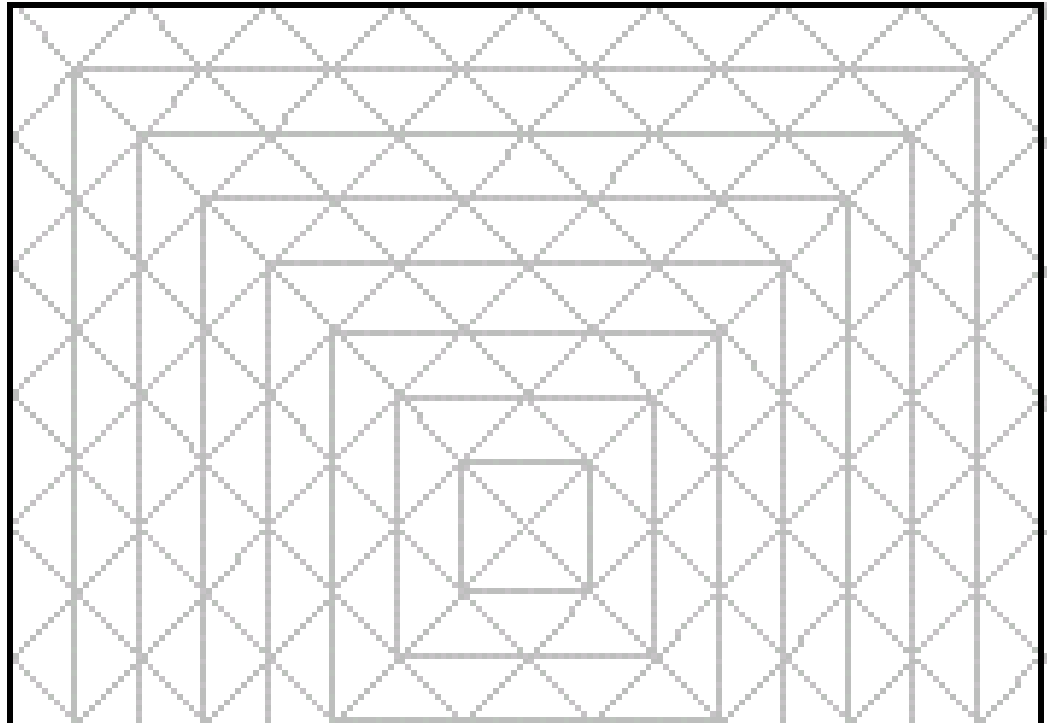
Figure 3.11. Mesh discretization of part of rod yielding the result in Figure 3.18

3.6.1 – Investigation of infinite elements versus use of air domain

When modeling a magnetic circuit, it is important to account for the surrounding atmosphere. Generally, this atmosphere is air, with a relative permeability of one. There have been several ways to model the surrounding air in a magnetic circuit. The two most notable techniques are the use of an air domain and infinite elements.

As discussed in Section 3.3, an air domain serves as a boundary for the flux lines, which prevents them from flowing outside of the air domain. Instead, the flux lines flow tangential to the boundaries of the air domain. Atulasimha et al. [36] describes how to determine the proper dimensions of an air domain. The dimensions

of three times the largest dimension of the setup are said to be adequete to properly model the flux flow through air. Any air domain that is smaller than this will lead to an inaccurate solution.

Another method of modeling the surrounding air is by using infinite elements. Infinite elements are assigned to a small subdomain region which defines the outside of the setup. The outer domain containing infinite elements causes the domain to be stretched to infinity. This allows for the flux lines to flow as far as they normally would without constraints.

Consider again the rod and coil setup, with an air domain. Also consider if an additional subdomain is created which causes a thin domain on the outer geometry (Figure 3.12). The outer domain will have the same properties as air, but instead of normal elements, it will contain infinite elements. When solving the model, the region containing infinite elements is stretched to infinity, simulating an infinite air domain. The magnetic field streamlines are shown in Figure 3.13. It is clear that the infinite elements allow the flux lines to flow outside of the outer domain, which is expected. Because of this, there is no limit on the size of the outer domain. The outer infinite element boundary only needs to be big enough to surround the entire magnetic setup. Seeing this, the amount of elements needed to run a model using infinite elements is less than that needed for a model with an air domain. The use of infinite elements will greatly enhance the computational efficiency of the model, especially for larger setups.
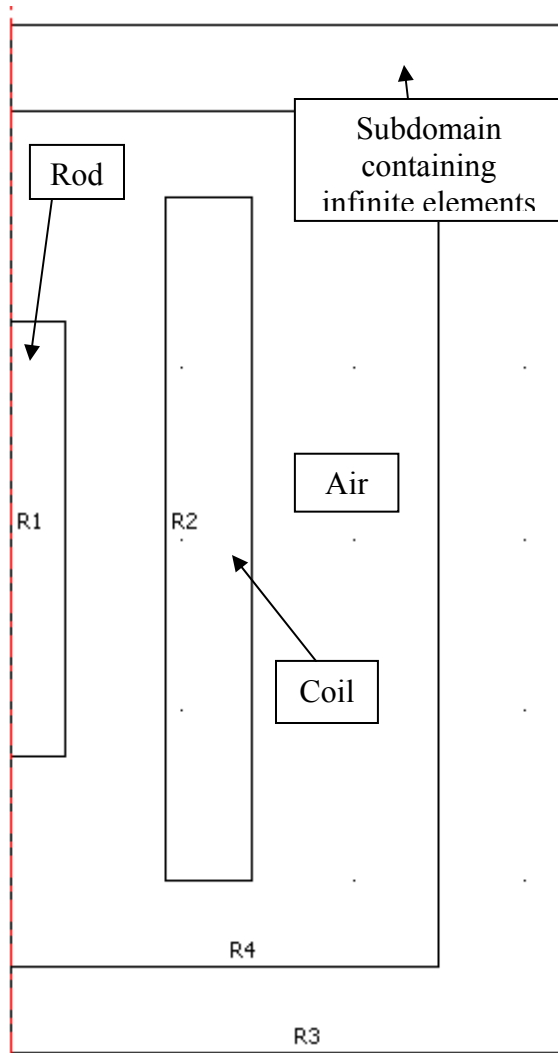
Figure 3.12. Rod and coil setup with infinite elements
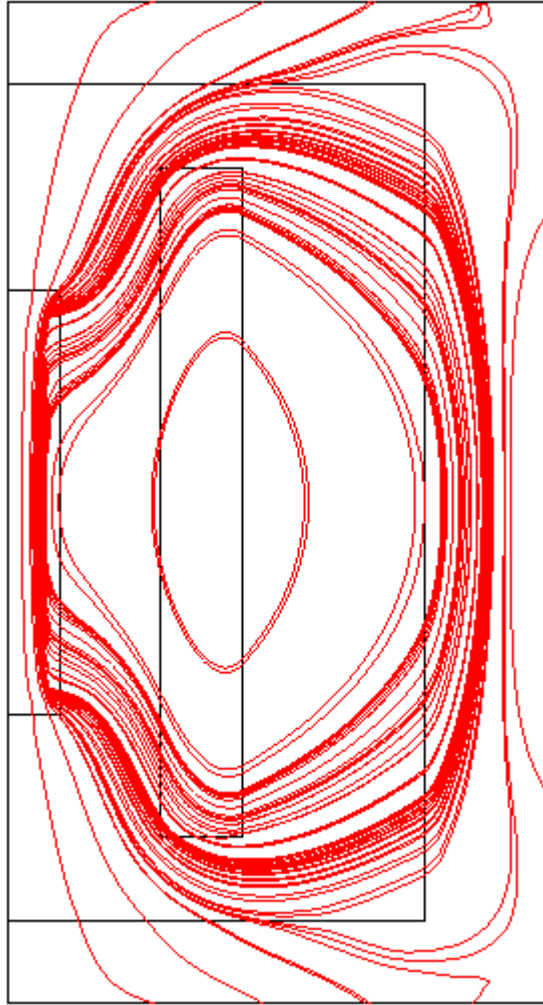
Figure 3.13. Magnetic field streamlines using infinite elements

It was desired to compare the two previously described methods of modeling the surrounding air domain. To do this, the rod and coil was implemented with infinite elements and with air domains of different sizes. The results are shown in Figure 3.14, where it was found that an air domain with dimensions of three times the largest geometric dimension of the setup gives same results as infinite elements. It was also desired to determine if larger applied current densities lead to the need for a larger air domain. In Figure 3.15, magnetic fields of ~7-7.2 kA/m are seen and the previously specified dimensions of the air domain still give a very good answer as compared to the infinite element result. Figure 3.15 shows the same plot as Figure 3.14, but at a higher applied magnetic field (~117-120 kA/m). Air domain sizing of three times the largest dimension in each direction still provides an accurate answer.

The use of infinite elements will generally reduce the total number of elements required in a magnetic model. Seeing this, models using infinite elements will generally prove to be more computationally efficient than using an air domain. However, infinite elements take longer to solve than standard elements, so there is a tradeoff between using the two methods.
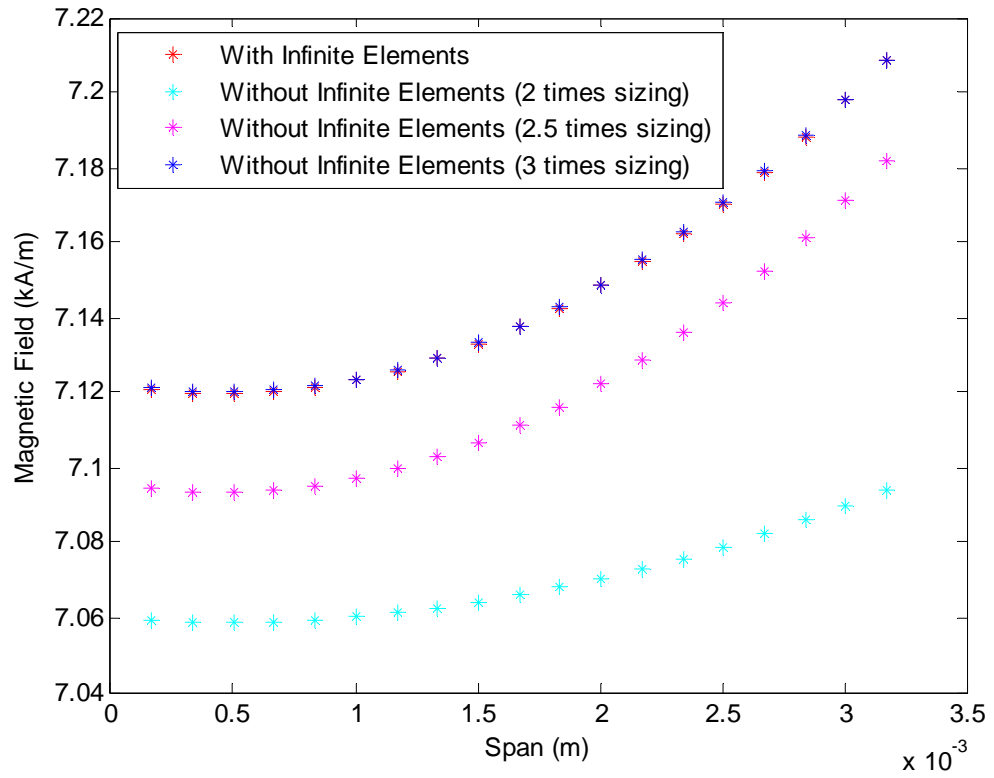
Figure 3.14. Radial distribution of magnetic field for rod and coil setup with air domain of different dimensions and infinite elements
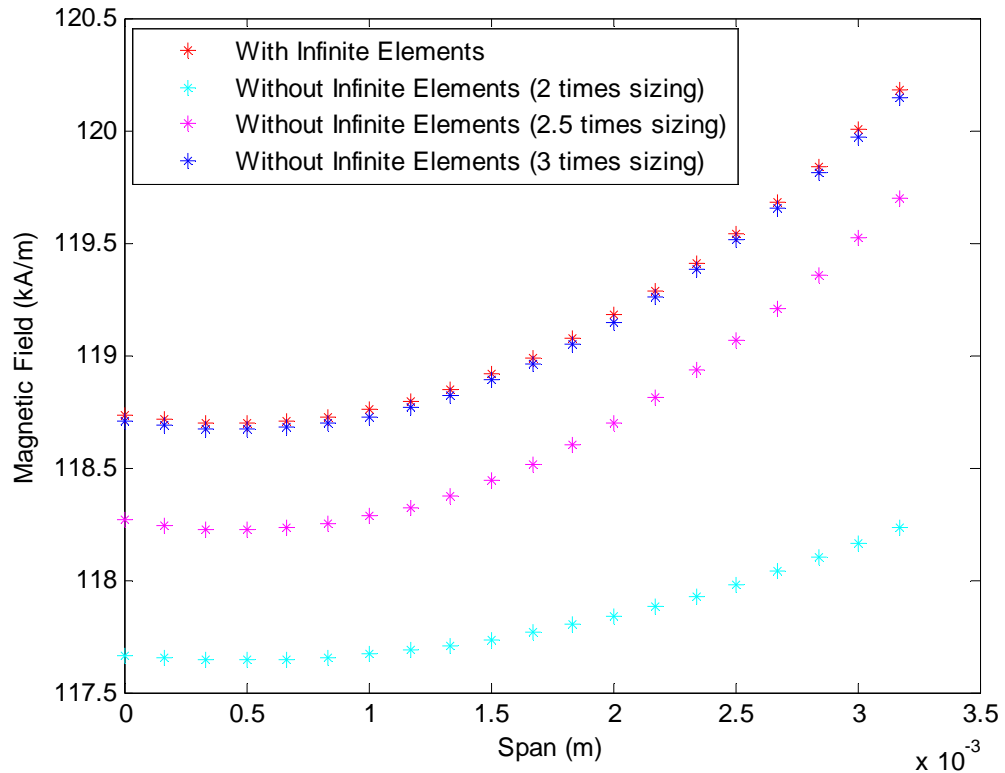
Figure 3.15. Radial distribution of magnetic field for rod and coil setup with air domain of different dimensions and infinite elements at high applied magnetic fields

3.7 – Using COMSOL Script 1.2 to couple magnetic and mechanical FEM

This section outlines the methods used in COMSOL Script to couple the mechanical and magnetic models.

When developing a magnetostrictive model, the key variables that one is interested in are the magnetostriction and magnetic field. However, as previously discussed, magnetostriction and magnetic field are both functions of magnetic induction and stress. This posses an interesting problem, as the solution of the magnetic model depends on the solution to the mechanical problem, and vice versa.

Further, as changes in magnetostriction and magnetic field occur, so do changes in stress and magnetic induction. This creates a bidirectionally coupled problem with the needed for a coupling capability to find a solution.

COMSOL Script 1.2 is a command based language with a wide range of capabilities. Although it may not be convenient to do so, an entire COMSOL Multiphysics model can be created, solved, and analyzed in COMSOL Script. This includes creating the geometry, meshing, assigning loads and boundary conditions, solving the model, postprocessing, etc. The BCMEM takes advantages of several of these capabilities.

The first step in creating a finite element model is to create the geometry. With the knowledge of geometry creating commands, this can be done in COMSOL Script, however, it is much easier to develop the geometry of the model using either COMSOL Multiphysics or a commercially available drawing software. The geometry for all of the models in this research were created in the COMSOL Multiphysics graphical user interface. Boundary and loading conditions as well as the meshing were also defined using COMSOL Multiphysics.

COMSOL Script becomes useful in the solving and postprocessing stages. Once the models are created, as described in the previous paragraph, they are imported into COMSOL Script. The BCMEM begins by solving the mechanical model under the assumption that there is no applied field. The solution to the mechanical model provides the initial stress states that are used to solve the first iteration of the magnetic model. Next, the mechanical model is solved again, but this time using the magnetic field solutions provided from the magnetic model. This

iterative process repeats until both the stress and field converge to within 1% between iterations.   The ability to use for and while loops and call functions that create interpolation files makes COMSOL Script very useful for this problem. Once a solution is reached, COMSOL Script makes data processing very easy. Data can easily be imported, exported, saved, and plotted.

To visually interpret the postprocessing results, COMSOL Multiphysics can be used to import the results. Contour, surface, streamline, and slice plots are just a few ways of visually interpreting the data.

Chapter 4: The Actuator Load Line

4.1 – Background information

The actuator load line is a plot that characterizes the relationship between force and displacement smart materials and actuators. As a background on actuator load lines, consider the Terfenol-D load-lines measured by Kellogg and Flatau [38] shown in Figure 4.1 for applied field levels increasing from 0 to 2400 Oe in steps of 200 Oe. The x-intercepts (finite strain, zero stress) in this figure correspond to the free displacement achieved by the actuator for a given magnetic field. The y-intercepts (zero strain, finite stress) correspond to the blocking force for the given magnetic field. Kellogg and Flatau [38] gathered this data by first applying the indicated magnetic field and then applying a compressive load until the total strain was reduced to zero. This load corresponds to what is defined as the blocking stress for the given applied field.
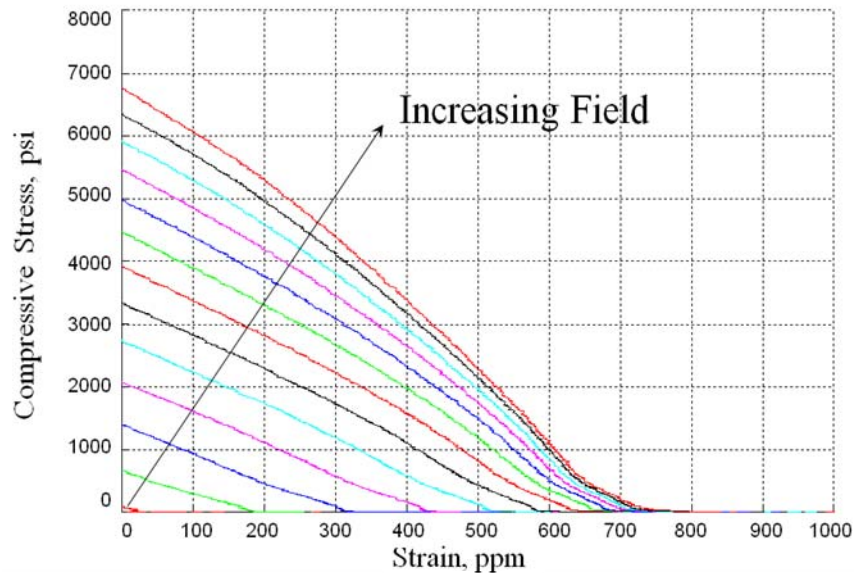
Figure 4.1. Terfenol-D actuator load line for fields ranging between 0 and 2400 Oe at steps of 200 Oe [38].

Traditionally the blocking stress is calculated based on the free strain and Young's Modulus of the material [3]. To calculate the blocked stress developed using this method, the free strain is multiplied by the Young's Modulus. However, variability in the slope of the load lines in Figure 4.1 indicates that the Young's Modulus is not always a constant value. Also, note that the relationship is nonlinear in nature exhibiting a noticeable kink near 650 ppm, and thus traditional assumptions for the development of a linear load line may not be an accurate means of predicting actuator performance. This relationship will be investigated in Galfenol, as discussed in the subsequent sections.

4.2 – Actuator load line of Galfenol

The experimental characterization of Galfenol load lines [32] involved measurement of strain of the sample under quasi-static compressive stress from zero to 120 MPa and back to zero at room temperature with a ramp rate of 2 MPa/s while the sample was subjected to DC bias magnetic fields of 0, 1, 3.5, 7.3, 17.8, and 71.2 kA/m. The compressive stress cycle was applied using a hydraulic MTS 810 universal testing machine in feedback force-control mode. The compressive force was measured using a load cell. The stress in the sample was calculated from the ratio of the measured values of force and the cross section area (3.07×10^{-5} m^2) of the sample. The strain in the sample was measured by two resistive strain gages attached in a quarter bridge configuration on opposite sides of the rod at mid-length to counter the effect of any bending moment. A linear Hall-effect sensor placed parallel to the sample measured the magnetic field. Although the Hall-effect sensor is measuring the

field in air, the sensor is placed on the surface of the Galfenol. It has been shown via Ampere's Law (Equation 4.1) and Stokes Theorem (4.2) that the tangential component of magnetic field is conserved across a boundary defining the interface of two materials with different permeabilities (Equation 4.4) [39]. The current density term is omitted from Equation 4.1 since there is no current being applied between the Galfenol sample and air. Figure 4.2 gives a pictorial representation of the continuity condition of the tangential components of magnetic field between two boundaries with different permeabilities.

$$\nabla \times \overrightarrow{H} = 0 \tag{4.1}$$

$$\int_{\Omega} \left(\nabla \times \overrightarrow{H} \right) d\overrightarrow{S} = \oint_{d\Omega} \overrightarrow{H} \cdot \overrightarrow{dl} \tag{4.2}$$
$$= \oint_{d\Omega_1} \overrightarrow{H_1} \cdot \overrightarrow{dl} + \oint_{d\Omega_2} \overrightarrow{H_2} \cdot \overrightarrow{dl} = 0$$

$$\overrightarrow{H_1} \cdot \overrightarrow{dl} \equiv \left(H_{1t} \hat{t} + H_{1n} \hat{n} \right) \cdot dl\, \hat{t} = H_{1t} dl \tag{4.3}$$

$$\overrightarrow{H_2} \cdot \overrightarrow{dl} = -H_{2t} dl \tag{4.4}$$
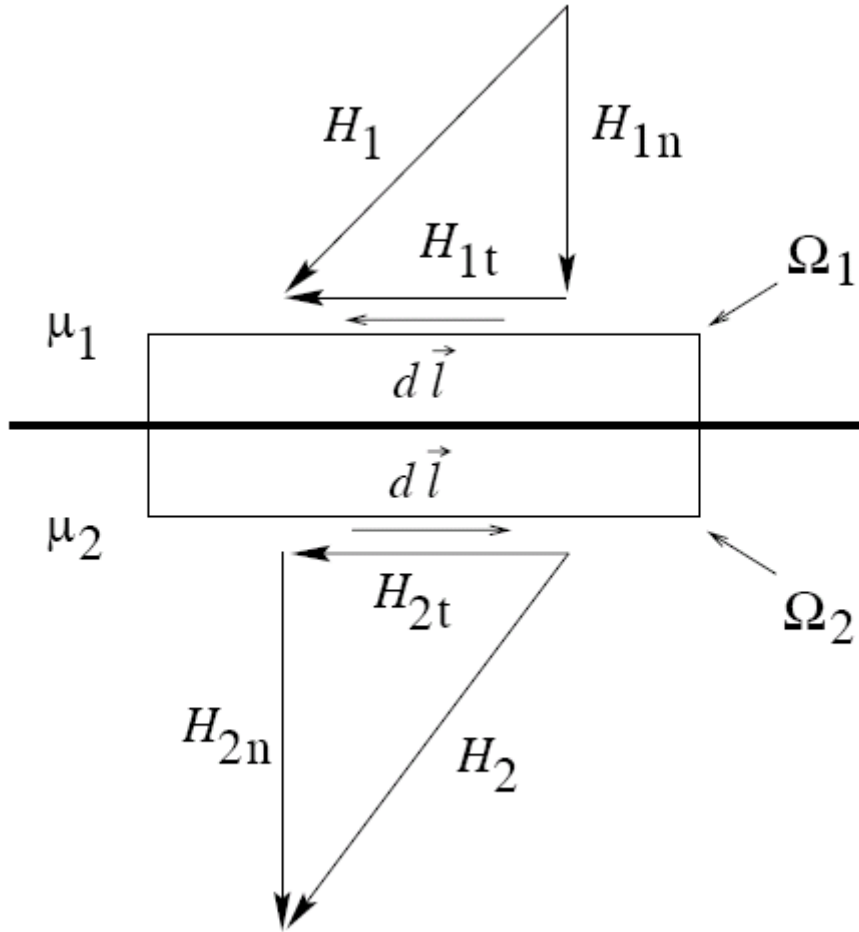
Figure 4.2. Continuity of the tangential component of magnetic field, $H_{1t} = H_{2t}$, across the boundary between two magnetic media of permeabilities μ_1 and μ_2.

The test sequence was comprised of 1) demagnetizing the sample followed by 2) applying the DC bias magnetic field and 3) cycling the stress. The demagnetization sequence consisted of cycling a magnetic field over 167 cycles using a 1 Hz sinusoidal signal which underwent a 5 % geometric decay every 1.5 cycles from an initial amplitude of 97 kA/m. The data was collected using a computer-controlled system at 50 scans per second. The DC bias magnetic fields were produced by applying a constant current to the drive coil of the transducer such that the desired field was obtained when the sample was at zero stress. This provided the no-load free

strain condition for the actuator load line for that DC bias condition. The blocked

force, zero-strain condition was determined from the subsequent application of

compressive stress as the condition at which strain was reduced back to zero. The

intermediate values stress-strain values were also recorded to create the full stress-

strain curve. Experimental results for the block stress and actuator load lines will be

shown in Section 4.3.3.

4.3 – BCMEM model of Galfenol actuator load line

It is known that changes in stress alter the magnetic state of a

magnetoelastically coupled material such as Galfenol. It was desired to model

Galfenol actuator load lines to test the BCMEM's capability of capturing this

coupling.

4.3.1 – Magnetic Model

The magnetic model was created using a 2D axisymmetric magnetostatics

(with currents) module. The magnetic setup consisted of the water cooled transducer

that has been discussed previously in this research (Figure 4.5). The air domain

(Figure 4.5) was assigned the dimensions of width and length equal to three times the

maximum dimension of the transducer. A more detailed explanation of the required

air domain dimensions can be found in [14]. The air and aluminum parts were

assigned a $\mu_R = 1$, steel casing a $\mu_R = 2000$, and the Galfenol rod was assigned a

variable permeability via $\mu_R(B,\sigma)$. The magnetic field is assigned via a current

density which has units of current per unit area. Both of the coils in Figure 4.3 were

assigned constant current densities such that the desired magnetic fields were applied to the Galfenol rod.
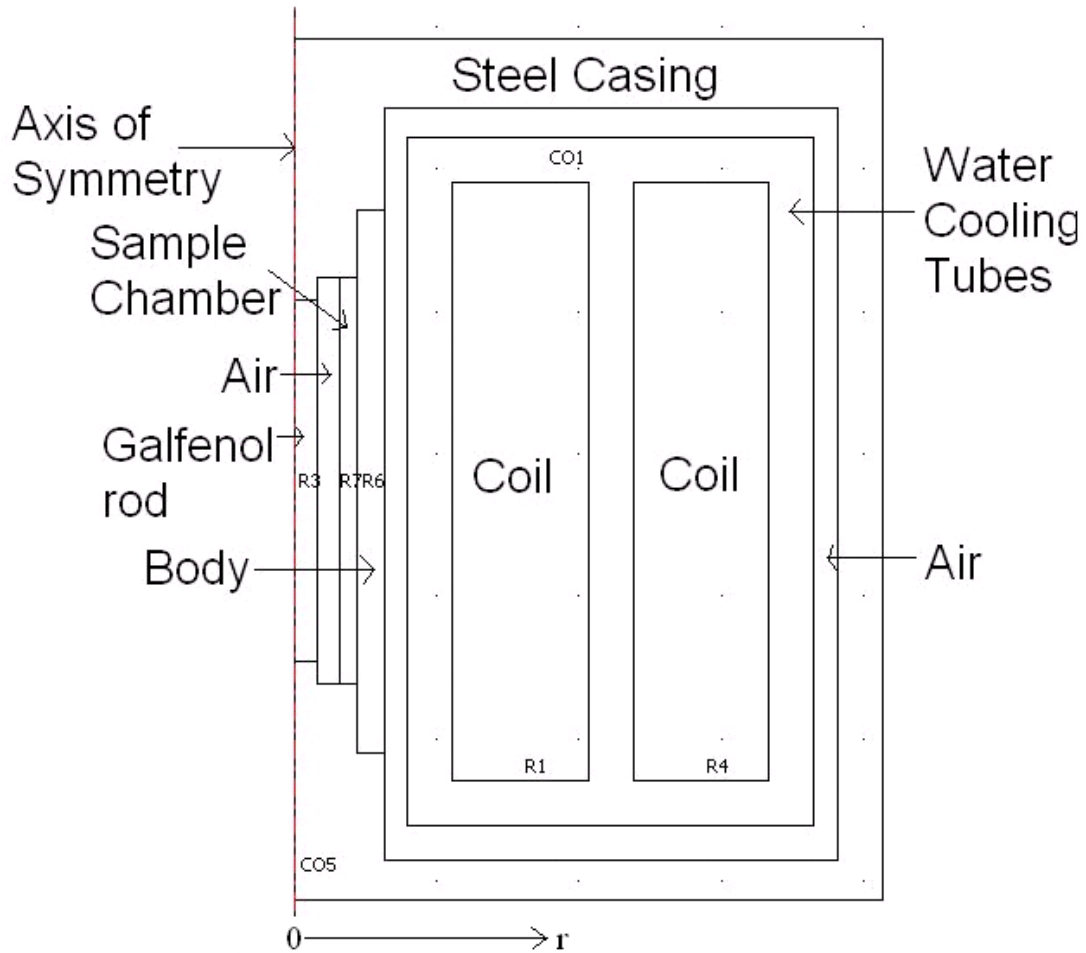
Figure 4.3. COMSOL 2D Axisymmetric Geometry of Water Cooled Transducer

Other important boundary conditions include axial symmetry and continuity. Axial symmetry is defined for 2D axisymmetric models at $r = 0$, and assumes a symmetric condition such that the properties of the system do not vary azimuthally. The continuity boundary condition enforces continuity of the tangential components

of the magnetic field via: n x (H$_2$ – H$_1$) = 0. This boundary condition is used at the junction of two different subdomains with different magnetic properties.

4.3.2– Mechanical Model

The 2D axisymmetric mechanical model consisted only of the Galfenol rod. Edge loads and boundary conditions were applied based on the particular point of interest on the actuator load line. For calculating the free strain condition, the fixed-free boundary condition was used, and no forces were applied to the rod. When calculating the blocked stress, the fixed-fixed boundary condition was used, and again, no forces were applied to the sample. For purposes of calculating all of the intermediate points along the actuator load line, a fixed-free condition was used, along with different applied compressive edge loads. The stress was again altered according to Equation 3.14 and is presented in the (r,z,φ) 2D-axisymmetric coordinate system in Equations 4.5-4.7, where φ is the azimuth angle.

$$\sigma_r = E \frac{(1-v)\varepsilon_r + v\varepsilon_\varphi + v(\varepsilon_z - \lambda)}{(1+v)(1-2v)} \qquad (4.5)$$

$$\sigma_z = E \frac{v\varepsilon_r + v\varepsilon_\varphi + (1-v)(\varepsilon_z - \lambda)}{(1+v)(1-2v)} \qquad (4.6)$$

$$\sigma_\varphi = E \frac{v\varepsilon_r + (1-v)\varepsilon_\varphi + v(\varepsilon_z - \lambda)}{(1+v)(1-2v)} \qquad (4.7)$$

4.3.3 – BCMEM predictions

Calculation of the blocking stress for a given applied field requires a model that includes the bidirectional magnetomechanical coupling effects. Hence this was deemed a suitable exercise to demonstrate the application of the BCMEM for use in conjunction with our on-going studies on the behavior of Galfenol. Additionally, using the approach taken by Kellogg, experimental data needed to validate the BCMEM predictions against measured Galfenol load lines can be readily obtained. Figure 4.4 shows a good correlation between the blocked stress determined experimentally and simulated using the BCMEM. Error bars are shown to 3σ.

The predicted actuator load lines are compared to those gathered experimentally for a single crystal $Fe_{84}Ga_{16}$ (Figure 4.5). The stress-strain curves predicted by the BCMEM are linear in nature. This is due to the fact that the compressive stresses induced were small and thus the linear range of the actuator load line in Figure 4.5 was used.
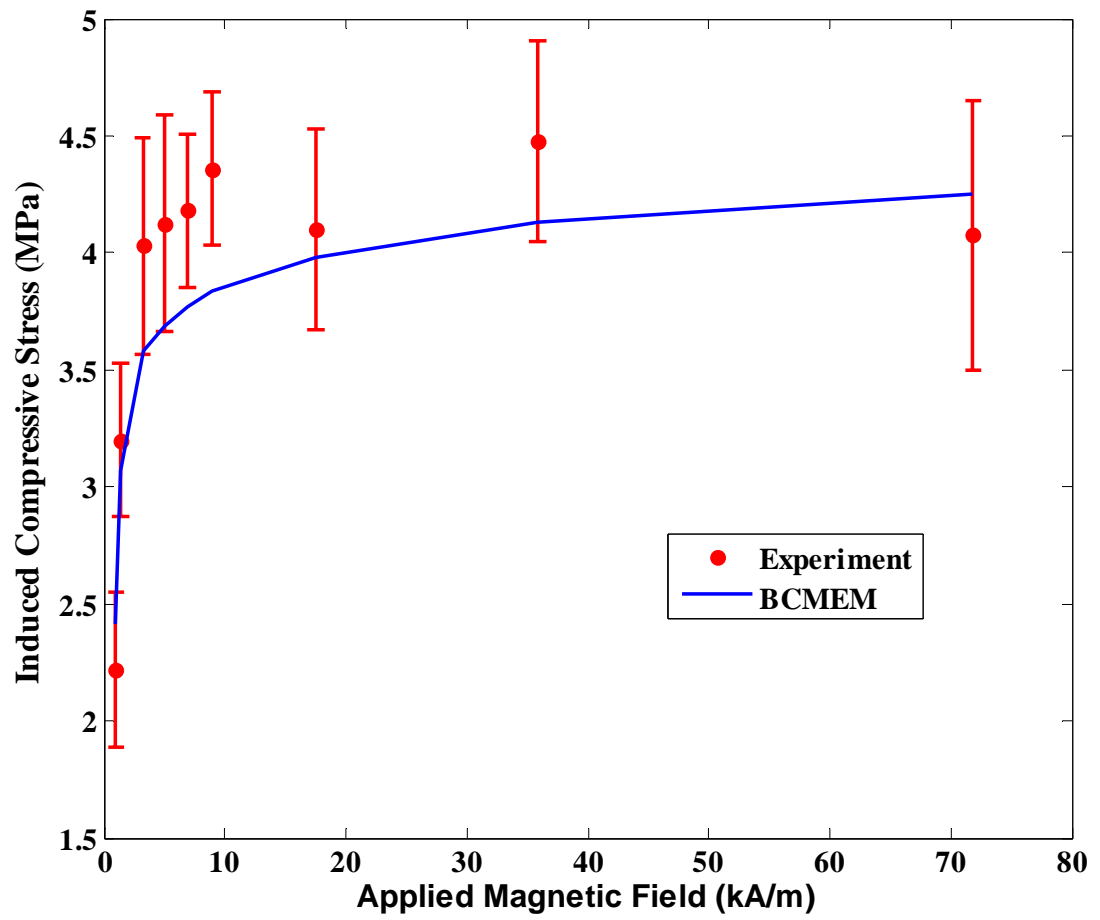
Figure 4.4. Experiment [32] and model predictions of blocked stress for initial bias magnetic fields
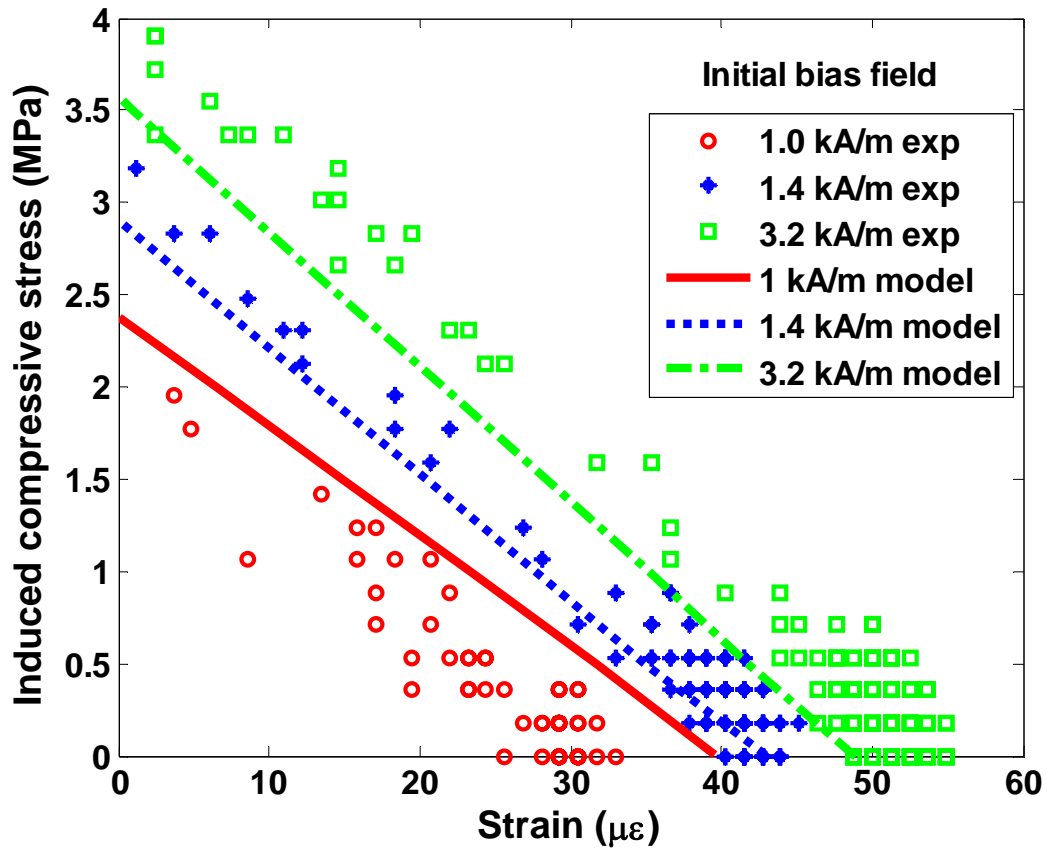
Figure 4.5. Experiment [32] and BCMEM actuator load lines for 1.0, 1.4, and 3.2 kA/m initial bias magnetic fields in Galfenol

Table 4.1 outlines the differences between the blocked force capabilities in Galfenol ($Fe_{84}Ga_{16}$ single crystal) and Terfenol-D ($Tb_{0.3}Dy_{0.7}Fe_{1.95}$). The Galfenol blocked stress values were obtained from the experimental data shown in Figure 4.4. The Terfenol-D blocked stresses were determined by recording the zero strain stress values for each actuator load line in Figure 4.1 [38]. To calculate the blocked force, the blocked stress was multiplied by the cross sectional area of the rods, which was the same as both samples have a radius of 0.25-inches. Terfenol-D can develop a much larger blocked force (1500-N for Terfenol-D compared with 140-N for

Galfenol). However, as outlined in Table 1.1, Terfenol-D is a very brittle material, while Galfenol is a very ductile material, making it suitable for applications involving bending and torsion.

Table 4.1. Comparison between Terfenol-D and Galfenol blocked force characteristics [38]

Galfenol ($Fe_{84}Ga_{16}$, 0.25-inch diameter)			Terfenol-D ($Tb_{0.3}Dy_{0.7}Fe_{1.95}$, 0.25-inch diameter)		
Field (kA/m)	Blocked Stress (Mpa)	Blocked Force (N)	Field (kA/m)	Blocked Stress (Mpa)	Blocked Force (N)
1	2.22	70.3	15.92	4.25	134.725
1.4	3.2	101.3	31.83	9	285.3
3.2	4.03	127.6	47.75	14	443.8
5	4.125	130.6	63.66	18	570.6
6.95	4.18	132.4	79.58	22.5	713.25
8.95	4.36	138.1	95.49	28	887.6
17.55	4.1	129.8	111.41	32	1014.4
35.85	4.475	141.7	127.32	35	1109.5
71.85	4.075	129.1	143.24	38	1204.6
			159.15	41	1299.7
			175.07	45	1426.5
			190.98	48	1521.6

4.2.1 – Delta-E effect in Galfenol

Upon validating the model capabilities, the BCMEM is used to investigate the ΔE effect in magnetostrictive materials and to study issues related to optimization of transducer magnetic circuits for improving device performance. The variability in the Young's Modulus of Galfenol has been documented well [40], but the capability of a

finite element model which accurately simulate this variability in the material's stiffness will assist in the future develop of applications.

Young's Modulus is a material property and is defined as the change in stress per change in strain with units typically of (N/m^2) or (psi). Although this property is a constant for conventional materials, it has been found to vary for certain materials that transduce energy between different states. This phenomenon has been given the name "delta-E effect" (ΔE-effect) [7]. Nickel and Iron have been shown to exhibit moderate changes in elasticity, on the order of 0.4-18%, whereas giant magnetostrictives such as Terfenol-D have been shown to exhibit much higher changes in the Young's modulus, on the order of ~150% [30], when only the effect of magnetic field on Young's modulus is considered. Galfenol has also shown to possess this effect with changes of Young's modulus of ~60% by Datta et al. [40], where the effect of both stress and magnetic field on Young's modulus is investigated.

The slopes of the load lines in Figure 4.7 for different applied magnetic fields are not the same. In turn, the apparent Young's modulus, i.e. change in stress per unit change in strain that can be determined from both experimental data and the BCMEM model for the different magnetic fields, will not be the same. This can be explained by recognizing the modulus, being equal to change in stress per unit strain, has contributions to the strain that are due to the superposition of purely elastic strain and magnetostrictive strain. It should be noted that the BCMEM incorporates a constant modulus in the mechanical model (76 GPa for $Fe_{84}Ga_{16}$), which is used to calculate the mechanical strain (Equation 4.8). However, the actuator load line is a plot of stress versus total strain, which is the sum of mechanical strain and magnetostrictive

strain (Equation 4.9). Thus, the apparent Young's modulus in the material is found by
dividing the induced stress by the total strain (Equation 4.10). Note that the apparent
Young's modulus is different than the purely mechanical Young's modulus used in the
mechanical BVP.

$$\varepsilon_{mech} = \frac{\sigma_{induced}}{E_{mech}} \tag{4.8}$$

$$\varepsilon_{total} = \varepsilon_{mech} + \lambda \tag{4.9}$$

$$E_{apparent} = \frac{\sigma_{induced}}{\varepsilon_{total}} \tag{4.10}$$

To investigate this phenomenon further, actuator load lines were simulated
using the BCMEM at applied magnetic fields of 1 kA/m and 71.75 kA/m (Figure
4.6). A relation for blocked stress can be derived by first considering Equation 4.11
as an alternate form of Equation 4.9. Rearranging Equation 4.11 and solving for
stress leads to Equation 4.12. Due to the fixed-fixed boundary condition required to
determine the blocked stress of a material, the total strain (ε_{total}) is equal to zero.
Setting $\varepsilon_{total} = 0$ in Equation 4.12 leads to an equation for blocked stress (Equation
4.13). Note that the minus sign in Equation 4.13 is indicative of that a compressive
stress was applied to the Galfenol sample to return it to zero strain. The blocked stress
(force) produced *by* the sample will be equal to but of the opposite sign to this
compress stress (force). Traditionally assumed cases represent a blocked stress that is
calculated using a magnetostrictive strain that is independent of stress (i.e., $\sigma_{block} = -$
$E_{mech}*\lambda(0,B)$). A comparison between the BCMEM and traditionally assumed cases

presented in Figure 4.6 shows that for Galfenol actuators, $-E_{mech}*\lambda(0,B)$ is a reasonable approximation for blocked stress at high applied field conditions. However, at lower applied fields, changes in magnetostriction as stress is induced in the material are larger in magnitude, and the BCMEM becomes a more appropriate means of predicting actuator performance. However, the magnitude of the differences between the traditional and BCMEM methods is not initially obvious, thus justifying the need for the BCMEM. Again, it is clear that the slopes of the actuator load lines at low and high magnetic fields shown in Figure 4.8 are different, which shows evidence of the ΔE effect.

$$\varepsilon_{total} = \frac{\sigma}{E_{mech}} + \lambda(\sigma, B) \qquad (4.11)$$

$$\sigma = E_{mech}\left(\varepsilon_{total} - \lambda(\sigma, B)\right) \qquad (4.12)$$

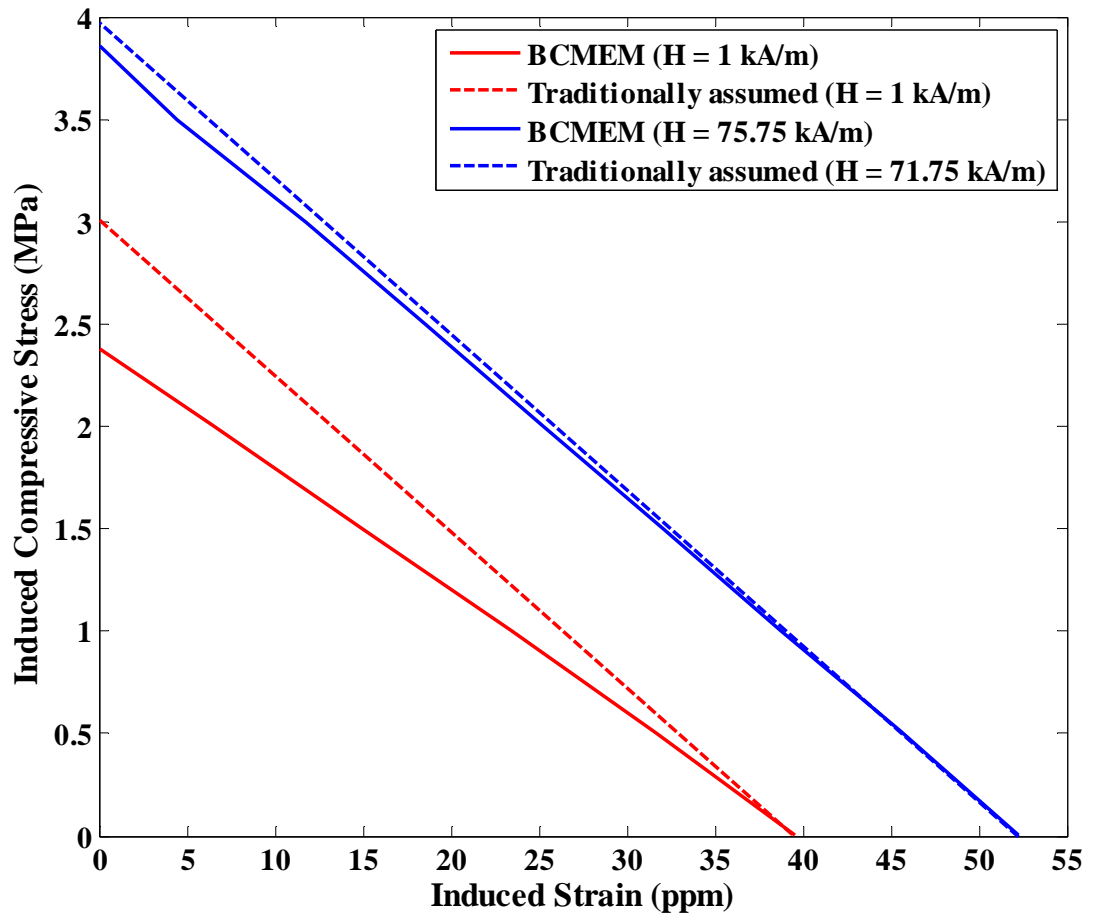$$\sigma_{block} = -E_{mech}\lambda(\sigma, B) \qquad (4.13)$$

Figure 4.6. Actuator load lines showing evidence of ΔE Effect in the BCMEM

Chapter 5: Four-Point Bending

Galfenol's high strength has made it a popular option for research in sensing and actuator applications involving bending. An understanding of the behavior of Galfenol under bending conditions is essential to the proper design of such devices. A four-point bending test is a method to experimentally characterize changes in the magnetic properties (magnetic induction) of Galfenol under a uniform bending moment load. This chapter discusses the experimental characterization of a single crystal 18.4% at. Ga parallelepiped sample and these results are compared to BCMEM predictions. The capability of a model to accurately capture the effect of bending on the properties of Galfenol will assist in the further development of Galfenol applications.

5.1 – Experimental setup and procedure

Four-point bending tests were conducted on a rectangular parallelepiped sample ($25x2x2$ mm^2) with its edges oriented along the <100> direction [41]. The goal of the experiment was to measure the change in magnetic induction that arose due to four-point bending loads. In a four point bending experiment (Figure 5.1), the beam is subjected to two loads on the top of the beam and is simply supported at the bottom of the beam at two locations. This creates compression on the top of the beam and tension on the bottom of the beam. One characteristic of this setup is that a region of constant bending moment appears between the locations of the two loading points. A bending moment diagram is shown in Figure 5.2. In a bending moment diagram, the magnitude of the bending moment at any location is equal to the area under the shear force diagram from position zero to the current position. In Figure

5.2, the region of constant bending has a magnitude of F*L, where L is the distance from the simply supported position to the loading position. The sense coil was placed in this region to measure the change in magnetic induction resulting from different applied bending moments. The magnetic setup included a solenoid which surrounds the electromagnet core which supplies magnetic field to the Galfenol sample. For a more detailed description of the experimental four-point bending setup refer to Datta et al. [41]. The experimental results will be shown along with the BCMEM predictions in the next section.
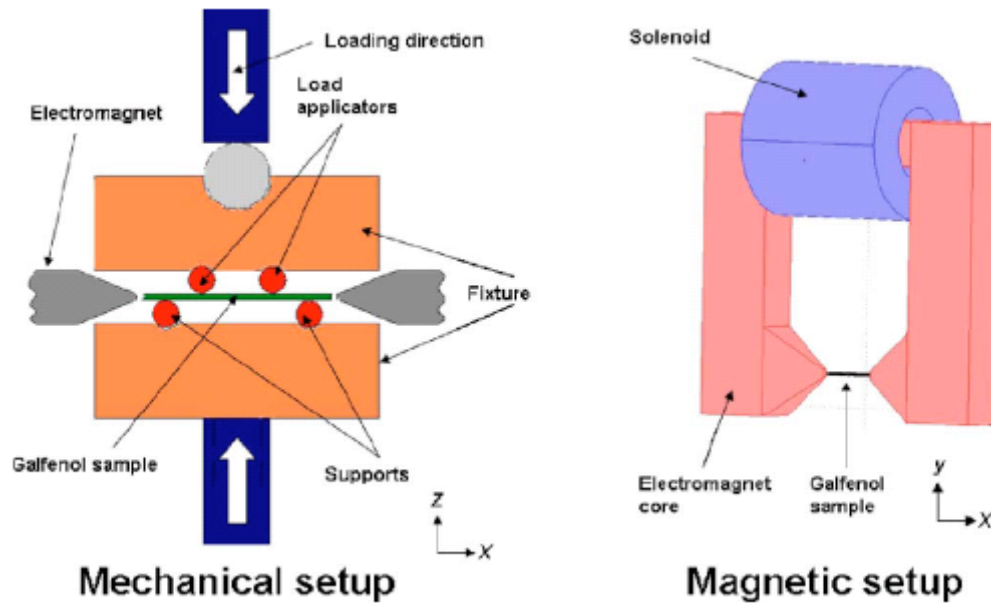

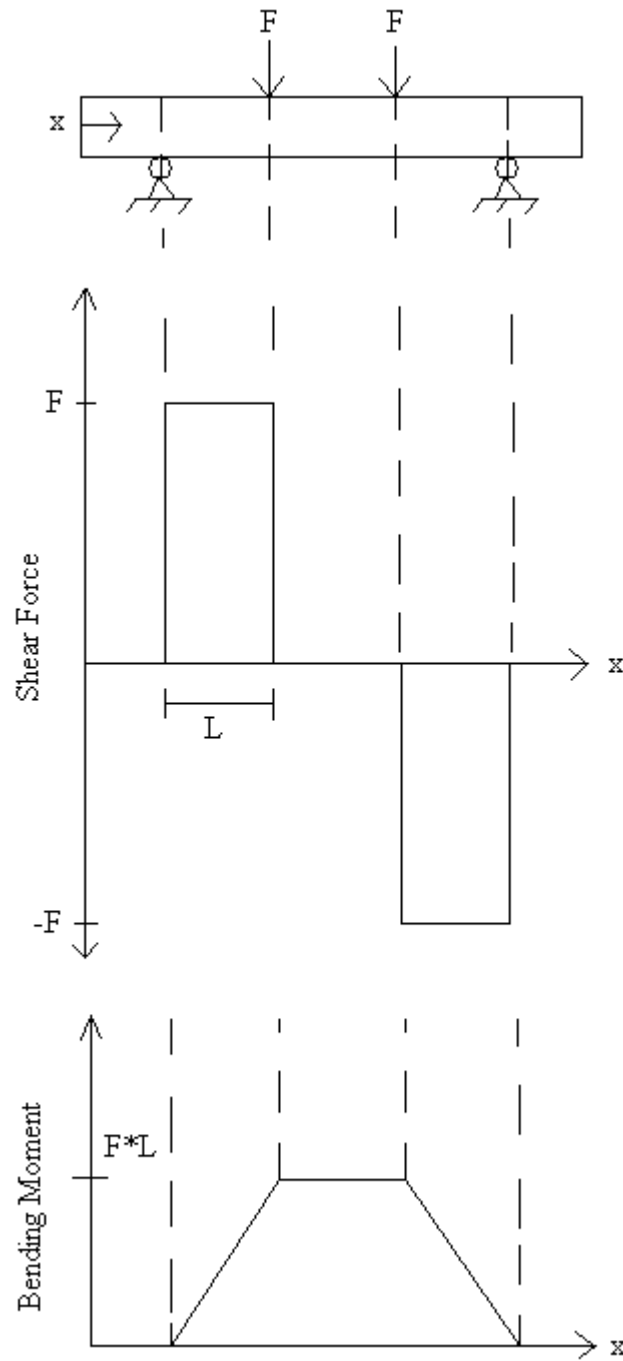**Figure 5.1.** Mechanical (left) and magnetic (right) setups for four-point bending test [41].

Figure 5.2. Bending moment diagram for a four-point bending setup.

5.2 – BCMEM setup and predictions

5.2.1 – Mechanical model

The geometry in the mechanical model consisted only of the Galfenol parallelepiped sample. For purposes of creating the mechanical model, it was unnecessary to model the other components in the magnetic setup (electromagnet and solenoid) as they do not contribute to the mechanical solution.

The loading conditions were simulated by applying line loads (N/m) to the top of the beam (Figure 5.3). The simply supported boundary condition was applied to two lines on the bottom of the beam. This boundary condition prevents vertical displacement, but does allow the beam to bend at the specified location. A constant hard modulus of 59 GPa was assigned to the $Fe_{81.6}Ga_{18.4}$ Galfenol rod. The x-direction is the direction of applied magnetic field and magnetostriction in this study and represents the longitudinal direction of the rod. Seeing this, the equations for calculating stress in COMSOL Multihphysics were modified in the x, y, z-directions by subtracting the component of magnetostriction from the x-component of strain in each stress equation. The modified stress equations are presented (Equations 5.1-5.3). The equations for x, y, and z stresses are only altered for the subdomains corresponding to the Galfenol components in the setup. However, the mechanical model in this setup consists only of a Galfenol rod, and thus the modified stress equations (Equations 5.1-5.3) can be used for the entire mechanical model.
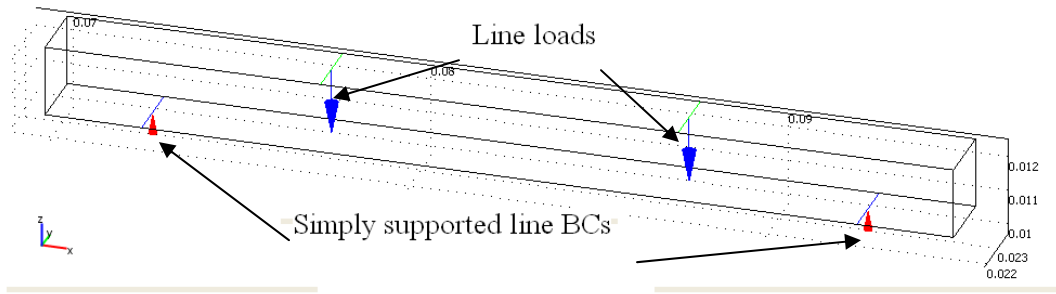
Figure 5.3. Mechanical model of Galfenol rod showing line loads (blue) and simply supported boundary conditions (red)

$$\sigma_x = E \frac{(1-\nu)(\varepsilon_x - \lambda) + \nu\varepsilon_y + \nu\varepsilon_z}{(1+\nu)(1-2\nu)} \quad (5.1)$$

$$\sigma_y = E \frac{\nu(\varepsilon_x - \lambda) + (1-\nu)\varepsilon_y + \nu\varepsilon_z}{(1+\nu)(1-2\nu)} \quad (5.2)$$

$$\sigma_z = E \frac{\nu(\varepsilon_x - \lambda) + \nu\varepsilon_y + (1-\nu)\varepsilon_z}{(1+\nu)(1-2\nu)} \quad (5.3)$$

5.2.2 – Magnetic model

The magnetic model consists of the Galfenol parallelepiped sample, an

electromagnet, and a coil.

The electromagnet is made up of steel and was assigned a relative

permeability of 2000. The solenoid was assigned a relative permeability of 1, and the

Galfenol rod was assigned a variable relative permeability via H(B,σ).

A current density was applied to the solenoid based on x, y, z components of

the magnitude of J_0 (Equations 5.4-5.6). In this particular model, the cross section of

the coil was in the y-z plane, leading to an x-component of current density equal to

zero.

99

$$J_x = 0 \qquad\qquad (5.4)$$

$$J_y = \frac{-J_0 z}{\sqrt{y^2 + z^2}} \qquad\qquad (5.5)$$

$$J_z = \frac{J_0 y}{\sqrt{y^2 + z^2}} \qquad\qquad (5.6)$$

The electromagnet core provides a flux path for the magnetic field to follow, and is aligned such that the magnetic field flows through the longitudinal direction of the rod. Figure 5.4 shows a typical flux return path in the magnetic model with the air domain suppressed. Suppression of the air domain was done in the postprocessing mode to show a more clear representation of the field lines within the electromagnet and Galfenol sample. It is important to note that the air domain was used to determine the magnetic field distribution shown in Figure 5.3, but was omitted in the figure for visualization purposes.
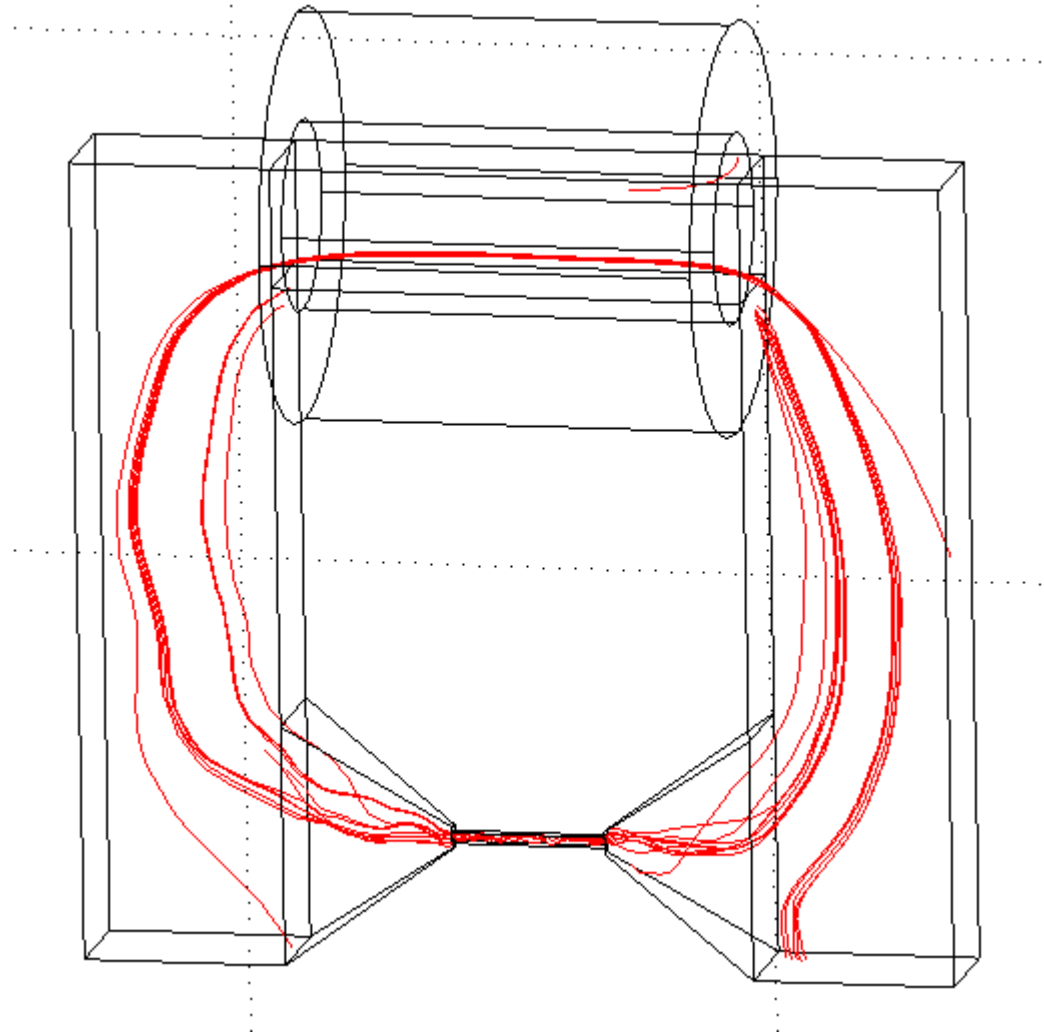
Figure 5.4. Typical flux path through electromagnet and into Galfenol sample (air domain suppressed here).

5.2.3 – BCMEM results

Experimental data was recorded for different magnetic inductions with varying bending moment. In order to model the specific zero bending moment magnetic inductions, a magnetic model was used to determine the relationship between the applied current density and corresponding magnetic induction (Figure 5.5). The J_0 versus B behavior was found to linear in nature. Using this plot, the

desired zero bending moment magnetic inductions can be used to back out the correct J_0's to use in the BCMEM.
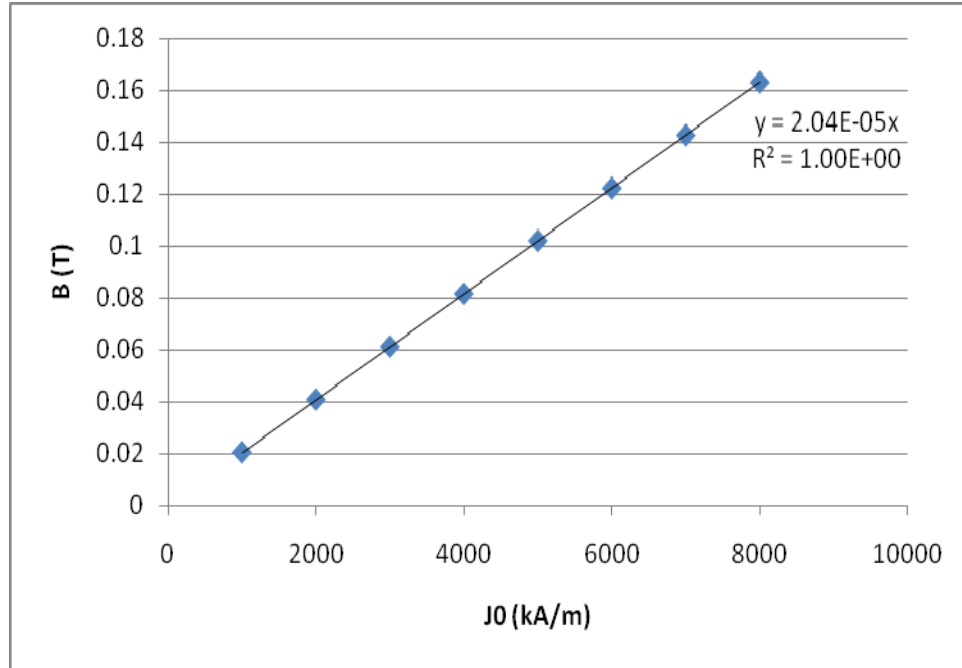
Figure 5.5. Magnetic induction versus applied current density for the no applied bending moment case.

The BCMEM results are shown in Figure 5.6. This figure shows that at low applied current densities, and thus, magnetic fields, there is a lower coupling between applied bending moment and corresponding change in magnetic induction. Coupling between applied bending moment and a change in magnetic induction is more evident at higher magnetic fields. At low magnetic fields, the magnetic moments of the sample are randomly oriented in nature. Thus, one would think that the effect of tension and compression would have the same effect, and thus one would expect to see little change in magnetic induction as is seen in Figure 5.6. However, at higher current densities (high magnetic fields), the moments are oriented in the direction that

would favor a tensile load. Therefore, tensile loads will not change the orientation of the magnetic moments, thus leading to no change in magnetic induction. However, if a compressive load is applied under the same magnetic field, there will be a much larger change in magnetic induction since the domains will want to rotate 90° to an orientation that is perpendicular to the applied magnetic field. This will lead to a large change in magnetic induction. From B-H characterization plots, it is known that a compressive stress will lower B for a given H. This is exactly what is observed in the experiment and predicted by the model as the induction drops as the stress increases. A visual representation of the above ideas is shown in Figure 5.7.

Datta et al. [41] coupled the Euler-Bernoulli Beam Model to the Armstrong Model to compare model and experimental results. However, Datta's model assumes that the field is constant within the sample. A benefit of BCMEM is its ability to calculate spatial variations of the magnetic field. However, both models are limited by the accuracy of the Armstrong model. Both models give results within 10% of experimental data.
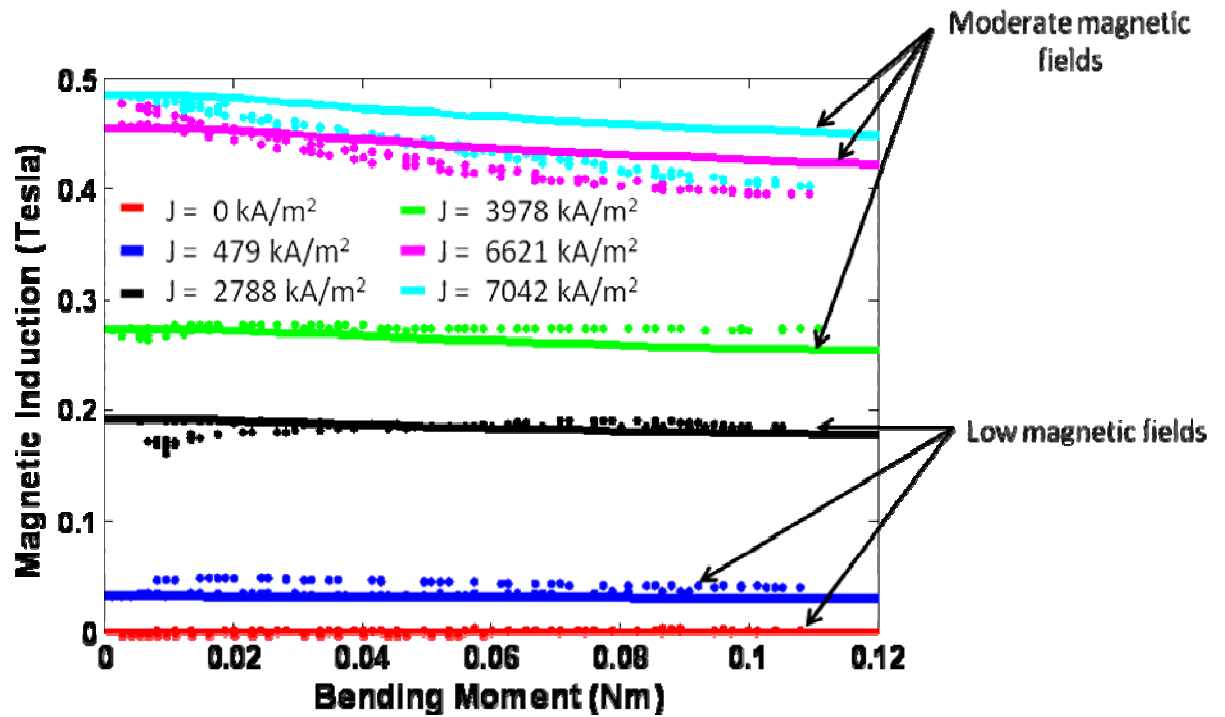
Figure 5.6. Magnetic induction changes with varying bending moment for different applied magnetic fields from experimental data [41] and BCMEM predictions.

Low fields: randomly oriented magnetic domains, compression and tension have similar effects on magnetic induction.

High fields: domains aligned in direction of applied field, tension negligibly changes magnetic induction, compression causes much larger change in magnetic induction.

Figure 5.7. Pictoral respresentation of affects of compression and tension on magnetic induction of sample with low (top) and high (bottom) applied magnetic fields.

Chapter 6: Conclusions

This thesis studied the bidirectional modeling of Galfenol using finite element software COMSOL Multiphysics 3.4 that was coupled to an energy-based model for prediction of nonlinear material behavior. This software was used in conjunction with COMSOL Script 1.2 to couple a magnetostatics (with currents) model to a static structural model to account for magnetoelastic coupling in Galfenol. Both the magnetic and mechanical models required the user to input B-H and λ-H data respectively. This data was initially determined experimentally and t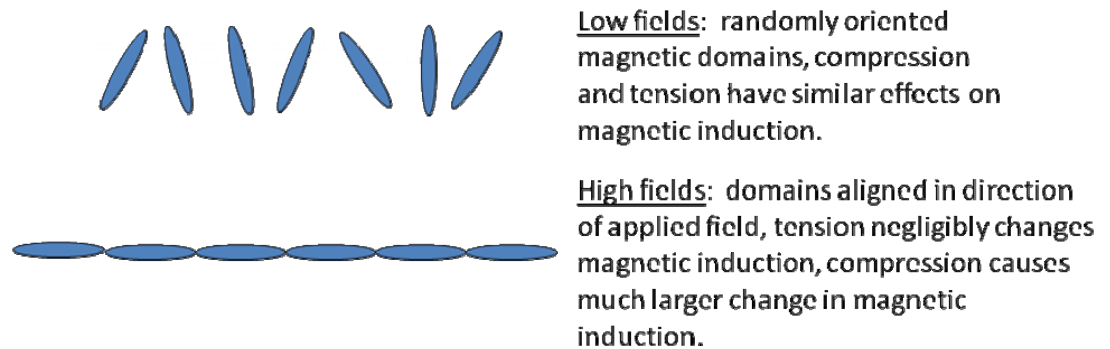hen expanded to a larger and more heavily discretized stress regime via the Armstrong model. The model predictions showed good correlation with experimental actuator load line results for a 16% at. Ga sample. The BCMEM actuator load lines also showed evidence of the delta-E effect. The model also compared well with experimental results for a four-point bending test, as the expected magnetic induction versus bending moment behaviors were accurately captured.

In future research, this model should be enhanced such that the key variables (λ and H) can be solved for as a function of B and σ in all directions (i.e., $\lambda(B_x, B_y, B_z, \sigma_x, \sigma_y, \sigma_z, \tau_{xy}, \tau_{zx}, \tau_{yz})$). This will help to give more accurate answers in problems where stresses and inductions are comparable in magnitude in different directions. For example, the torque sensor would require such a model. The Galfenol patch in this setup experiences compression along one direction and tension along the other. The BCMEM discussed in this work can analyze each variable independently: $H_x(B_x, \sigma_x)$ and $H_y(B_y, \sigma_y)$, but in reality, they affect each other: $H_x(B_x, B_y, \sigma_x, \sigma_y)$ and $H_y(B_x, B_y, \sigma_x, \sigma_y)$. Future research should be conducted to enhance the BCMEM to

account for this phenomenon. Further research can also be done to extend the

BCMEM so that it can handle dynamic cases. This will involve the use of a different

energy-based model than the Armstrong model which is only valid for quasi-static

cases. It would also be desirable to include models of coils that address number of

turns, gage of wire, resistance, inductance, etc. possibly with COMSOL script, for use

in optimization of the coil that produces the current density that is used as an input to

the BCMEM.

This thesis provides a foundation for the development of devices involving

current carrying applications, as proposed designs involving current carrying coils

can easily be analyzed using the BCMEM. The BCMEM can also be used optimizing

future experimental setups.

Appendix A: Experimental Characterization

This appendix outlines the procedure taken to experimentally characterize the magnetic and mechanical material properties of Galfenol. Properly modeling the key characteristics of any type of material is important to obtaining accurate performance predictions. The sample characterized in this discussion was not used in any of the BCMEM runs. This was due to the fact that it was desired to compare BCMEM results with experimental actuator load line and four point bending data, which had been previously gathered on a 16% and 18.4% at. Ga single crystal respectively. Instead, this appendix explores the characterization of an 18.4% at. Ga polycrystalline sample. However, the procedure for gathering λ-H and B-H data for single and polycrystalline Galfenol is the same.

In this characterization process, it was desired to characterize a 2-inch long, 0.25-inch diameter $Fe_{81.6}Ga_{18.4}$ polycrystalline sample. The ability to manufacture polycrystal samples at a much faster rate than single crystal samples will, more than likely, lead to the use of polycrystal samples in future applications and research. The experimental setup involved the use of a water cooled transducer designed by Kellogg [30]. The experimental characterization involved measurement of strain, magnetic induction, and magnetic field of the sample under quasi-static compressive stress from zero to 78 MPa and while the sample was subjected to different DC bias magnetic fields from 0 to 45 kA/m at a constant temperature 21 ± 1° C.

In a magnetostrictive material characterization, the λ-H and B-H plots provide valuable information regarding the materials performance. There are three key variables that are generally measured in a magnetostrictive material characterization: magnetostriction (λ), magnetic field (H), and magnetic induction (B). This section discusses how these three variables are measured on a cylindrical rod sample. All devices discussed in this section were wired to a data acquisition board. This board was connected to a computer which had Labview ©. Within the Labview program, key variables such as current, sample rate, amplifier gain, etc. are defined. Use of a Labview program is essential to calibrating, defining the experimental conditions, and recording data.

Strain was measured at the mid length of the rod. Two strain gages (CEA-06-250UN-350) were used on opposite sides at this location to ensure that bending effects are negated. They were connected in a quarter bridge configuration (700 ohms total due to 350 ohm contributions from each strain gage) to a Vishay 3800 strain indicator box.   In order to satisfy the quarter-bridge configuration, a 350 ohm resistor must also be attached to one of the connections on the strain indicator box. This makes a total of 700 ohms which is needed to balance the resistance of the strain gages. If one strain gage is used in an experimental test, and there is no need to use any additional resistors to balance the quarter-bridge formation since the connection on the Vishay box has a 350 ohm resistance. The gage factor of the strain gages was 2.105, and was used as an input into the strain indicator box. The gage factor helps to define the relationship between change in resistance and strain of the strain gauge.

For example, consider if a Galfenol rod strains 200 ppm. The corresponding change in resistance of the strain gage will be ($2.105*200*10^{-6} = 4.21*10^{-4} = 0.042\%$). The quarter bridge formation is very sensitive to small resistance changes and is capable of accurately predicting the strain resulting from such a small change in resistance. It is also important to tune the analog output of the strain indicator box to its strain sensitivity (2500 με/V). This value describes the strain change due to a voltage change.

A linear Hall Effect sensor (A1323EUA) was used to measure the magnetic field at the mid length of the rod. The Hall sensor was mounted perpendicular to the rod such that it measured magnetic field along the length of the sample. Section A.3 contains figures will give a pictorial representation of the sample preparation. It was mounted using silicon glue, which normally takes several days to dry. It is important to calibrate the Hall sensor before use. This can be done by measuring the Hall sensor response to different magnetic fields. A gauss meter along with the Hall sensor can be used to measure different magnetic fields resulting from different drive currents to a solenoid. A typical Hall sensor calibration plot is shown in Figure A.1. This particular Hall sensor has a sensitivity of 2.4962 mV/G.
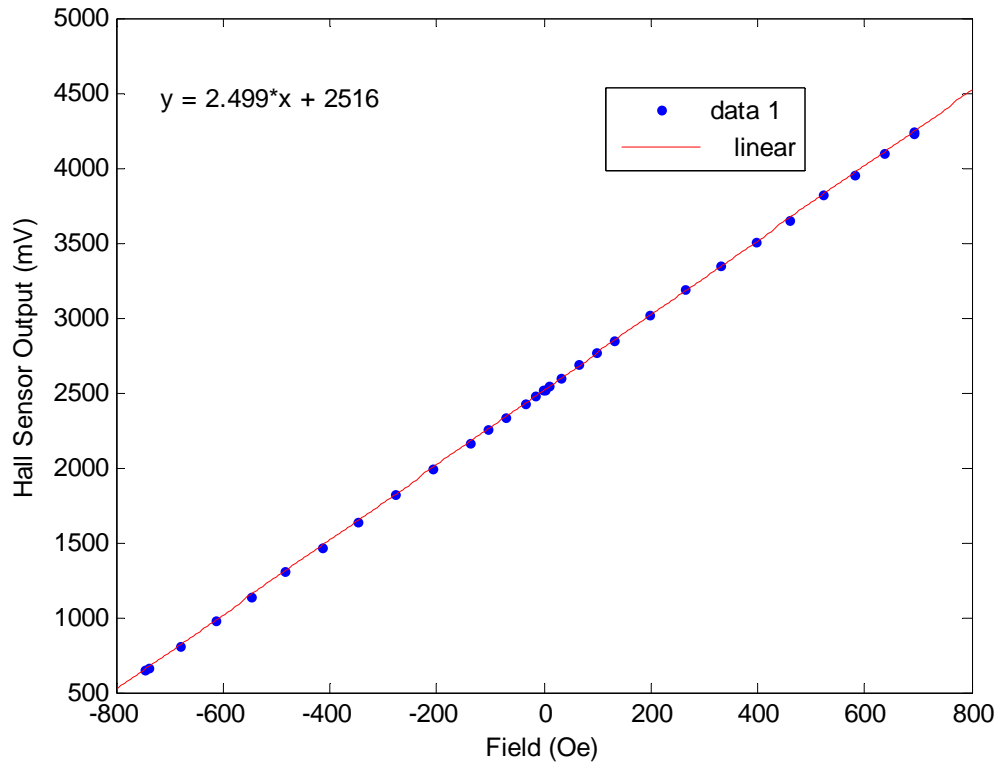
Figure A.1. Hall sensor calibration

Finally, the magnetic induction was measured using a sense coil, which was placed near the mid-height of the sample. The sense coil consisted of 100 turns and was monitored by a Walker Fluxmeter. The resistance of the coil and cm*turns are used as inputs to the fluxmeter.

A.2 – Transducer components

A cross sectional view of the transducer is shown in Figure A.2 and the full transducer setup is shown in Figure A.3. The different components in this figure will be discussed in this section.

The transducer includes two coils that current is passed through to provide a magnetic field to the sample. These coils are surrounded by water cooling tubes that ensure that the heating effects caused by the current passed through the coils have no thermal expansion effects on the strain read from the strain gage on the sample. The steel casing provides a well-defined flux return path due to its high permeability (μ_R = 2000). The loads were applied using a loading fixture that consisted of loads applied to a ball joint at the top of the steel casing. The ball joint ensures that loads are distributed to the sample in a strictly compressive manner. The sample is enclosed in a sample chamber of a length of ~2 inches. Since the sample used in this study was 2 inches, there was no gap between the sample and load applying fixture. However, many Galfenol samples that have been tested are less than 2-inches in length, and require steel end caps to ensure that the loading fixture is applying a load to the sample. It is important to use a magnetic material such as steel as the end cap material so that the magnetic circuit is not significantly altered. However, as described in Section 2.3.1, steel end caps will change the magnetic field distribution. As a result of using steel (μ_R = 2000) for shorter samples, the magnetic field will be higher longitudinally along the sample. This may cause the sample to saturate at a lower applied magnetic field.
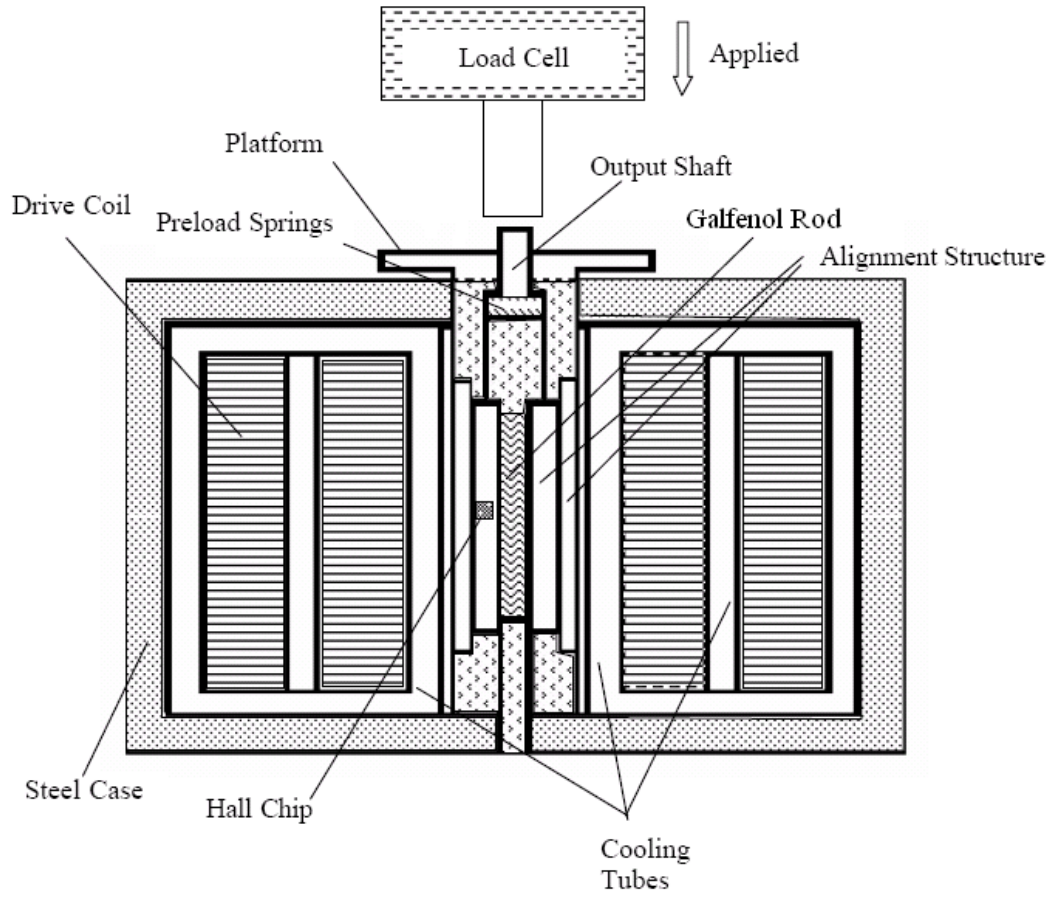
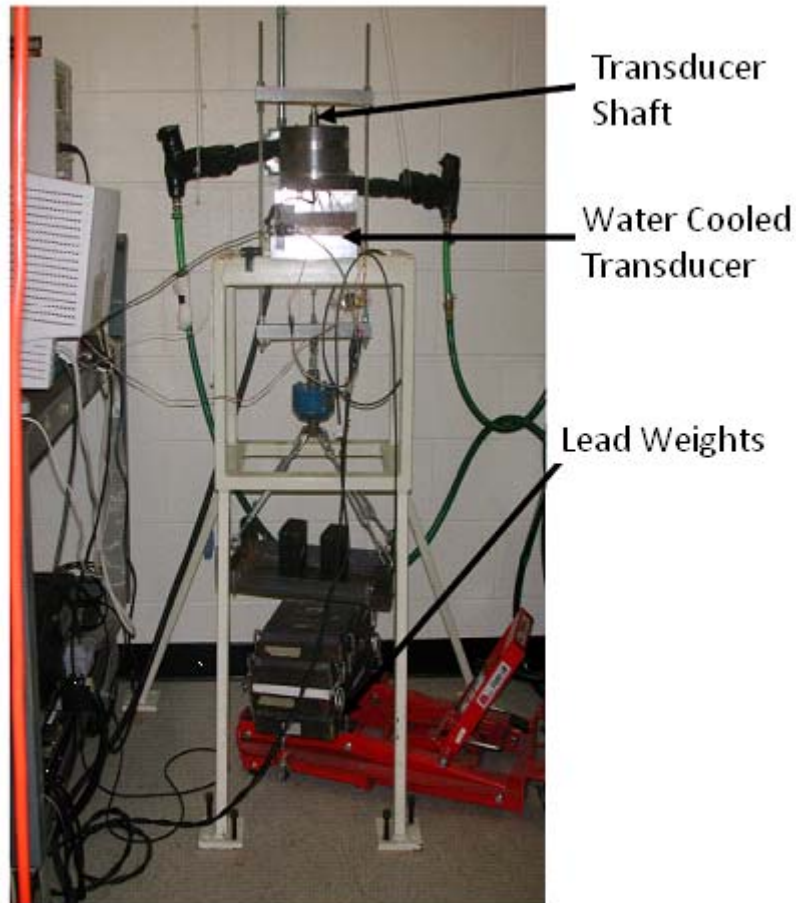**Figure A.2.** Cross-sectional view of water cooled transducer setup

Figure A.3. Transducer setup for quasi-static actuator (left) and sensor (right) characterization [14].

A.3 – Assembling the water cooled transducer

The first step in experimental characterization is to prepare the sample by mounting the strain gage, gluing the Hall sensor, and surrounding the rod with the sense coil. Figure A.4 shows a typical prepared sample. Strain gages were mounted at the mid-height of the rod on opposite sides to negate bending effects. From Figure A.4, it is clear that it would be more difficult to prepare smaller samples (i.e., 1 or 0.5-inch long samples).
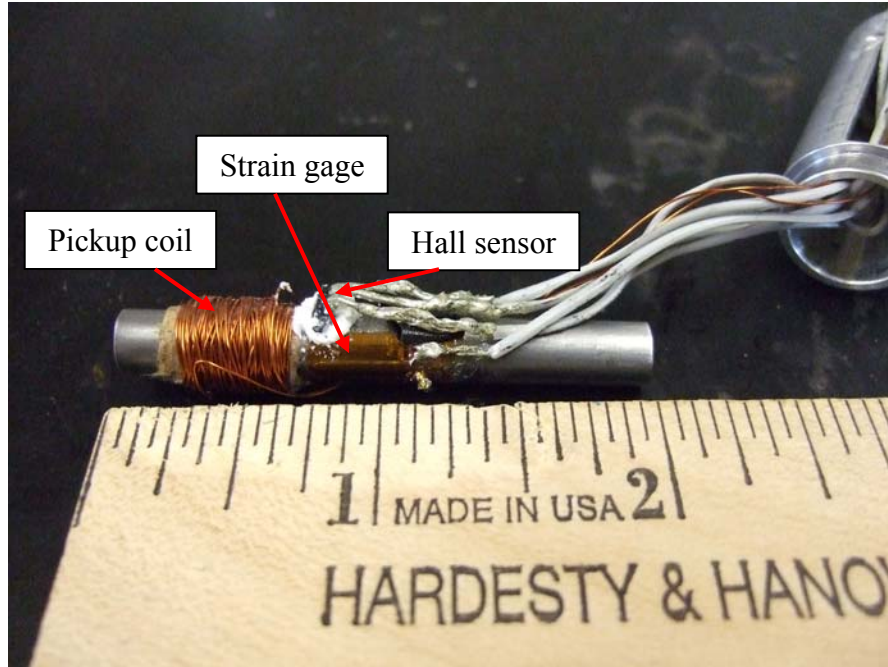
Figure A.4. 2-inch, 0.25-inch diameter 18.4 % at. Ga Polycrystal sample with strain gage, Hall sensor, and pickup coil.

The next step is to insert the prepared sample in the sample chamber. The sample chamber consists of two hollow cylindrical aluminum pieces which lock together when their respective grooves are lined up (Figure A.5.1-A.5.2). The wires should pass through the opening of the sample chamber (Figure A.5.3). It is important to use thin wire so that when the magnetostrictive rod is actuated, the wires do not rub up against the inner portion of the sample chamber. This rubbing can lead to inaccurate strain measurement results.
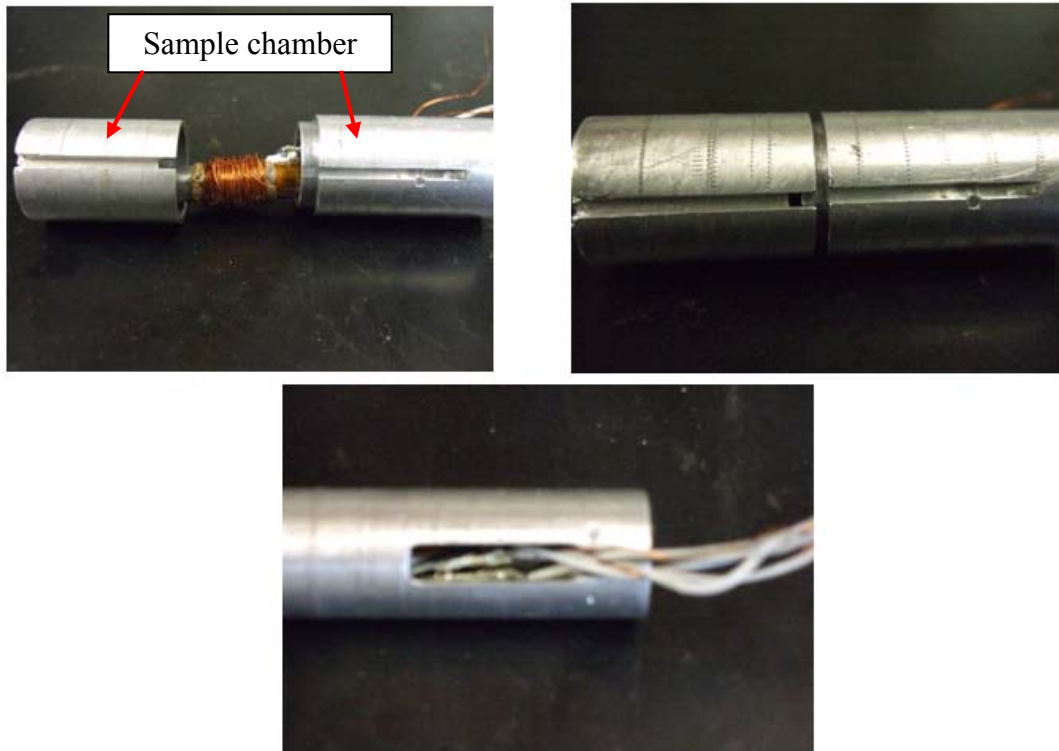
Figure A.5. **(1)** Upper-left – Placement of sample in sample chamber, **(2)** Upper-right – assembly of sample chamber, **(3)** Lower middle – placement of wires

The sample chamber is surrounded by the body (Figure A.6.1). Ensure that the notches on both the body and sample chamber are aligned. This will allow for a pathway for the wires. Next, screw the *base* onto the *body* (Figure A.6.2). If the *body* is screwed onto the *base*, then the wires connected to the body will rotate and become tangled. Next, ensure that the body and base are connected and properly aligned by using a small magnetic screw to secure the body to the base (Figure A.7.1). Finally, screw the base and body fixture into the text fixture (Figure A.7.2).
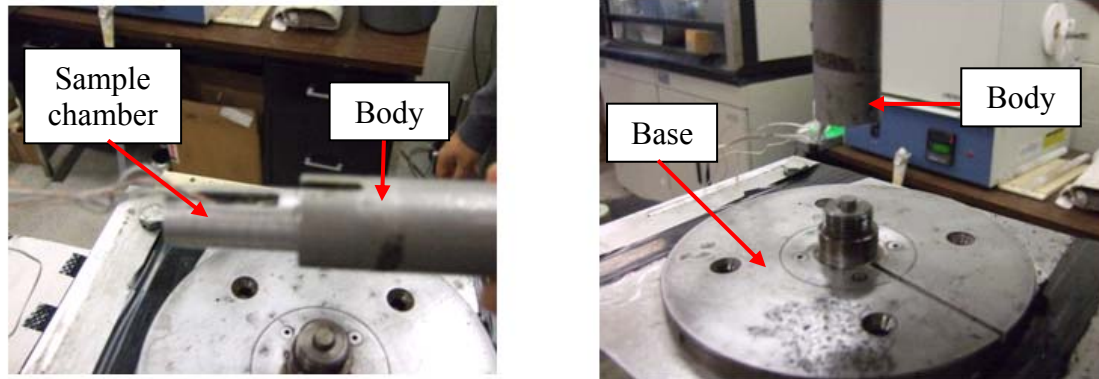
Figure A.6. (1) Left – sample chamber inserted into body. **(2)** Right – screw the body onto the base.
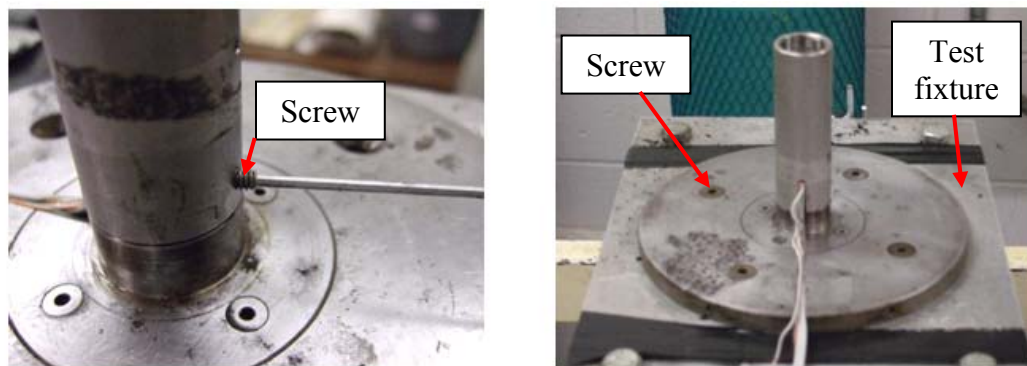
Figure A.7. (1) Left – body screwed to base. **(2)** Right – screw base to test fixture

To ensure that the wires do not come in contact with the coil, place tape around the body (Figure A.8.1). However, make sure that there is some slack between the wires and the sample. Otherwise, the wires will impede the magnetostriction of the sample. Place the pad over the base (Figure A.8.1). Next, surround the body with the coil, and surround the coil with the steel casing (Figure A.8.2).

Figure A.8. (1) Left – electrical tape around wires and flap on base. **(2)** Right – place coil around body, and steel casing around coil.
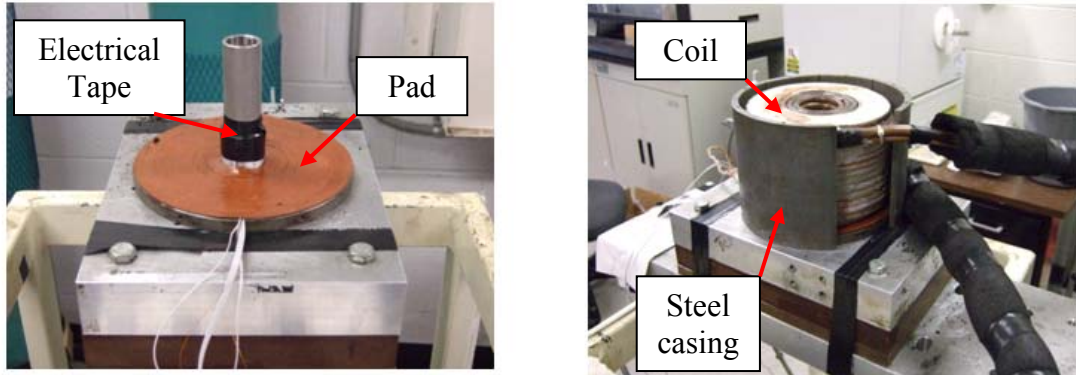
Refer to Figure A.9 for the final steps to the water cooled transducer assembly. First, screw the steel casing to the base. Next, place and screw the top steel casing to the main steel casing. Insert the plunger setup through the top steel casing. The plunger screws into the top of the base. Ensure that the plunger has a thin coating of magnetic grease (standard grease doped with fine iron particles) to negate any frictional effects. Place the loading fixture on the top of the plunger on the ball joint, which ensures that loading to the sample is strictly compressive. Finally attach hoses to each end of the transducer setup. One of the hoses gets plugged into a sink spout, and the other hose should drain into the sink.
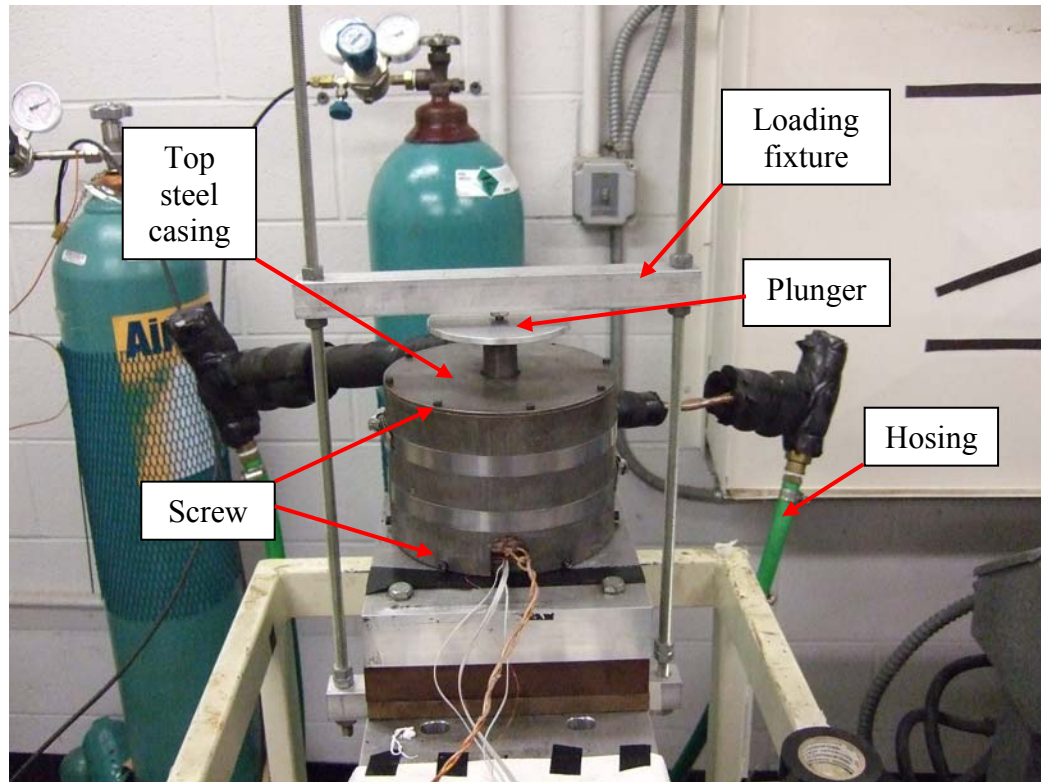
Figure A.9. Setup water cooled transducer

Now that the transducer is setup, it is time to attach the loading fixture to weights. Figure A.10 shows how a jack can be used to subject the loading fixture to different compressive weights. There are lead bricks within five different trays on the jack leading to a variety of different possible compressive prestress conditions. The water should be turned on prior to applying magnetic field to the sample.
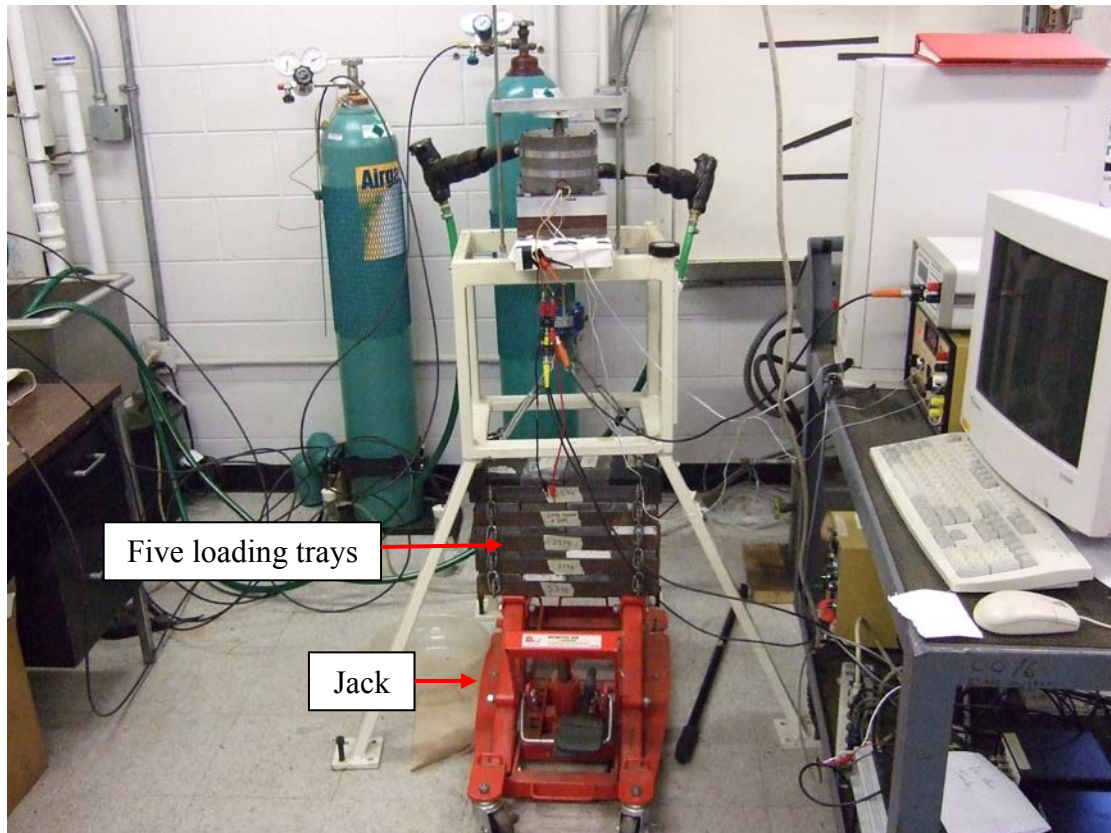
Figure A.10. Setup water cooled transducer with jack/weights.

A.4 – 18.4% at. Ga Polycrystal material characterization results

Before applying magnetic fields, it was desired to determining the Young's

Modulus of the polycrystal. The hard Young's Modulus of the material is used as an

input to the mechanical model in the BCMEM. Different compressive loads were

applied to the sample, and the corresponding strains were recorded at the zero field

condition. Figure A.11 below shows the stress-strain curve of the 18.4% Polycrystal

Galfenol sample for four different trials. It was determined that the average Young's

Modulus was 83.1 GPa. As previously stated, this particular sample was not modeled

with the BCMEM. However, this value of 83.1 GPa would be used in the mechanical

model as the hard Young's Modulus.
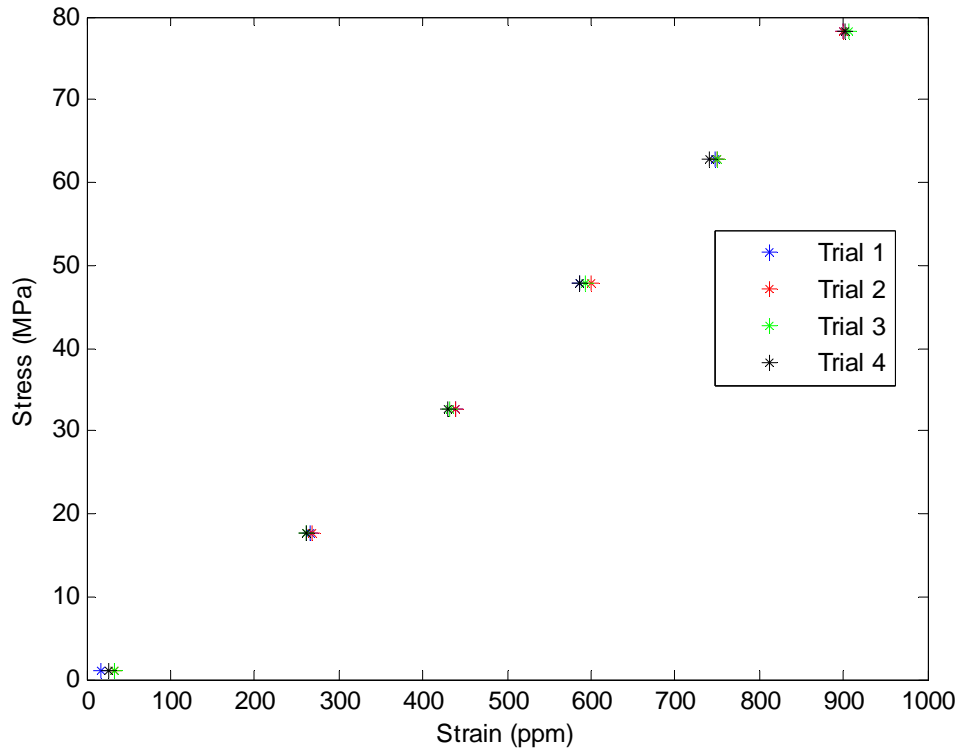
Figure A.11. Stress-strain curve for 18.4% polycrystalline Galfenol sample

The test procedure included first demagnetizing the sample, then applying

magnetic fields between 0 and 45 kA/m. This procedure was repeated for

compressive stresses of 17.61, 32.62, 47.78, 62.88, 78.26 MPa. As has been shown

previously, compressive stresses enhance the magnetostriction capabilities of the

material, as is evident upon investigation of Figure A.12. However, there is an

optimal stress that should be used which is reached rather quickly (17.61 MPa). At

this optimal compressive stress, the maximum magnetostrictive capabilities are

already reached and there is no need for additional compressive stresses. The addition of further compressive stress only will cause the need for more applied field to reach the same saturation magnetostriction. It was found that the zero stress magnetostriction (~120 ppm) was ~2/3 of the saturation magnetostriction (~200 ppm). The B-H curve also shows a stress dependency (Figure A.13). The application of compressive pre-stress changes the relative permeability of the sample.

As discussed in Section 3.5, the λ-H and B-H data for each stress is used as an input to the BCMEM. The Armstrong model is used to simulate the experimental data, and interpolate between stresses to develop λ-H and B-H data for a wide range of stresses, enhancing the accuracy of the model. For the magnetostatics (with currents) model, the $\lambda(H,\sigma)$ and $B(H,\sigma)$ determined experimentally must be converted to $\lambda(B,\sigma)$ and $H(B,\sigma)$. This data is then saved to a text file, where the model determines the dependent variables B and σ, and uses the text file to solve for λ and H.

This appendix serves as an introduction to the techniques used to experimentally characterize a magnetostrictive sample. See [30] for a more thorough description of the water cooled transducer experimental characterization.
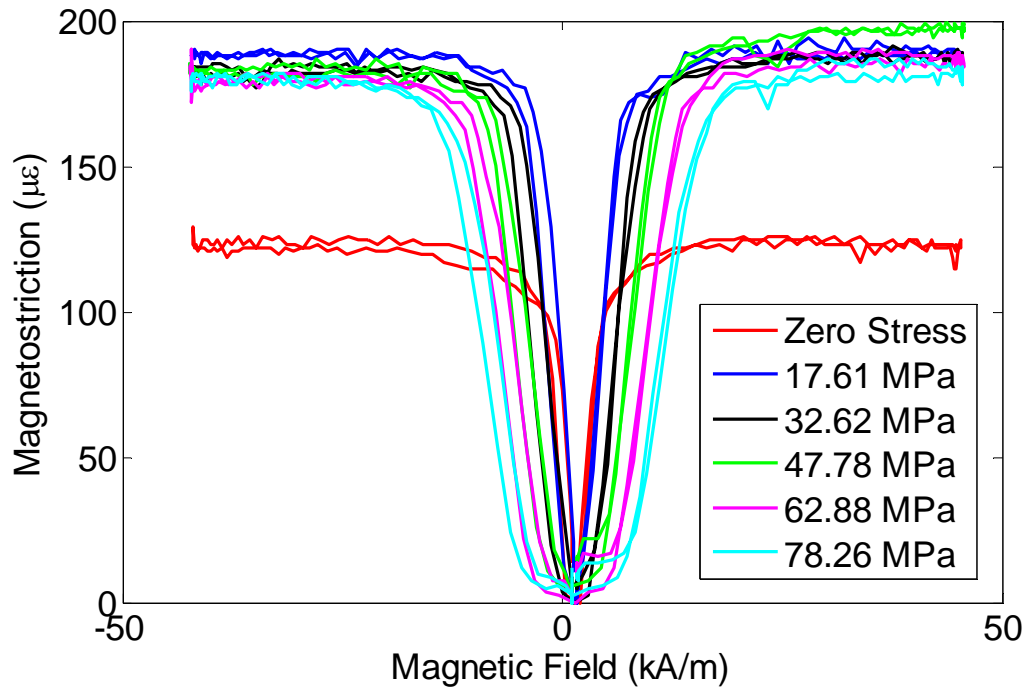
Figure A.12. λ-H plot for 18.4% at. Ga, polycrystal, production grade (Etrema Products, Inc.)
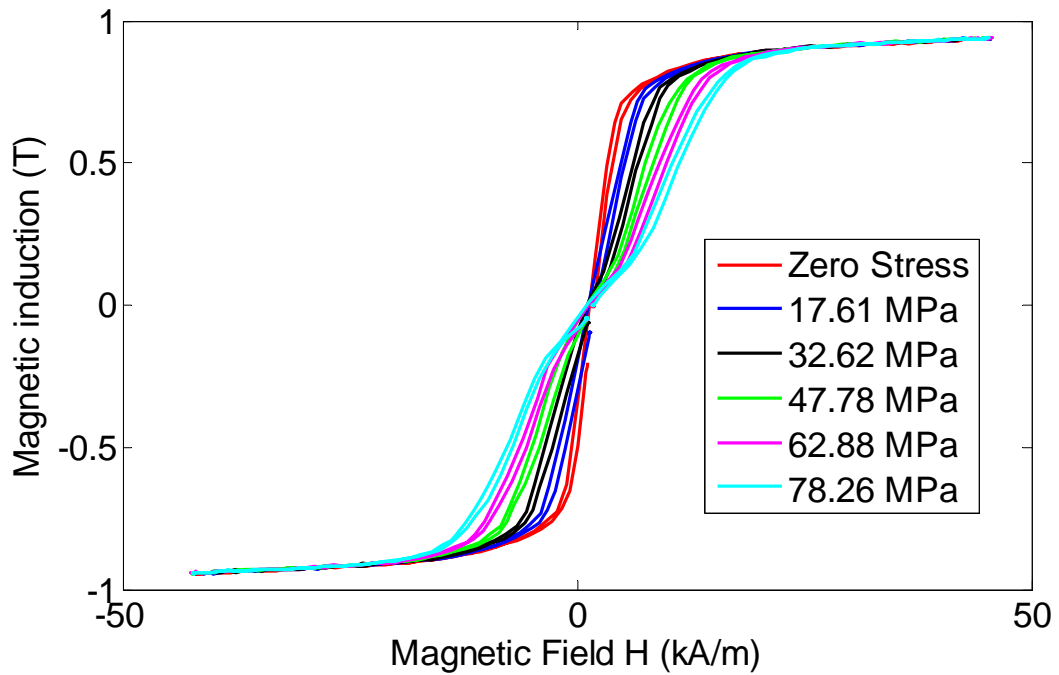

Figure A.13. B-H plot for 18.4% at. Ga polycrystal, production grade (Etrema Products Inc.)

Bibliography

[1]   F. T. Calkins, A. B. Flatau, and M. J. Dapino, "Overview of magnetostrictive sensor technology," *Journal of Intelligent Material Systems and Structures,* vol. 18, no. 10, pp. 1057-1066, Oct 2007.

[2]   C. Mudivarthi, S. Datta, J. Atulasimha, and A. Flatau, "A bidirectionally coupled magnetoelastic model and its validation using a Galfenol unimorph sensor," *Smart Materials and Structures,* vol. 17, no. 3, 2008.

[3]   I. Chopra, "Review of state of art of smart structures and integrated systems," *Aiaa Journal,* vol. 40, no. 11, pp. 2145-2187, Nov 2002.

[4]   J. McCormick, R. DesRoches, D. Fugazza, and F. Auricchio, "Seismic vibration control using superelastic shape memory alloys," Asme-Amer Soc Mechanical Eng, 2006, pp. 294-301.

[5]   J. P. Joule, "On a new class of magnetic forces," *Am. Electr. Magn. Chem,* vol. 8, no. p. 219, 1842.

[6]   E. Villari, "Change in magnetization by tension and by electric current," *Ann. Phys. Chem,* vol. 126, no. pp. 87-122, 1865.

[7]   E. W. Lee, "Magnetostriction and Magnetomechanical Effects," *Reports on Progress in Physics,* vol. 18, no. pp. 184-229, 1955.

[8]   J. B. Restorff, "Magnetostrictive Materials and Devices," *Encyclopedia of Applied Physics 9,* no. pp. 603-616, 1994.

[9]   A. E. Clark, M. Wun-Fogle, J. B. Restorff, and T. A. Lagrasso, "Magnetic and Magnetostrictive Properties of Galfenol Alloys Under Large Compressive Stresses," in *International Symposium on Smart Materials-Fundamentals and*

System Applications, Pacific Rim Conference on Advanced Materials and Processing (PRICM-4), Honolulu, Hawaii, 2001.

[10]   A. Clark and D. Crowder, "High temperature magnetostriction of TbFe$_2$ Tb$_{.27}$Dy$_{.73}$Fe$_2$," *Magnetics, IEEE Transactions on,* vol. 21, no. 5, pp. 1945-1947, 1985.

[11]   R. A. Kellogg, A. M. Russell, T. A. Lograsso, A. B. Flatau, A. E. Clark, and M. Wun-Fogle, "Tensile properties of magnetostrictive iron-gallium alloys," *Acta Materialia,* vol. 52, no. 17, pp. 5043-5050, 2004.

[12]   P. R. Downey and A. B. Flatau, "Magnetoelastic bending of Galfenol for sensor applications," *Journal of Applied Physics,* vol. 97, no. 10, p. 10R505, 2005.

[13]   M. J. Parsons, S. Datta, C. Mudivarthi, S. M. Na, and A. Flatau, "Torque sensing using rolled galfenol patches " in *Proceedings of SPIE*, San Diego, CA, 2008.

[14]   J. Atulasimha, "Characterization and Modeling of the Magnetomechanical Behavior of Iron-Gallium Alloys," Phd Dissertation in *Department of Aerospace Engineering*, University of Maryland, College Park, MD, 2006.

[15]   R. A. Kellogg, "Development and Modeling of Iron-Gallium alloys," Phd Dissertation in *Engineering Mechanics*, Iowa State University, Ames, IA, 2003.

[16]   E. M. Summers, T. A. Lograsso, J. D. Snodgrass, and J. C. Slaughter, "Magnetic and mechanical properties of polycrystalline Galfenol," in *Smart*

Structures and Materials 2004: Active Materials: Behavior and Mechanics, San Diego, CA, 2004, pp. 448-459.

[17] A. E. Clark, "Magnetostrictive rare earth-Fe_2 compounds," *Ferromagnetic Materials,* vol. 1, no. pp. 531-589, 1980.

[18] J. R. Cullen, A. E. Clark, M. Wun-Fogle, J. B. Restorff, and T. A. Lograsso, "Magnetoelasticity of Fe-Ga and Fe-Al alloys," *Journal of Magnetism and Magnetic Materials,* no. pp. 948-949, 2001.

[19] A. E. Clark, K. B. Hathaway, M. Wun-Fogle, J. B. Restorff, T. A. Lograsso, V. M. Keppens, G. Petculescu, and R. A. Taylor, "Extraordinary magnetoelasticity and lattice softening in bcc Fe-Ga alloys," *Journal of Applied Physics,* vol. 93, no. 10, pp. 8621-8623, 2003.

[20] A. E. Clark, J. B. Restorff, M. Wun-Fogle, T. A. Lograsso, and D. L. Schlagel, "Magnetostrictive properties of body-centered cubic Fe-Ga and Fe-Ga-Al alloys," in *IEEE Transactions on Magnetics*, 2000, pp. 3238-3240.

[21] A. E. Clark, M. Wun-Fogle, J. B. Restorff, T. A. Lograsso, and J. R. Cullen, "Effect of quenching on the magnetostriction of $Fe_{1-x}Ga_x$ (0.13 < x < 0.21)," in *8th Joint MMM-Intermag Conference*, 2001, pp. 2678-2680.

[22] D. P. Ghosh and S. Gopalakrishnan, "Coupled analysis of composite laminate with embedded magnetostrictive patches," *Smart Materials and Structures,* vol. 14, no. 6, pp. 1462-73, 2005.

[23] J. L. Pérez-Aparicio and H. Sosa, "A continuum three-dimensional, fully coupled, dynamic, non-linear finite element formulation for magnetostrictive materials," *Smart Materials and Structures,* vol. 13, no. 3, p. 493, 2004.

[24] F. T. Calkins, "Design, Analysis, and Modeling of Giant Magnetostrictive Transducers," Ames, Iowa: Iowa State University, 1997.

[25] T. Suzuki and E. Matsumoto, "Magnetoelastic behavior of ferromagnetic materials using stress dependent Preisach model based on continuum theory," *International Journal of Applied Electromagnetics and Mechanics,* vol. 19, no. 14, pp. 485-489, 2004.

[26] P. G. Evans, M. J. Dapino, and J. B. Restorff, "Bill Armstrong memorial symposium: free energy model for magnetization and magnetostriction in stressed Galfenol alloys," in *Proceedings of SPIE, Behavior and Mechanics of Multifunctional and Composite Materials*, San Diego, CA, 2007, p. p. 652619.

[27] M. J. Sablik and D. C. Jiles, "Coupled Magnetoelastic Theory of Magnetic and Magnetostrictive Hysteresis," *Ieee Transactions on Magnetics,* vol. 29, no. 4, pp. 2113-2123, Jul 1993.

[28] W. D. Armstrong, "Magnetization and magnetostriction processes in $Tb_{(0.27 - 0.30)}Dy_{(0.73 - 0.70)}Fe_{(1.9 - 2.0)}$," *Journal of Applied Physics,* vol. 81, no. 5, pp. 2321-2326, 1997.

[29] S. Datta, J. Atulasimha, C. Mudivarthi, and A. B. Flatau, "The modeling of magnetomechanical sensors in laminated structures," *Smart Materials & Structures,* vol. 17, no. 2, p. 9, Apr 2008.

[30] R. Kellogg, "The Delta-E effect in Terfenol-D and its application in a tunable mechical resonator," M.S. Thesis in *Engineering Mechanics*, Iowa State University, Ames, IA, 2000.

[31] J. Atulasimha, A. B. Flatau, and E. Summers, "Characterization and energy-based model of the magnetomechanical behavior of polycrystalline iron-gallium alloys," *Smart Materials & Structures,* vol. 16, no. 4, pp. 1265-1276, Aug 2007.

[32] S. Datta and A. Flatau, "Magnetomechanical coupling factor and energy density of single crystal iron-gallium alloys," in *Behavior and Mechanics of Multifunctional and Composite Materials*, San Diego, CA, 2008, p. 69291Z.

[33] S. Chikazumi, *Physics of Magnetism*: John Wiley and Sons, Inc., 1964.

[34] R. I. Joseph and Schloman.E, "Demagnetizing Field in Nonellipsoidal Bodies," *Journal of Applied Physics,* vol. 36, no. 5, pp. 1579-&, 1965.

[35] W. B. Brown, *Magnetostatic Principles in Ferromagnetism* vol. 1. New York: North-Holland, 1962.

[36] J. Atulasimha, A. B. Flatau, and R. A. Kellogg, "Sensing Behavior of Varied Stoichiometry Single Crystal Fe-Ga," *Journal of Intelligent Material Systems and Structures,* vol. 17, no. 2, pp. 97-105, 2006.

[37] T. H. H. Pian and S. W. Lee, "Finite-Elements for Nearly Incompressible Materials," *Aiaa Journal,* vol. 14, no. 6, pp. 824-826, 1976.

[38] R. Kellogg and A. Flatau, "Blocked-Force Characteristics of Terfenol-D Transducers," *Journal of Intelligent Material Systems and Structures,* vol. 15, no. 2, pp. 117-128, February 1, 2004 2004.

[39] M. J. Dapino, "Nonlinear and hysteretic magnetomechanical model for magnetostrictive transducers," Phd Dissertation in *Engineering Mechanics*. Iowa State University, Ames, IA, 1999.

[40]   S. Datta, J. Atulasimha, C. Mudivarthi, and A. Flatau, "Stress and magnetic field dependent Young's modulus in single crystal iron-gallium alloys," in *19th International Conference on Adaptive Structures and Technologies*, Ascona, Switzerland, 2008.

[41]   S. Datta, J. Atulasimha, and A. Flatau, "Modeling of magnetostrictive Galfenol sensor and validation using four point bending test," *Journal of Applied Physics,* vol. 101, no. 9, pp. 09C521-09C521-3, 05/2007 2007.